THE UNIVERSITY *of* EDINBURGH

Neutron Skin Measurement of Tin Isotopes

Dominika A. Glowa

School of Physics and Astronomy
University of Edinburgh

A thesis submitted for the degree of
Doctor of Philosophy
The University of Edinburgh
November 2015

Acknowledgements

I would like to thank my supervisor, Dan Watts for his trust and all the help and guidance over the past few years. Thank you for helping me prepare for the thesis defence and for believing I would pass even when I have doubted it. It has been an honour working with you.

Vorrei anche ringraziare il mio secondo supervisore, Lorenzo Zana. Grazie per il tuo aiuto, per i tuoi consigli e per il sostegno che mi hai dato durante il mio dottorato di ricerca, per avermi pazientemente insegnato a navigare i meandri di programmazione e delle simulazioni G4, e per il tuo prezioso aiuto nel leggere e correggere la stesura iniziale della mia tesi di laurea. Grazie di tutto. Non ce l'avrei mai fatta senza di te.

I would like to thank my fellow PhD student, Jamie Fleming for always keeping me company for tea and watching news and politics breaks, for putting up with my rants when my analysis code was crashing and for always offering a helping hand with my work.

Finally, I would like to thank my family for their support and encouragement during my doctorate, I dedicate this thesis to you.

Thank you guys, this would not have been possible without you!

Abstract

Heavy atomic nuclei are thought to have proton and neutron radial distributions which have different extents. This difference is usually quantified in terms of a neutron skin (r_{np}), defined as the difference between the root mean square radii of the neutron and proton radial distributions ($r_{np} = r_n - r_p$). The nature, or even existence, of the neutron skin is currently not well established for many nuclei. Different nuclear theories give different predictions for the neutron skin thickness ranging for a typical heavy nucleus from 0.05 to 0.35 fm. Accurate measurement of the properties of the neutron skin would be a powerful constraint to differentiate between models of nuclear structure, improving our knowledge of the basic Equation Of State (EOS) for neutron rich matter. Particularly, the rate at which the neutron skin thickness changes across an isotopic chain of nuclei gives a tight constraint on the EOS and is also amenable to experimental determination with small systematic error. Improving our knowledge of the EOS for neutron rich matter is a crucial step towards gaining a deeper understanding of nuclear structure and nuclear matter in general. These results will also impact our knowledge of compact astrophysical objects such as neutron stars. This thesis describes the first measurement of neutron skin thicknesses along an isotopic chain using an electromagnetic probe. The neutron skin is measured through the study of the coherent photoproduction of neutral π mesons emitted from nuclei.

This experiment was carried out in the A2 hall of the MAMI facility in Mainz, Germany in October 2012. The incident photon beam comprised of energy tagged photons in the range of E_γ=150-800 MeV with an intensity of 10^8 photons per second. Experimental data was obtained for three different tin targets, ^{116}Sn, ^{120}Sn and ^{124}Sn. The products from the resulting photoreactions were measured in the Crystal Ball detector and in the TAPS calorimeter systems, with track and particle identification information for charged particles provided by a multi wire

proportional chamber (MWPC) and a particle identification detector (PID).

The experiment provides the first information on the evolution of the neutron skin thickness along an isotopic chain using an electromagnetic probe. The results are compared with a range of theoretical models and previous data from strongly interacting probes. The new data will provide an important new experimental constraint on the basic properties of the EOS in atomic nuclei.

Lay Summary

For centuries, scientists have employed various experimental techniques to explore the composition of the universe. Ever since it has been discovered that ordinary matter is built from small constituent units called atoms, much research has been devoted to study their size, shape and internal structure. The atom consists of a dense positively charged atomic nucleus surrounded by a cloud of negatively charged electrons. The nucleus is made up of protons (positively charged particles) and neutrons (uncharged particles). The characteristic that defines an element and differentiate atoms from one another is their proton number. However, even if elements have the same number of protons they may still have different number of neutrons. Such variants of an element are called isotopes. Isotopes can be stable (those whose proton and neutron numbers do not change over time) or unstable, which attain more stable configurations via radioactive decays.

Heavy atomic nuclei require higher number of neutrons than protons to be stable. Those *neutron rich* nuclei have been shown to have different proton radius, r_p, and neutron radius, r_n, this difference is usually described in terms of a neutron skin ($r_{np} = r_n - r_p$). Currently, the nature and size of the neutron skin for many nuclei is not very well established and various nuclear theories predict vastly different sizes of the neutron skin. Accurate measurement of the neutron skin would provide information about internal structure of atoms and also greatly improve our knowledge of *neutron rich* matter that builds neutron stars.

This thesis presents the first information on the evolution of the neutron skin thickness along an isotopic chain of tin using a photon probe. Tin has been chosen for this experiment because of its wide range of stable isotopes; three different isotopes have been used, ^{116}Sn, ^{120}Sn and ^{124}Sn with 116, 120 and 124 representing mass number (combined number of protons and neutrons).

Studying the evolution of the neutron skin along the isotopic chain (elements differing only by the number of neutrons) allows some cancellation of systematic effects as the experimental measurements are all made with the same apparatus and the predicted change in the skin may be less sensitive to inaccuracies in the theoretical modelling of the reaction process. The results are compared with a range of theoretical models and previous data from other experiments. The experiment described in this thesis was carried out in the A2 hall of the MAMI facility in Mainz, Germany. This facility provides an intense photon beam which was impinged on various nuclear targets. Information on the neutron skin was extracted through a measuerement of coherent π^0 photoproduction. In this process an incident photon creates a π^0 meson particle from one of the nucleons inside the atomic nucleus; and the nucleus remains in its initial state after this process (i.e. it is not excited). The new data provides an important new experimental constraint on the size of the neutron skin and the basic properties of nuclear matter.

Declaration

The data presented in this thesis was obtained in experiments carried out by the CB@MAMI collaboration in the A2 hall of the Institut fur Kernphysik at the University of Mainz, Germany. I played a major role in the preparation and execution of the experiment, the data analysis and interpretation is entirely my own work. Any contributions from colleagues in the CB@MAMI collaboration such as diagrams or calibrations are explicitly referenced in the text. This thesis was written by myself and the work presented in it has not been submitted in support of another degree or qualification from this or any other university or institute of learning.

D. A. Glowa
November 2015

Contents

Chapter 1

Prologue

The composition of the world around us has been of profound interest to humanity throughout recorded history; the earliest known records attempting to explain the composition of matter date back to antiquity. Since 1911, when Rutherford elucidated the structure of the atom as being composed of a compact dense nucleus surrounded by a more diffuse electron cloud, obtaining a better understanding of the nucleus has been a major endeavour of physics. Various experimental techniques have been developed to determine the size, shape and momentum distributions of atomic nuclei, providing a wealth of data from across the nuclear chart. As a result of precise experimental methods such as electron scattering and muonic atoms x-ray spectroscopy the charge distribution in nuclei has been estimated with high accuracy, for example the root mean square charge (r.m.s.) radius of ^{208}Pb is known to a $\sim$ 0.01% accuracy [1]. Despite the huge success of these experimental methods in determining the distribution of protons within a nucleus, the probes employed have been largely insensitive to the neutron distribution in the nucleus. This is because the electrons dominantly interact with the charged components in the nucleus and are only senstive to the uncharged components through the much weaker magnetic interaction. Strongly interacting probes such as protons, antiprotons and alpha particles do interact with neutrons, but their strong interactions and the resulting short mean free path of the probe in the nucleus have resulted in inconsistent determinations of the nature of the neutron distribution. The theoretical models describing these processes are subject to large model uncertainties due to uncertainties in the description of the strong interaction in the nuclear medium [2]. Currently it is

not well established how the distributions of neutrons differ from those of protons in the nucleus. Recent work using an electromagnetic probe and the method of coherent photoproduction of a neutral π meson has provided new constraints for ^{208}Pb [3] with different systematics to previous measurements. This work will use the same technique as the one employed in the case of ^{208}Pb to obtain the first assesment of how a neutron skin evolves across an isotopic chain of tin.

According to theoretical predictions of the nuclear structure, nuclei with similar numbers of protons and neutrons have almost no difference in their r.m.s. radii of charge and matter distributions. However, this is predicted to change with increasing mass number. For isotopes with greater numbers of neutrons than protons, it is predicted that the excess neutrons form a small skin around the nucleus. The size of this neutron skin is usually defined as:

$$\Delta R = r_n - r_p \tag{1.1}$$

where r_n and r_p are the r.m.s. radii of neutrons and protons respectively [4]. Having ΔR determined accurately by experiment for a range of nuclei will provide a stringent constraint on the current nuclear structure theories. There are many different theoretical models in common use, which predict very different values for the neutron skin despite giving good descriptions of a wealth of nuclear properties already determined. New experimental measurements, providing accurate determination of the size and shape of the neutron skin, would provide a means of verifying the validity of these models. Furthermore, an accurate measurement of the neutron skin will have more far reaching implications. Currently, poorly established parameters in the equation of state for neutron rich matter show a linear dependence with the size of the neutron skin, irrespectively of the model employed in the analysis. Precise measurement of the neutron skin will also place much needed constraints on these parameters. This in turn has the potential to improve our understanding of the physics of neutron stars, which have a common dependence on the equation of state. Accurate neutron skin measurements have been proposed as a way of obtaining a better constraint on the mass-radius relationship of low mass neutron stars and also establish the feasibility of proposed cooling mechanisms such as the modified URCA cooling, which is a rapid neutrino cooling of neutron stars [5].

Neutron skin measurements have been performed with strongly interacting

probes before [6, 7]. The data obtained were strongly affected by many-body strong interaction effects that made the analysis and interpretation of results ambiguous, which made it difficult to draw a solid conclusion on the size of the skin. Measurements of global nuclear properties, such as the dipole or pygmy resononaces provide valuable information but the model dependence of the extraction method is still debated.

The use of photons to study the neutron skin, potentially allows for much more accurate measurements than strongly interacting probes. The strength of the photon's electromagnetic interaction is weak when compared to the strong force. Thus, the reaction is not affected as much by the initial state interactions (ISI). Also, the many-body interaction effects, arising from multiple scatters of the incoming probe in the nucleus, do not complicate the interpretation of the obtained data. Furthermore, because the electromagnetic interaction is better understood than the strong interactions, the results obtained with the use of electromagnetic probes may be less sensitive to systematic effects in their theoretical interpretation [2].

The main objective of the experiment presented in this thesis is to exploit coherent π^0 photoproduction as a mean of studying the nuclear matter distribution of three stable tin isotopes.

Pion photoproduction takes place when a high energy photon interacts with a nucleon what results in an emission of pions. Coherent nuclear π^0 photoproduction takes place when a photon interacts with a nucleon within an atomic nucleus and as a result a π^0 meson is emitted. In the region where the mechanism for this process is dominated by the Δ resonance, the photoproduction takes place with close to equal probablity on protons and neutrons. For the coherent process, where the target nucleus remains in its ground state, $A(\gamma, \pi^0)A$, the interefrence of the production amplitudes from all the nucleons contains information about the matter distribution of the target nucleus. Therefore, by increasing only the number of neutrons we are able to determine how the neutron skin thickness evolves increasing only the number of neutrons.

The theoretical background to the experiment and methodology are presented in the next chapter. The experimental details are presented in the subsequent chapter. This is followed by a summary of the current state of knowledge and a description of the implications of the results presented in this thesis for the future

research. The following chapters present the analysis and experimental details while the results and conclusions are discussed in the final chapters.

Chapter 2

Neutron Skins: Theoretical Background and Previous Experimental Measurements

This chapter introduces the theoretical background representing our current understanding of the processes for pion photoproduction and presents the theoretical model used in interpreting the current data. Following this the state-of-the-art nuclear theories are outlined as well as the link between nuclear properties and the nuclear equation of state.

2.1 Background

In 1932, Heisenberg formulated an idea that protons and neutrons are in fact two states of the same particle, the nucleon [8]. He proposed a new quantum number to label these states and called it isospin (I), which in case of a nucleon carries a value of $\frac{1}{2}$. The Z components of the isospins, labelled as I_3, are therefore $I_3 = \frac{1}{2}$ for proton and $I_3 = -\frac{1}{2}$ for neutron. Hence, the charge Q of the the nucleon can be written as:

$$\frac{Q}{e} = \frac{1}{2} + I_3 \tag{2.1}$$

where e is the charge of an electron.

In 1935, Yukawa proposed that, in order for the nucleons to be held together in

a nucleus, some kind of "strong" force must exist and that the mediator particle for this force should be a spin-0 meson with a mass of $\sim$ 150 MeV [9]. The existence of such particle was proven 12 years later, in 1947, when charged pions were discovered by the collaboration of C. Powell, C. Lattes and G. Occhialini [10].

Pions are the lightest mesons with mass of $\sim$ 135 MeV and they act as mediators of the long-range part of the strong nuclear force. They are zero spin particles composed of two valence quarks and they can be found in three states; neutral, (π^0), and charged, (π^+ and π^-).

Charged pions decay via weak interactions into a muon and a neutrino (equations 2.2 and 2.3). The branching ratio of this decay mode is $\sim$ 99.988% with a mean lifetime of 2.6×10^{-8} s.

$$\pi^+ \rightarrow \mu^+ + \nu_\mu \tag{2.2}$$

$$\pi^- \rightarrow \mu^- + \bar{\nu_\mu} \tag{2.3}$$

Other possible decay modes create an electron and anti-neutrino (π^-), or a positron and neutrino (π^+). However, the probability of these decay channels is very low $\sim$ 0.001%.

Neutral pions decay via electromagnetic interactions with a mean lifetime of 8.4×10^{-17} s. The dominant decay mode (with a branching ratio of $\sim$ 99%) is into two photons:

$$\pi^0 \rightarrow \gamma + \gamma \tag{2.4}$$

The second most probable decay mode ($\sim$ 1%) is into a photon and an electron-positron pair [11].

2.2 Coherent Pion Photoproduction

Pion photoproduction occurs when a photon interacts with a nucleon and the reaction mechanism results in the emission of a pion in the final state. There are four possible channels for this reaction:

$$\gamma + p \rightarrow p + \pi^0 \tag{2.5}$$

$$\gamma + p \rightarrow n + \pi^+ \tag{2.6}$$

$$\gamma + n \rightarrow p + \pi^- \tag{2.7}$$

$$\gamma + n \rightarrow n + \pi^0 \tag{2.8}$$

Photoproduction can occur on a free nucleon (for example, the proton nucleus of an hydrogen atom) or, for heavier elements, on one of the nucleons bound within a nucleus. For heavier nuclei a coherent production process occurs only if the target nucleus is left in its ground state, $A_{gs}(\gamma, \pi^0)A_{gs}$. If the initial and final states differ, $A_{gs}(\gamma, \pi)A*$, the process is incoherent. Because of charge conservation, reactions involving charged pions leave the target nucleus in a different state from the original. Therefore, the only coherent production possible is the one featuring neutral pions [2].

For the photon energy ranges analysed in this experiment, the π^0 production process occurs with close to an equal probability for both protons and neutrons [12]. In the case of a coherent reaction there is insufficient quantum information to identify which nucleon or shells of nucleons contributed to the reaction mechanism, therefore the amplitudes from all nucleons add coherently. The resulting production cross section, neglecting any final state interactions, is then directly proportional to the square of mass number A and the square of the matter form factor $|F_m(q)|^2$. In this Plane Wave Impulse Approximation (PWIA) the cross section σ is expressed as [13]:

$$\frac{d\sigma}{d\Omega} = A^2 \frac{q}{k_\gamma} P_3^2 |F_m(q)|^2 sin^2(\theta_\pi) \tag{2.9}$$

where q is the momentum transfered to the nucleus, k_γ is the momentum of the photon, P_3 is the contributing pion photoproduction amplitude, Ω is the solid angle and θ_π is the pion scattering angle [14]. The matter form factor is a Fourier transform of the matter density distribution and, because of that, a diffraction pattern can be observed in the differential cross section.

The use of photons to study the neutron skin potentially allows for a much more accurate measurement to be obtained than from using strongly interacting probes. The strength of the photon's electromagnetic interactions is very weak and as such it is not affected by initial state interactions (ISI). Furthermore, many-body interaction effects do not complicate the interpretation of the data obtained. The results derived from the use of electromagnetic probes are less

susceptible to systematic effects in their theoretical interpretation [2] because electromagnetic interactions are far better understood than strong interactions.

Despite the photon probe in the entrance channel being completely unaffected by strong interactions, the photoproduced pions are strongly interacting particles and therefore the effect of the final state interactions (FSI) with the nucleus has to be accounted for. The real part of the pion-nucleus interaction is responsible for a shift in the (γ, π^0) angular distribution. The imaginary part, taking the absorption processes into account, explains the reduction in the flux [14]. It has been previously shown that the strength of the FSI scales with the pion energy and the pion-nucleus scattering cross section is dominated by the $\Delta(1232)$ resonance corresponding to a pion energy of ~ 165 MeV. Photoproduced pions with energies away from the peak of the resonance have weaker interaction with the nucleus.

Although the FSI complicates the analysis of the matter distribution in the nucleus, they also provide a very effective way to study pion-nucleus interactions across the whole volume of the nucleus. All the available information about the pion-nucleus interaction comes from charged pions scattering experiments with incident pion energies above a few 10's of MeV. However, the coherent π^0 production is not constrained by the limitations of charged-pion scattering experiments. It offers an opportunity to investigate the pion-nucleus interactions for pion energies nearing 0 MeV evaluated over the entire volume of the nucleus [2]. Therefore as well as studying the reaction at low pion energies, where the pion-nucleus interaction is minimised, it is also useful to go to higher energies where new constraints on these processes can be obtained.

The study of coherent π^0 photoproduction provides therefore a unique way to test not only nuclear matter distribution but pion-nucleus interactions as well. The main objective of the experiment presented in this thesis is however the use of coherent π^0 photoproduction as means for studying the nuclear matter distribution of tin isotopes, in order to determine how the neutron skin thickness depends on the mass number. The current predictions for neutron skin thicknesses of tin isotopes are presented in Fig. 2.1.

Across an isotopic chain of tin which ranges from $A = 112$ to $A = 124$, we expect a change in the neutron skin of ~ 0.05 fm. The precision necessary in order to study this expected change should be achievable through a measurement of coherent pion photoproduction.

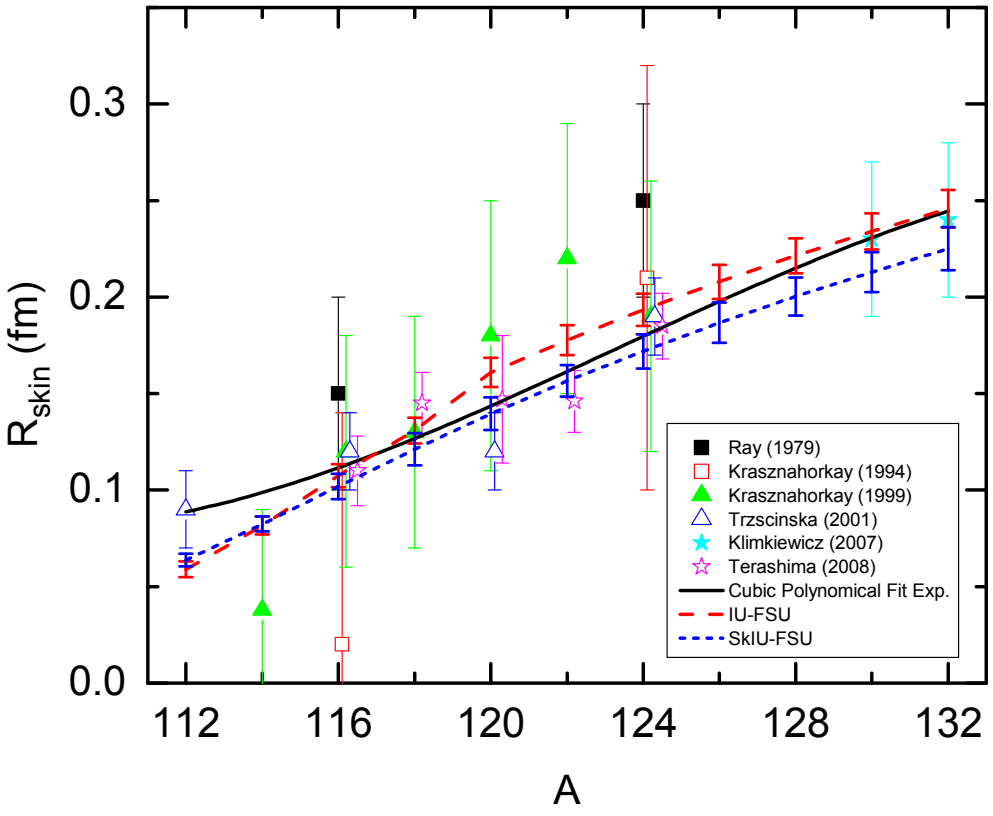

Figure 2.1: The predictions of the neutron skin thicknesses for tin isotopes from the IU-FSU and SkIU-FSU models after the optimization compared to those determined with different experimental methods [15].

2.2.1 Reaction Kinematics

The kinematic variables relevant to pion photoproduction are shown in figure 2.2. The interacting particles, the photon (γ) and the nucleon (N) have initial four-momenta of k and p_i respectively. The four-momentum is a combination of the particle's energy and its three-momentum: $P = (\vec{p}, E)$. The final state particles, π and nucleon (B), have the respective four-momenta q and p_f. The θ_{CM} is the pion scattering angle in the centre-of-mass frame of reference.

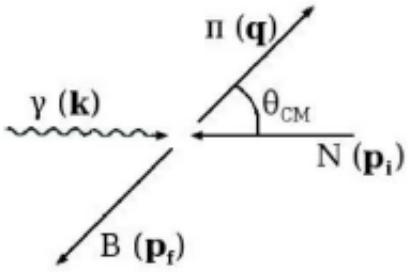

Figure 2.2: Simple diagram of a photoproduction reaction [16].

The Feynman diagrams (Fig. 2.3) illustrate that this reaction can proceed via three possible mechanisms. The first diagram (s-channel) describes a process where photon and nucleon combine into an intermediate particle (resonance), which eventually decays into two final state particles. In the case of t-channel, one of the interacting particles emits an intermediate particle, which is subsequently absorbed by the other interacting particle. The u-channel describes the same situation as the t-channel with the difference that the final state particles are interchanged.

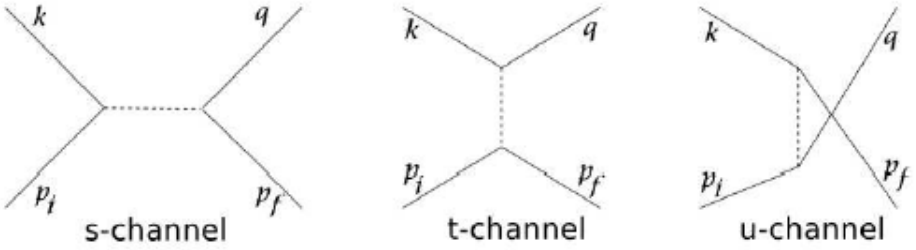

Figure 2.3: Feynman diagrams of the s-channel, t-channel and u-channel. For coherent π^0 only s- and u-channels are possible.

The kinematics of any such production reaction can easily be described with the use of the Lorentz-invariant Mandelstam variables s, t and u, which define the relative channel (Fig. 2.3). They are defined in terms of the four-momenta between the two vertices of the diagram as [17]:

$$s = (k + p_i)^2 = (q + p_f)^2 \tag{2.10}$$

$$t = (p_i - p_f)^2 = (k - q)^2 \tag{2.11}$$

$$u = (p_i - p_f)^2 = (k - p_f)^2 \tag{2.12}$$

Since all these diagrams share the same initial and final states, each channel defines some property of the reaction: s is the square of the energy of the reaction, t is the square of the momentum transfer, while the sum of the squares of the masses of particles is defined as a linear combination of those three variables.

$$s + t + u = \sum m_i^2 \tag{2.13}$$

Only two of the Mandelstam variables are necessary to fully describe these reactions. In the relativistic approximation, $mc^2 << E$, these variables can be written as:

$$s = 4p^2 \tag{2.14}$$

$$t = 2p^2(1 - cos\theta_{CM}) \tag{2.15}$$

$$u = 2p^2(1 + cos\theta_{CM}) \tag{2.16}$$

where θ_{CM} is the pion scattering angle in the center of mass frame of reference. If s is fixed, t is a linear function of $cos\theta$, and therefore, the scattering functions for π^0 can be represented completely in terms of s and $cos\theta$ [18].

2.2.2 The Cross Section for Pion Photoproduction

The angular distribution of a pion, or any other meson created in a photoproduction process, can be represented by a differential cross section:

$$\frac{d\sigma}{d\Omega} = |A(s, cos\theta)|^2 \tag{2.17}$$

The probability of the transition from a given initial state $\langle i|$ to another final state $|f\rangle$ can be represented by a scattering matrix S in the Bjorken-Drell notation [19]:

$$S_{fi} = \delta_{fi} - \frac{i}{(2\pi)^2}\delta^4(q - k + p_f - p_i)\sqrt{\frac{m_N^2}{4E_\gamma E_\pi E_i E_f}} < i|T|f > \tag{2.18}$$

where T is the transmission matrix relating initial and final states, m_N is the mass of a nucleon, and q, k, p_i, p_f are the four-momenta of the particles involved. The transmission matrix T describes the amplitude of the photoproduction process, and can be written as:

$$T = \epsilon_\mu J_\mu \tag{2.19}$$

where ϵ_μ is the photon polarization vector and J_μ is the electromagnetic current of a nucleon. Then the differential cross section can be defined as:

$$\frac{d\sigma}{d\Omega} = \frac{q}{k}\left(\frac{m_N}{4\pi W}\right)^2 \sum |T| \tag{2.20}$$

where W is the invariant mass of the system.

The electromagnetic current of a nucleon J, as proposed by Chew, Goldberg, Low, Nambu (CGLN), can be written in terms of nucleon spin matrices σ, and the meson unit vectors $\hat{\mathrm{q}}$ and $\hat{\mathrm{k}}$ [20]:

$$J = \frac{q}{k}\frac{4\pi W}{m_n}(i\sigma F_1 + (\sigma \cdot \hat{k})(\sigma \times \hat{q})F_2 + i\bar{k}(\bar{\sigma} \cdot \hat{q})F_3 + i\bar{k}(\sigma \cdot \hat{k})F_4) \tag{2.21}$$

where

$$\bar{\sigma} = \sigma - (\sigma \cdot \hat{q})\hat{q} \tag{2.22}$$

$$\bar{k} = \hat{k} - (\hat{k} \cdot \hat{q})\hat{q} \tag{2.23}$$

and F_1, F_2, F_3, F_4, known as CGLN amplitudes, are the structure functions of energy and scattering angle, which can be written in terms of electric and magnetic multipoles and angular momentum through a partial wave expansion as:

$$F_1(\theta) = \sum_{l=0}^{\infty}(lM_{l+} + E_{l+})P'_{l-1}(cos\theta) + ((l+1)M_{l-} - E_{l-})P'_{l-1}(cos\theta) \tag{2.24}$$

$$F_2(\theta) = \sum_{l=0}^{\infty}((l+1)M_{l+} + lM_{l-})P'_l(cos\theta) \tag{2.25}$$

$$F_3(\theta) = \sum_{l=0}^{\infty}(E_{l+} - M_{l+})''_{l+1}(cos\theta) + (E_{l-} + M_{l-})P"_{l-1}(cos\theta) \tag{2.26}$$

$$F_4(\theta) = \sum_{l=0}^{\infty}(M_{l+} - E_{l+} - M_l - E_{l-})P''_l(cos\theta) \tag{2.27}$$

where P'_l and P''_l are derivatives of a Legendre polynomials, l is the relative orbital momentum of a meson, $E_\pm$ and $M_\pm$ are electric and magnetic transitions respectively, and the $+$ or $-$ determines whether the spin of the baryon should be added or subtracted.

The total angular momentum of a nucleon is $\frac{1}{2}$, and the total angular momentum of an incident photon is L_γ. In order to satisfy the selection rule the resulting spin of a resonant state, denoted with a $*$, has to obey the following relation [21]:

$$\left|L_\gamma - \frac{1}{2}\right| < J_{N*} < \left|L_\gamma + \frac{1}{2}\right| \tag{2.28}$$

and the parity is given as:

$$\pi_{N*} = \pi_N\pi_\gamma \tag{2.29}$$

where, π_N, parity of a nucleon, is equal to 1, and π_γ, the parity of the photon is equal to:

$$\pi_\gamma = (-1)^{L_\gamma} \tag{2.30}$$

$$\pi_\gamma = (-1)^{L_\gamma+1} \tag{2.31}$$

respectively for an electric and magnetic multipoles.

The selection rules for the angular momentum and parity of the resonant state with respect to the outgoing meson are given as:

$$\left|L_\pi - \frac{1}{2}\right| < J_{N*} < \left|L_\pi + \frac{1}{2}\right| \tag{2.32}$$

$$\pi_{N*} = \pi_N\pi_\pi(-1)^{L_\pi} = (-1)^{L_\pi+1} \tag{2.33}$$

where π_π is -1.

Combining the above equations sets a limit to the spin and parity of the resonance:

$$\left|L_\gamma \pm \frac{1}{2}\right| < J_{N*} < \left|L_\gamma \pm \frac{1}{2}\right| \tag{2.34}$$

$$\pi_{N*} = \pi_{N\gamma} = (-1)^{L_\pi+1} \tag{2.35}$$

When a cross section is dominated by a single resonance, its quantum numbers are reflected in the angular distribution because of the dependence of the Legendre polynomials in the CGLN amplitudes. This means that the electric ($L = L_\pi \pm 1$) and the magnetic ($L = L_\pi$) multipoles, the spin and parity are related to the angular distribution of mesons. Most photoproduction mechanism, however, have more than one multipole contributing to the resonance and in order to distinguish between the different contributions, several channels must be investigated.

Isospin is not conserved in the electromagnetic interactions but is conserved in the hadronic interactions. The isospin of the initial state, determined from the isospin of the nucleon, is $I_i = \frac{1}{2}$ while the contributions from the pion and nucleon's isospins determine the value of the isospin of the final state, I_f, which can therefore take the values of $\frac{1}{2}$ or $-\frac{1}{2}$. The value is determined by the photon, which behaves as a linear combination of an isoscalar (I_s), which conserves the isospin, and an isovector (I_v), which can change the isospin by one. The whole system can then be described by the three isospin amplitudes [22]:

$$A^0 =< \frac{1}{2}, I_3|I_s|\frac{1}{2}, I_3 > \tag{2.36}$$

for the isoscalar electromagnetic current, and:

$$A^1 =< \frac{1}{2}, I_3|I_v|\frac{1}{2}, I_3 > \tag{2.37}$$

$$A^3 =< \frac{3}{2}, I_3|I_v|\frac{1}{2}, I_3 > \tag{2.38}$$

for the isovector electromagnetic current.

As defined by *M.Dehn et al.* in [23], if the amplitudes are written as:

$$A^+ = \frac{A^1 + 2A^3}{3} \tag{2.39}$$

$$A^{-} = \frac{A^1 - A^3}{3} \tag{2.40}$$

the physical amplitudes for pion photoproduction can be expressed as:

$$A(p\gamma \to p\pi^0) =< p\pi^0|I|p\gamma >= (A^0 + A^+) \tag{2.41}$$

$$A(n\gamma \to n\pi^0) =< n\pi^0|I|n\gamma >= (A^+ + A^0) \tag{2.42}$$

$$A(p\gamma \to n\pi^+) =< n\pi^+|I|p\gamma >= \sqrt{2}(A^0 + A^-) \tag{2.43}$$

$$A(n\gamma \to p\pi^-) =< p\pi^-|I|n\gamma >= \sqrt{2}(A^0 - A^-) \tag{2.44}$$

The above set of equations allows for the separation of the amplitudes for individual photoproduction reactions provided that the measurements on both proton and neutron targets are carried out.

2.2.3 The Photoproduction Amplitude on the Nucleon

A key element in any calcaultion of the coherent pion photoproduction process on a nucleus is the underlying amplitude for production from a nucleon. This amplitude is obtained by fitting the model of the photoproduction process to the wealth of experimental data available for pion photoproduction from a nucleon target. In general, such reactions are also studied to constrain the nucleon excitation spectrum. However for the energy range of interest in this thesis only the first excited state of the nucleon, the Δ, gives a significant contribution. Information on the production amplitude, including information on the masses and widths of the contributing resonances is obtained from the fit to experimental data. A range of different approaches to the reaction models have been developed and used. The most common approach involves the separation of background and resonant terms from the transition matrix.

Considering a reaction of the form $A \to B \to C$, where A is the initial state of the nucleon-photon system, B is the intermediate resonant state and C is the final state of the nucleon-meson system, the photoproduction process can be described by the Hamiltonian below:

$$H = H_0 + V_{bg} + V_R(E) \tag{2.45}$$

where H_0 is a free Hamiltonian expressing the total kinetic energy of the

interacting particles, V_{bg} is the potential due to the background created by the non-resonant contributions to the reaction, and $V_R(E)$ is potential due to the resonant term.

The transition matrix for the process is given by [24]:

$$T_{AC} = V_{AC} + \sum_{B} V_{AC} g_B(E) T_{BC}(E) \tag{2.46}$$

where g_B is the propagator of channel B for the reaction, and $\sum_{B}$ sums all the possible channels of the reaction $A \rightarrow C$ via B. Alternatively, the transition matrix can be split into the background and resonant terms, allowing the calculations for the background and resonant contributions to be carried out independently.

$$T^{AC} = t_{bg}^{AC} + t_{R}^{AC}(E) \tag{2.47}$$

Partial wave analyses (PWA) are methods that allow the background and resonant terms of the transmission matrix to be decomposed into a number of partial waves of defined multipolarity and momentum. Generally, the resonant terms are modelled by a Breit-Wigner form while the background terms are described by Born terms and vector-meson contributions(Fig. 2.4). The extraction of the parameters from the analysis is done in a two-stage procedure of fitting the experimental data [24].

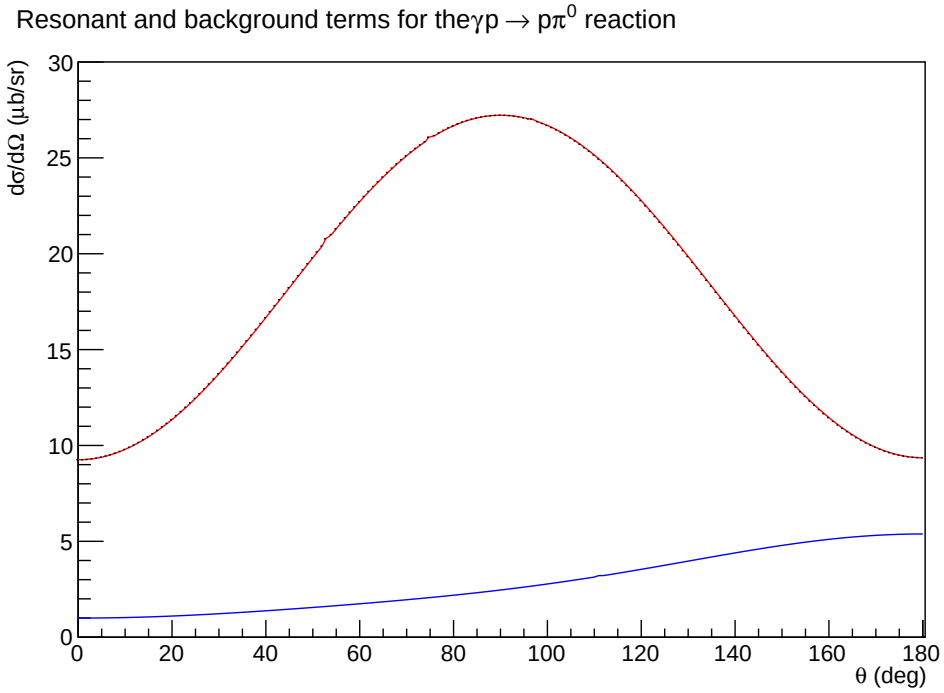

Figure 2.4: An example of a differential cross section of a resonance modeled with Breit-Weigner distribution in red and non-resonant terms described by Born terms and vector-meson contributions obtained from MAID2007 model in blue [25].

The most commonly used processes for the pion photoproduction PWAs are MAID, developed at the University of Mainz [26], SAID written by the CNS Data Analysis Center at George Washington University [27] and Bonn-Gatchina (BnGa) framework written by the collaboration of the Universitaet Bonn, Germany and Petersburg Nuclear Physics Institute in Gatchina, Russia. Detailed explanation of MAID can be found in [26, 28] SAID in [27, 29] and BnGa in [30, 31, 32].

MAID is a unitary isobar model which describes the transmission matrix through a single πN channel [28]:

$$T_{\gamma\pi} = V_{\gamma\pi}(E) + V_{\gamma\pi}(E) g_0 T_{\pi N}(E) \tag{2.48}$$

where $V_{\gamma\pi}$ is the transition potential of the $\gamma N \to \pi N$ reaction, $T_{\pi N}$ and g_0 are the scattering matrix and the free propagator of the πN interaction respectively.

The scattering matrix and the transition potential can be broken down into its constituents: background and resonant terms, which can be expanded as partial waves. The resonances included in MAID, are classified as 4* by the Particle Data Group (PDG) [33], however, MAID can only fit the reconances up to $2GeV$.

In the methods developed for SAID, there are no assumptions about resonances and channels included in the analysis framework. The transmission matrix, defined for the following three channels: γN, πN and $\pi\Delta$ (covering all open channels), can be written as [29]:

$$T_{\gamma\pi} = A_1(1 + iT_{\pi N}) + A_R T_{\pi N,\pi N} \tag{2.49}$$

where A_R parametrizes the multipole amplitudes of the resonant terms, and A_1 parametrises the background.

$$A_R = \frac{m_\pi}{q}\left[\frac{k}{q}\right]^l \sum_{n=0}^{N} p_n \left[\frac{E_\pi}{m_\pi}\right] \tag{2.50}$$

$$E_\pi = \frac{s - (m_\pi + M)^2}{2M} = E_\gamma - m_\pi\Big(1 + \frac{m_\pi}{2M}\Big) \tag{2.51}$$

where E_π is the pion kinetic energy in the lab frame for the $\pi N \to \gamma N$, s is the square of the center of mass energy, M is the mass of the nucleon. E_γ is the energy of the photon in the lab frame of reference for the $\gamma N \to \pi N$ reaction, and p_n is a free parameter determined from the fit to the experimental data.

$$A_1 = A_B + A_Q \tag{2.52}$$

where, A_B is a partial wave of a pseudoscalar Born amplitude, and A_Q is a Legendre function.

The BnGa approach uses the amplitudes obtained by SAID together with data on the $\pi p \to \pi^0\pi^0 n$ and a set of data on π induced reactions as Jülich-Bonn framework [34, 35]. The BnGa framework, relying on a fully relativistically invariant operator expansion method combining the analysis of different reactions by imposing analiticity abd unitary constraints directly, uses pion0- and phot-induced reactions and determine the properties of the contributing resonances in global fits to all included data [32].

The MAID model is employed for the nucleon photoproduction amplitude in the coherent pion photoproduction model used in this thesis. However, for

the photon energy range of interest, in the Δ region, both MAID and SAID approaches give results consistent to within $\pm 5\%$.

2.3 The DKT Theoretical Model for Coherent Pion Photoproduction

The simplest model describing the pion photoproduction is the plane wave impulse approximation (PWIA), which assumes that the photon-nucleon interactions can be simplified to a photon coupling to a single nucleon and neglecting all the interactions with other nucleons (impulse approximation). In the plane wave approach the pion-nucleus FSI in the final state is neglected. The differential cross section for the coherent photoproduction in the PWIA approximation can be written simply as in equation 2.9. For nuclei with zero spin, as studied in this thesis, the spin-dependent terms cancel and the differential cross section can be rewritten in the form:

$$\frac{d\sigma}{d\Omega} = \frac{q}{2k_\gamma} \left|F_2(E_\gamma, \theta_\pi)\right|^2 sin^2(\theta_\pi) \tag{2.53}$$

where F_2 is the CGLN amplitude (see equation 2.25), q is the momentum of the pion and k is the momentum of the photon in the centre of mass frame of reference.

It has been shown that these calculations approximate the coherent pion photoproduction well in the range of low photon energies near the reaction threshold. However, at higher photon energies, the pion FSI become more important and the PWIA model no longer gives a good description of the data [36].

The extension of the PWIA model, which includes the description of FSI for the pion-nucleus system is called the distorted wave impulse approximation (DWIA). As with the PWIA, the impulse approximation is used to describe the interactions, however, the plane wave of the outgoing pion is modified to include the FSI in a form of distortion (change in wavelength and amplitude) to the plane wave. The first DWIA calculations involved solving a Klein-Gordon equation in the coordinate space with an optical potential, where the parameters were taken from experiments on scattering and the capture of mesons by nuclei [37]. The

more recent calculations [38] however, have been done in the momentum space, which simplifies the transformations between pion-nucleon and pion-nucleus CoM frames of reference. The pion-nucleus interaction is modelled using a momentum space second order complex potential, whose parameters are extracted from a global fit to the wealth of pion-nucleus scattering experimental data [38]. The first order term is proportional to the single nucleon radial nucleon density. The second-order potential adds a term proportional to the square of the single nucleon radial densities and models the interaction of pions with more than one nucleon. The 4 parameters describing the 2 complex amplitudes in the potential are extracted from fits to the scattering data on light nuclei (^{6}Li, ^{12}C, ^{16}O, ^{32}Si and ^{40}Ca) [39]. However, with the increasing pion momentum, the significance of the Δ excitaton rises and the FSI description by the optical potential no longer suffice to explain the observed effects. In the calculations by Dreschel, Kamalov and Tiator, the DKT model, the effect of the Δ resonance, both in the pion photoproduction amplitude and in the final state pion-nucleus interaction are treated in a unitary way employing a Δ self-energy. The parameters of the self-energy are extracted from fits to the data on lighter nuclei where they were found to show an A independence [13].

The theoretical calculations of coherent pion photoproduction for this analysis were made using the DKT theoretical model, where the distortions of the outgoing pion waves are described by the optical potential of the second order calculated in the momentum space [38]. In this model, the initial pion photoproduction amplitudes on the nucleon are taken from the MAID [28] parameterization. The distributions of the protons and neutrons in the target are input in the form of a 2 parameter Fermi function for the matter distribution.

The DKT calculations use the matter form factor for the appropriate nucleus (Fourier transform of the radial matter density distribution) as an input. The calculations are done under the assumption that both, matter and charge density distributions, $\rho(r)$, can be parametrised as symmetrised Fermi functions (Fig. 2.5):

$$\rho(r) = \rho_0 \frac{sinh\left(\frac{c}{b}\right)}{cosh\left(\frac{c}{b}\right) + cosh\left(\frac{r}{b}\right)} \tag{2.54}$$

where b is the diffuseness parameter, c is the half height radius and ρ_0 is defined as:

$$\rho_0 = \frac{3}{4\pi c^3}\left(1+\frac{\pi b}{c}^2\right)^{-1} \tag{2.55}$$

Then the root mean square radius, r_{rms}, of the distribution is expressed as:

$$r_{rms} = \frac{3c^2}{5}\left(1+\frac{7}{3}\left(\frac{\pi b}{c}\right)^2\right) \tag{2.56}$$

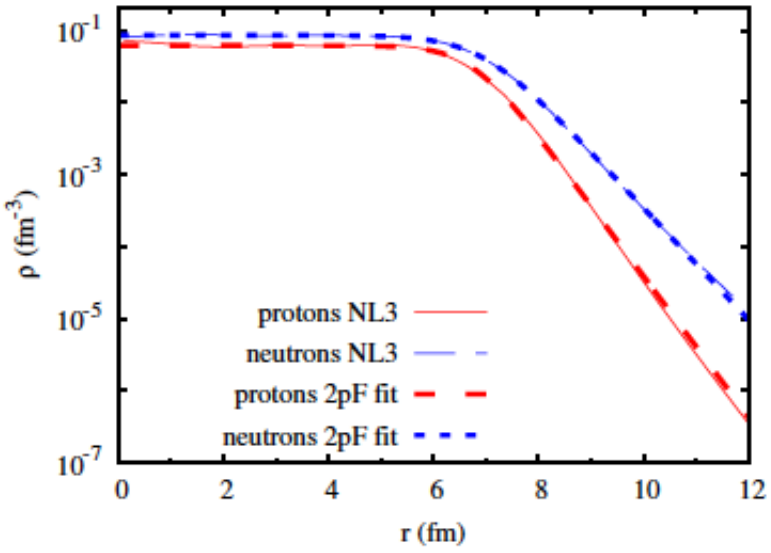

Figure 2.5: Two parameter Fermi (2pF) densities (Eq. 2.54) fitted to the proton and neutron densities calculated for ^{208}Pb with the NL3 parameter set [40].

The matter and charge distributions used in the calculations for this thesis come from those recently provided by J. Piekarewicz RMF parameter set FSUGold [41]. The parameter set FSUGold introduces an isoscalar-isovector coupling term Λ_v, which simulates the density dependence of the symmetry energy [42]. This parameter set has already been used and tested in the studies of the neutron skin of heavy nuclei [43], the equation of state for tin isotopes [44] and the investigation into different models of nuclear structure [45].

The DKT model predictions have been made for discrete values of photon energies in the E_γ range of $180 - 240$ MeV in 2 MeV steps. The data from this photon energy region is chosen for analysis to ensure that the model is used

in kinematic regions where the pion-nucleus interaction model has already been fitted to data (there is sparse data below ~ 20 MeV pion energy). The results of the DKT calculations for different targets are shown in figures 2.6 - 2.8. There are some clear general trends to the predictions. As would be expected, the location of the minima moves to smaller angles as the matter radius increases. These changes are already evident in the first minima. However, the accumulating change in the matter radius has a more pronounced effect on the higher order minima. The heights of the first maxima show a small sensitivity to the matter radius, as the cross section is increased the matter radius of the target becomes smaller. The relative heights of the first two maxima are expected to be sensitive to the diffuseness of the matter distribution.

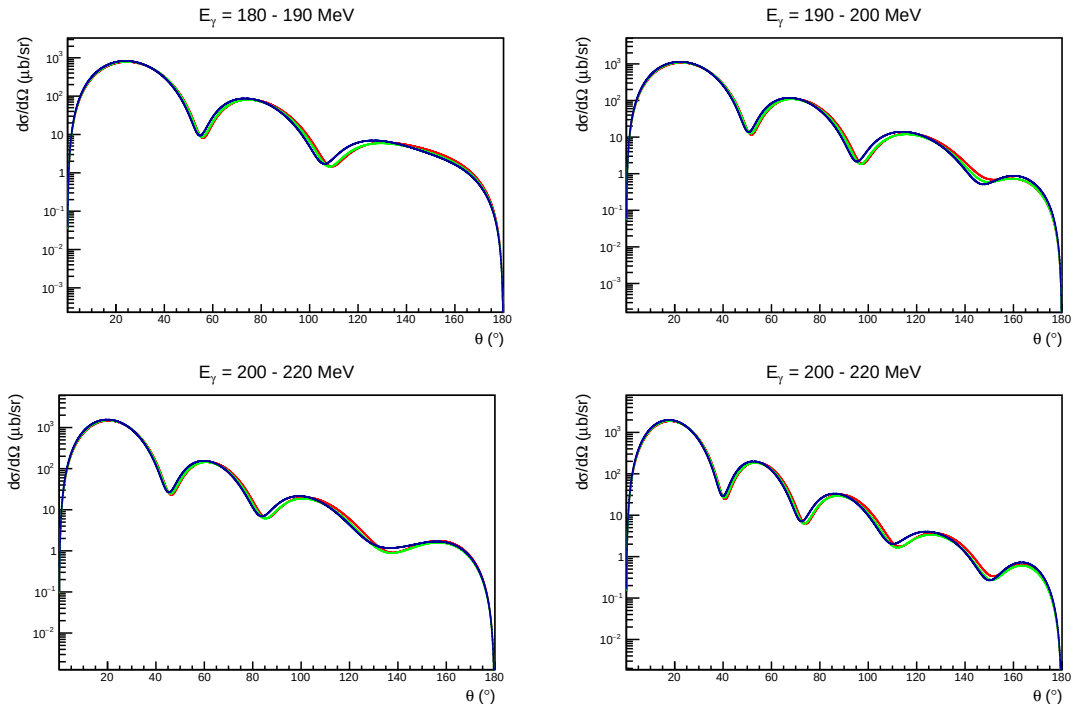

Figure 2.6: DKT calculations of the cross sections for different targets and different E_γ using the FSUGold parameters set (FSUGold corresponds to FSU030 [41]). The red line is for the ^{116}Sn isotope, the green line is for the ^{120}Sn isotope and the blue line shows the ^{124}Sn isotope.

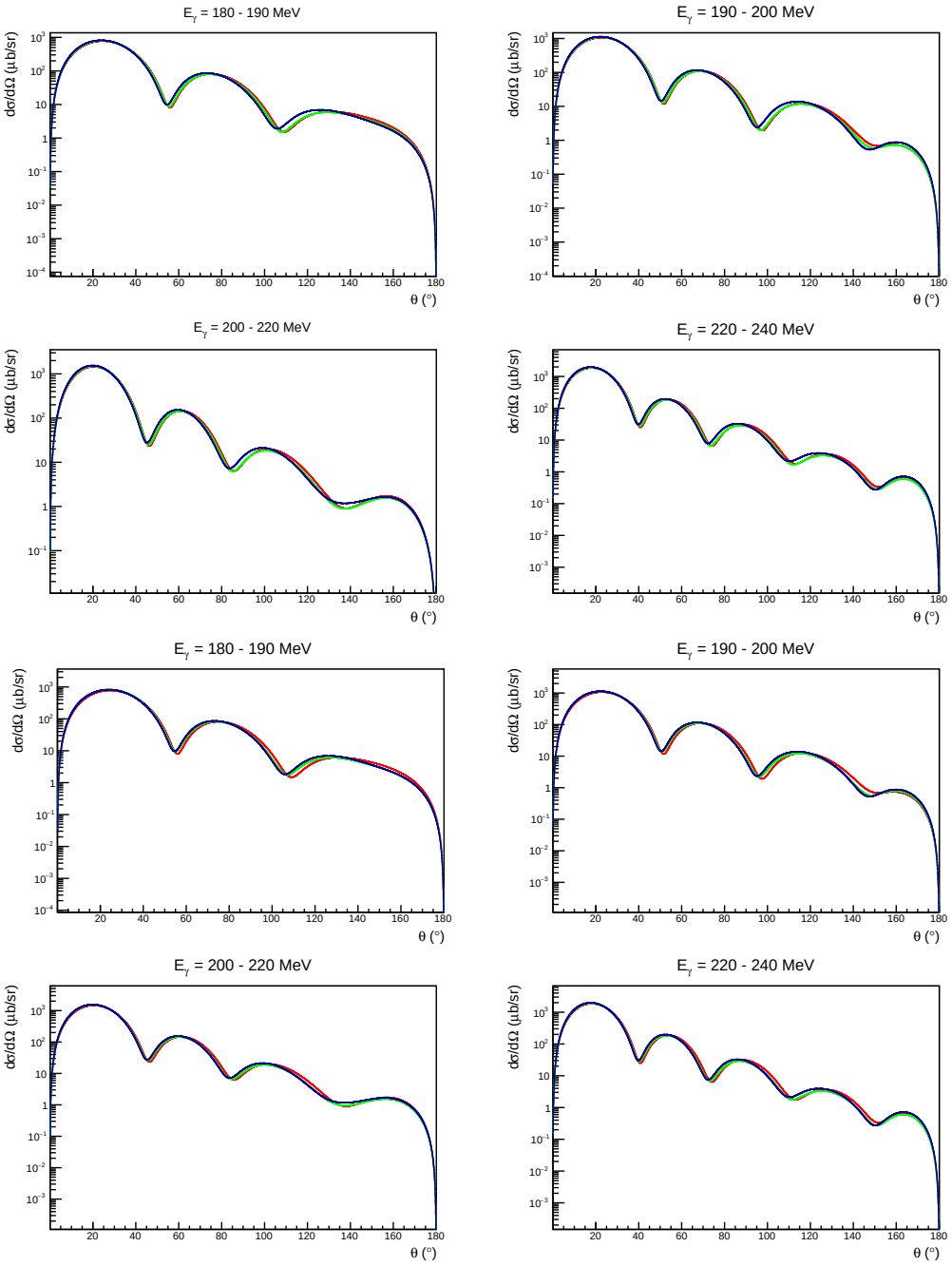

Figure 2.7: DKT calculations of the cross sections for different targets and different E_γ using the investigated values for the FSUGold parameters sets: FSU000 and FSU010. The red line is for the ^{116}Sn isotope, the green line is for the ^{120}Sn isotope and the blue line shows the ^{124}Sn isotope. Top four panels show the results for the FSU000 and bottom four panels show the results for FSU010.

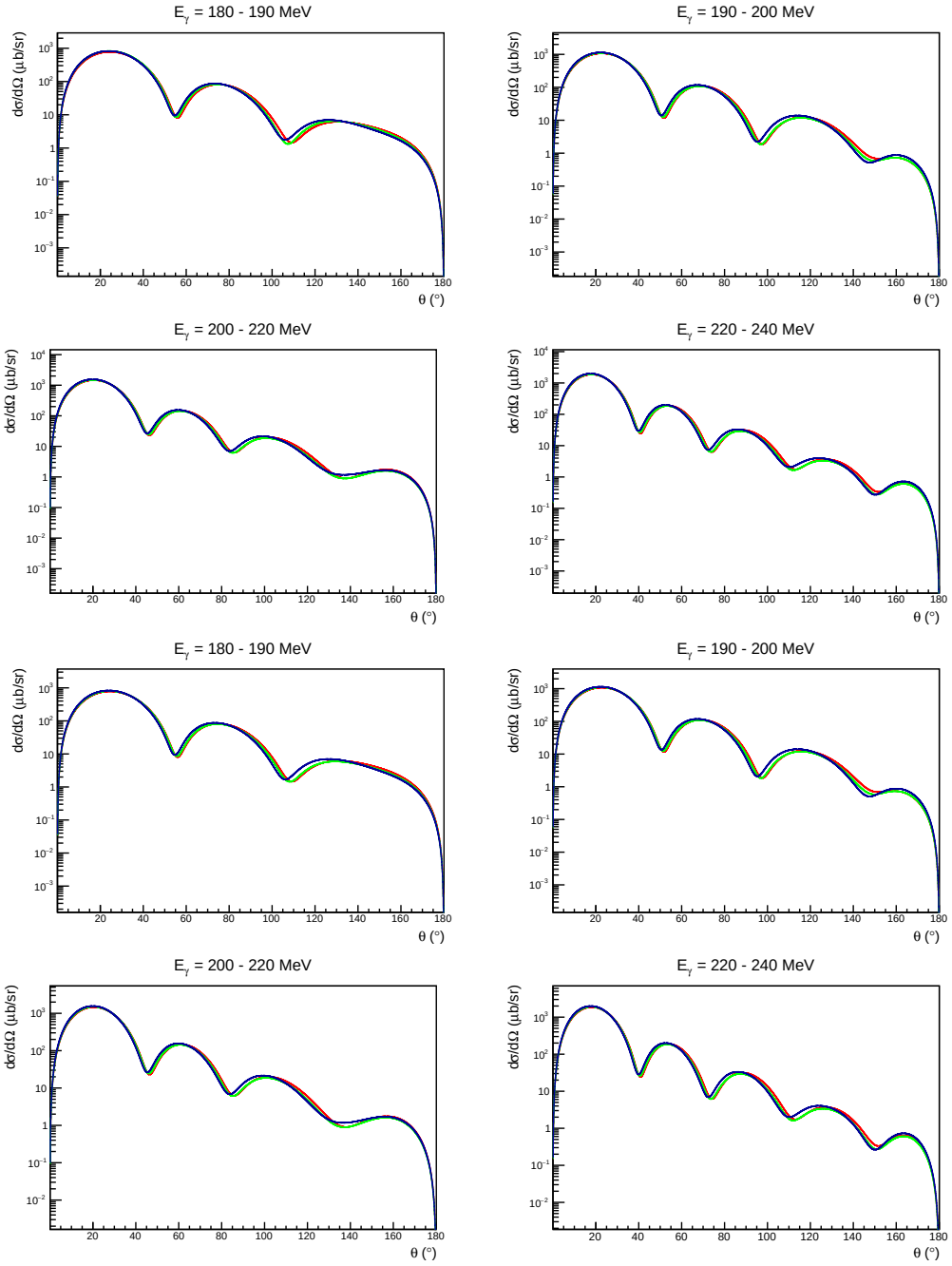

Figure 2.8: DKT calculations of the cross sections for different targets and different E_γ using the investigated values for the FSUGold parameters sets: FSU020 and FSU040. The red line is for the ^{116}Sn isotope, the green line is for the ^{120}Sn isotope and the blue line shows the ^{124}Sn isotope. Top four panels show the results for the FSU020 and bottom four panels show the results for FSU040.

2.3.1 The Nuclear Equation of State

An accurate measurement of the neutron skin provides constraints on the nuclear equation of state. An outline of what the equation of state represents is given in this section.

The equation of state (EOS) is a function of the matter's density (ρ) and the isospin asymmetry (α) and is expressed as the energy (E) per nucleon in an infinite piece of nuclear matter, $\frac{E}{A}(\rho, \alpha)$ where α is expressed as:

$$\alpha = \frac{N - Z}{A} \tag{2.57}$$

where, N is the number of neutrons, Z is the number of protons and A is the atomic mass number. α takes values of -1 for prton matter, 1 for neutron matter and 0 for symmetric matter.

The Bethe-Weizsaecker mass formula, more commonly known as semi-empirical mass formula (SEMF), is based on the theory of the liquid drop model and was first proposed in 1935 to explain the various properties of an atomic nucleus. According to this formula, the binding energy, E_B can be approximated as:

$$E_B = a_V A - a_s A^{\frac{2}{3}} + a_C \frac{Z^2}{A^{\frac{1}{3}}} - a_A \frac{(A - 2Z)^2}{A} - \delta(A, Z) \tag{2.58}$$

where a_V is the volume coefficient (based on the strong force), a_S (also based on the strong force) is the surface term, which provides a correction to the volume term and a_C is the Coulomb or electrostatic term which introduces a correction due to electrostatic repulsion between protons. a_A is the asymmetry coefficient, which is based on the Pauli exclusion principle, and accounts for the imbalances between numbers of proton and neutrons in a nucleus. The pairing term $\delta(A, Z)$ covers the effects of spin-coupling [18].

This formula, which is one of the first and most widely used equation of states, gives a good description of nuclear matter at nuclear densities. However, the model is not applicable at non-nuclear densities as the parameters are obtained from fitting nuclear data, which has a relatively constant density of around 0.18 gcm^{-3}. For matter at higher or lower densities a more general description of the equation of state is required. Accurately constraining the asymmetry coefficient is one of the most important studies in the fields of nuclear and particle physics

and would allow extrapolation to nuclear matter at higher densities, such as in neutron stars.

As mentioned before, an accurate measurements of the neutron skin could potentially put tighter constraints on the asymmetry term of the EOS and its dependence on density, allowing a better description of the properties of assymetric and high density matter, for example, the environment inside neutron stars. There are a number of recent theoretical papers where a linear relationship between the neutron skin thickness of a heavy asymmetric nucleus and these parameters is established [46]. This relationship appears to be robust and shows little nuclear model dependence, with relativistic mean field and Skyrme Hartree Foch models giving predictions, which lie near to the linear dependence (Fig. 2.10).

In the case of a symmetric nuclear matter (i.e. for $\alpha = 0$), EOS can be expanded about the nuclear saturation density (ρ_0) [47] as:

$$E(\rho, \alpha) = E(\rho, 0) + S_2(\rho)\alpha^2 + S_4(\rho)\alpha^4 + O(\alpha^6) \tag{2.59}$$

where ρ is the nucleon density, S_2 is the symmetry energy (defined in the equation 2.62) and ρ_0 is defined as:

$$\rho_0 - \frac{\partial S}{\partial \rho}|_{\rho=\rho_0} \equiv S_2'(\rho_0) \tag{2.60}$$

$$E(\rho, 0) = -\alpha_V + \frac{K_0}{18\rho_0^2}(\rho - \rho_0)^2 + O(\alpha^4) \tag{2.61}$$

$$S_2(\rho) = \alpha_4 + \frac{\rho_0}{\rho_0^2}(\rho - \rho_0) + \frac{\Delta K_0}{18\rho_0^2}(\rho - \rho_0)^2 + O(\alpha^4) \tag{2.62}$$

where, K_0 is the compression modulus of the nuclear matter, ΔK_0 is the correction to the incompresibilities and $\alpha_4 = S(\rho_0)$ is the symmetry energy at saturation density.

Even though K_0, ρ_0 and a_V do not show any correlation with the neutron skin thickness, the measurement done in [46] shows that the neutron skin thickness is directly correlated to the symmetry energy at the saturation density, $\alpha_4 = S(\rho_0)$. Figure 2.10 shows that the linear relationship between the neutron skin thickness and the symmetry energy α_4 is model independent. This correlation is also true for the nuclear saturation density. Therefore, an accurate determination of the

neutron skin thickness will provide constraints for both, the symmetry energy and its first derivative at saturation densities.

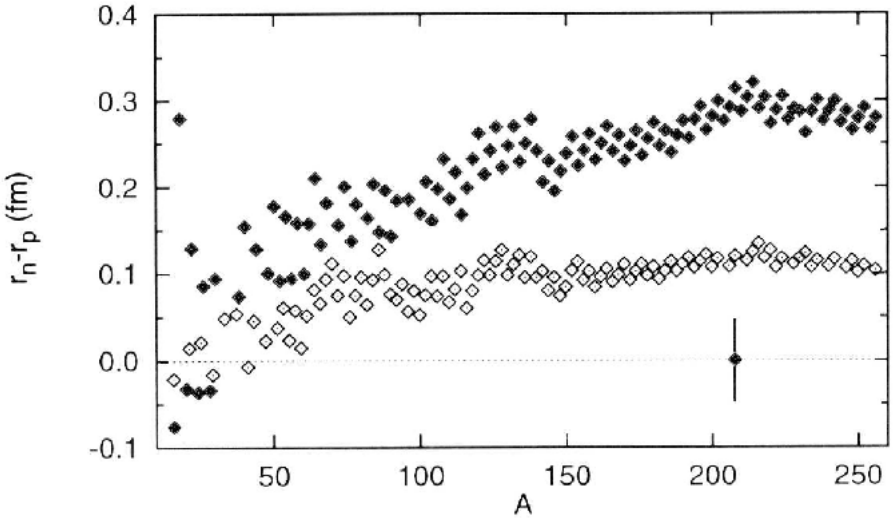

Figure 2.9: The variation of neutron skin thickness as predicted by different models. Filled markers are for the RMF theory calculations and unfilled markers show the predictions of the Skyrme forces. Taken from reference [48].

The model independent correlation between neutron skin thickness and the symmetry energy in the nuclear equation of state proves that an accurate measurement of the neutron skin would provide tighter constraints on the values of the symmetry energy and the nuclear saturation density. This would improve the accuracy of the EOS in describing neutron rich assymetric matter, for example in the case of neutron stars.

2.4 Nuclear Structure Theories

The central aim of the measurement in this thesis is to determine the properties of the neutron skin. This will constrain state-of-the-art nuclear theories. The current status of various nuclear theories will be described in this section.

Ever since the formulation of quantum mechanics, much of the research in the fields of nuclear and particle physics have been focused on the studies

of the structure of atomic nuclei. In those early times, the conventional theories treated the nucleus as a quantum mechanical many-body problem of Fermions interacting through a non relativistic two-body potential defined by the Schroedinger equation [49]. In reality, this approach is not applicable for any but the lightest nuclei because the many-body problem cannot be resolved analytically. However, other methods developed and used in recent years, such as variational Monte Carlo and Green's function Monte Carlo techniques, have been successfully employed to solve non-relativistic many-body problems for nuclei with mass numbers greater than 10 amu [50, 51]. For heavier nuclei those methods no longer hold and different approaches are required.

The Skyrme [52] or Gogny [53] interactions start off from the density dependent energy functions for iterative calculations of the Hartree-Fock. The parameters of these functions are then fitted to the experimental nucleon-nucleon scattering data.

The relativistic mean field (RMF) theory is a model of the nucleon-nucleon interactions assuming that nuclei are point-like particles described by Dirac spinors and all the interactions between them occur via mesonic fields. Even though there are many meson fields possible, most calculations only use the $\sigma(x)$, $\omega^{\mu}(x)$ and $\vec{\rho^{\mu}}(x)$ fields and the vector potential $A^{\mu}(x)$ due to the photon exchange between the nucleons in order to simplify the calculations [54]. Just like Skyrme and Gogny forces, RMF theory also uses the Hartree-Fock variational methods to resolve the nuclear wavefunctions.

Most of the existing models used to describe the structure of nuclei are based either on the RMF theories or on the Skyrme or Gogny interactions. However, even though various models offer a fair degree of consistency when reproducing general properties of nuclear matter such as the proton charge radius, masses and polarizabilities, they diverge when calculations of the neutron radius are considered [55, 48]. Fig. 2.9 shows the predictions from typical RMF and Skyrme nuclear structure models for the neutron skin of ^{208}Pb.

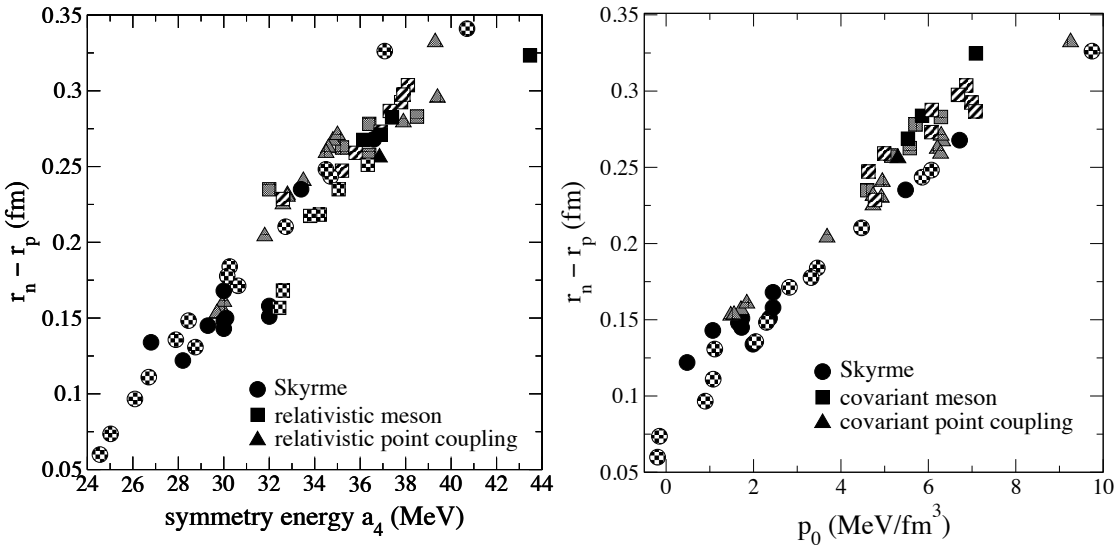

Figure 2.10: Plots of the relationship between neutron skin thickness and the symmetry energy for various models (left), and the linear dependence of the neutron skin and the nuclear saturation density (right) for ^{208}Pb. Figure taken from reference [46].

Rather than measuring an absolute value of the skin, the measurement of the evolution of the skin thickness across an isotopic chain is a favourable approach, both theoretically and experimentally. Particularly, this method allows some cancelation of systematic effects as the experimental measurements are all made with the same apparatus and the predicted change in the skin may be less sensitive to inaccuracies in the modelling. Figure 2.1 shows the theoretical predictions for the evolution of the neutron skin in tin isotopes from different theoretical models.

2.5 FSUGold

For the first interpretation of the data presented in this thesis the matter distributions input to the DKT model employed the FSUGold parameters. This is a nuclear relativistic mean field model fitted to the binding energies and charge radii of a number of magic nuclei [56]. The model parameters have been developed to also improve the theoretical predictions of the giant monopole resonance (GMR) and isovector giant dipole resonance (IVGDR) in ^{208}Pb. This functional is commonly employed in the literature. The earlier used NL3 model [57] has been suggested to reproduce the GMR in ^{208}Pb well only by accident [58, 59]. This hypothesis has been tested by calculating GMR for ^{90}Zr and IVGDR for ^{208}Pb, which values should be respectively over and underestimated by the NL3 model. The results proved that this was indeed the case, justifying the reason for developing a new accurately calibrated relativistic model - FSUGold. The main difference between the NL3 and FSUGold models is the introduction of two new isovector-isoscalar coupling parameters, ζ and Λ_v. Further details about the development of the FSUGold model can be found in [56].

2.6 Previous Neutron Skin Measurements

Neutron skin measurements have previously been attempted using a variety of techniques. A recent review of the experimental attempts to measure Δr_{np} in ^{208}Pb is given by in [7]. The main body of work uses strongly interacting probes such as protons, pions or heavy ion collissions. In very recent years some pioneering measurements using electromagnetic probes have appeared [2]. Most experimental work focuses on the measurements of ^{208}Pb because of its doubly magic nature and the resulting simplification in modelling its nuclear structure. For this reason, these past measurements on ^{208}Pb will be discussed first, followed by a discussion of the smaller number of measurements for tin isotopes.

Experiments involving polarised and unpolarised proton scattering have been carried out in a number of facilities. The angular distributions of the scattered protons contain information on the matter form factor of the nucleus. The matter distribution is sampled as the incoming probe interacts via the strong interaction with both protons and neutrons. The measured angular distributions have been fitted with theoretical models of the proton-nucleus scattering process, which

assume neutron radial distributions of varying size. The charge distributions in the model are either fixed to the experimentally determined values or take the values predicted by the nuclear model. The best fit combination is then used to determine the best matter distribution. As the charge distribution is known this can be used to extract the neutron skin thickness. Recent analyses have also used the sum of gaussians method to deconvolute the matter ditribution from the experimental data. The most recent global analysis [60] of proton scattering data gave Δr_{np}=0.21±0.06 fm for ^{208}Pb. However, a different theoretical analysis concludes that the method is not sensitive enough to determine the size or even the existence of the neutron skin [6].

A series of neutron skin measurements were also carried out at the Low Energy Antiproton Ring (LEAR) at CERN for a range of isotopes. In this method the antiprotons were impinged on a nuclear target. Antiprotons approaching the nuclei in the target can be absorbed by the nuclear surface (the mean free path of antiprotons in nuclear matter is much shorter than the typical nuclear size). Around 25 isotopes with mass numbers in the range of $40 - 238$ were studied. Antiprotons were chosen as a probe for the experiment as the anihilation of a proton or a neutron in the surface of the nucleus would lead to different final nuclear states, which could be identified using chemical or spectroscopic means. The resulting final state would be a nucleus in which the proton or neutron number is lowered by one unit compared to the initial state. If both products are radioactive then nuclear spectroscopy can be employed to determine their relative yields, which are directly related to the proton and neutron densities at the annihilation site. The experimental results are presented in (Fig. 2.11); analysis of the data suggested that neutrons are distributed in a form of a halo rather than a skin [61]. However, as the antiprotons are absorbed only in the tails of the wavefunction of the nucleus the systematics of such measurements are debated, and large extrapolations are required to infer information about the nucleon radial distributions in the nuclear interior.

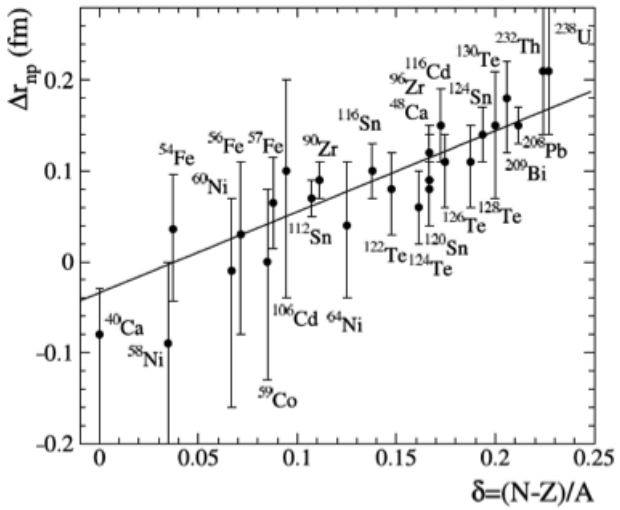

Figure 2.11: Difference between the r.m.s. radii of the neutron and proton distributions (Δr_{np}) are plotted against the symmetry parameter δ. Diagram taken from the reference [61].

Isospin diffusion in heavy-ion collisions gave Δr_{np}=0.22±0.04 fm for ^{208}Pb [62]. In this method the fragments resulting from a heavy ion colission are studied. The surface properties of the nuclei, including the neutron skin size, are predicted to influence which species are formed. From a detailed study of the reaction processes a model dependent determination of the neutron skin properties can be extracted.

There have also been a number of recent attempts to infer the existence of the neutron skin from model dependent studies of the global vibrational properties of nuclei [63, 64]. The Pygmy dipole resonance has been proposed as a state in which the neutron skin vibrates against the nuclear core. The properties of this resonance, such as its energy and width, are proposed to be sensitive to the properties of the neutron skin. Also the more conventional dipole vibrational mode of nuclei has been predicted to show sensitivity to skin properties in the measured electric dipole moment. Measurements of pygmy dipole resonances and electric dipole polarizabilities of nuclei gave Δr_{np} ranging from 0.156 fm to 0.194 fm with quoted accuracies as small as ±0.024 fm [65, 66, 67]. However, the model dependence is still debated [68] and an accuracy of ±0.05 fm in the measurement of the neutron skin of ^{208}Pb is taken from [7].

The measurement of parity violation asymmetries in electron scattering provides an independent probe of neutron densities because the weak charge of the neutron is much larger than that of a proton. The asymmetry is measured by the small (part per million) asymmetry between the number of electrons scattered at a given angle when their initial spin is aligned with the direction of motion compared to when it is anti-aligned. The interpretation of such results is less model-dependent and avoids the uncertainties of strong interactions. The disadvantage is that very long beam times are required to get the statistical accuracy for a given experiment because the asymmetries can only be measured at a single value of momentum transfer, fixed by the location of the electron spectrometer. Polarized electrons have been used as a probe of neutron distribution in only one very recent experiment, the ^{208}Pb Radius Experiment (PREX) at Jefferson Lab in the USA [69]. The first measurement of the parity-violating asymmetry, A_{PV} in the elastic scattering of polarized electrons from ^{208}Pb gave a thickness for the neutron skin of $\Delta R = 0.33^{+0.16}_{-0.18}$ fm, providing the first electroweak observation of a neutron skin [69]. The statistical errors are large but it is planned to reduce these with future measurements. Measurements of a lighter calcium target are also proposed. Those measurements will be an important addition to this experiment, however, the long beam times required to obtain statisticaly valid set of data mean that an extensive experimental investigation appears to be unfeasible at the moment.

The most recently established technique for studying neutron skins is that of coherent pion photoproduction. This method has the advantage over strongly interacting probes in that the initial state interactions of the photon are much weaker. The large mean free path of the photons in the nucleus offers the ability to probe the entire nuclear volume, whereas strongly interacting probes predominantly sample only the nuclear surface. Coherent pion photoproduction also contains different and potentially smaller systematics than the strong probes. A recent work carried out by the Crystal Ball at MAMI collaboration [3] extracted a neutron skin for ^{208}Pb of $0.15 \pm 0.03(stat)^{+0.01}_{-0.03}(sys)$ fm and could also gain sensitivity to the diffuseness of the neutron distribution. Based on the DKT model the results indicated that the diffuseness of the neutron distribution was larger than that of the protons, providing the first experimental confirmation for this effect which is predicted by most nuclear theories. The current work extends this

neutron skin measurement programme at MAMI to a different nucleus and also to a measurement across an isotopic chain, which has the potential to minimise theoretical model dependenceies and better assess the extracted infomation.

As can be seen from the above description, most work has focussed on ^{208}Pb due to its doubly magic nature and the large neutron-proton asymmetry. Previous measurements on tin isotopes are more sparse. Previous obtained results are discussed below.

A recent study employed the method of polarized proton elastic scattering at a 295 MeV incident beam energy [70]. Information about the neutron skin was extracted from measurements on two sets of five, isotopically enriched tin targets (^{116}Sn, ^{118}Sn, ^{120}Sn, ^{122}Sn and ^{124}Sn). Two thicknesses of targets were employed, the thinner ones providing accurate data for the forward scattered region while the thicker ones were employed to increase the statistics for the lower yield for more backward scatter angles. The proton scatter distributions obtained were analysed using a model of proton-nucleus elastic scattering based on a relativistic impulse approximation and using the relativistic Love-Franey interaction [71, 72]. Figure 2.12 shows the results of the experiment. In the plot on the left, the solid lines correspond to the RMF calculations using the parameters from [72] and the relativistic mean field densities from [73]. Even though those calculations appear to be in fair agreement with the experimental data, they overestimate the values of the cross sections for higher scattering angles (Figure 2.12). Based on the earlier ^{208}Pb results [74], and the analysis of the proton elastic scattering of ^{58}Ni, Terashima *et. al.* [70] modified the RMF calculations by fine tuning the effective nucleon-nucleon interaction to extract neutron density distributions from the experimental data. The results are compared with theoretical predictions in Fig. 2.12 and tabulated in Table 2.1.

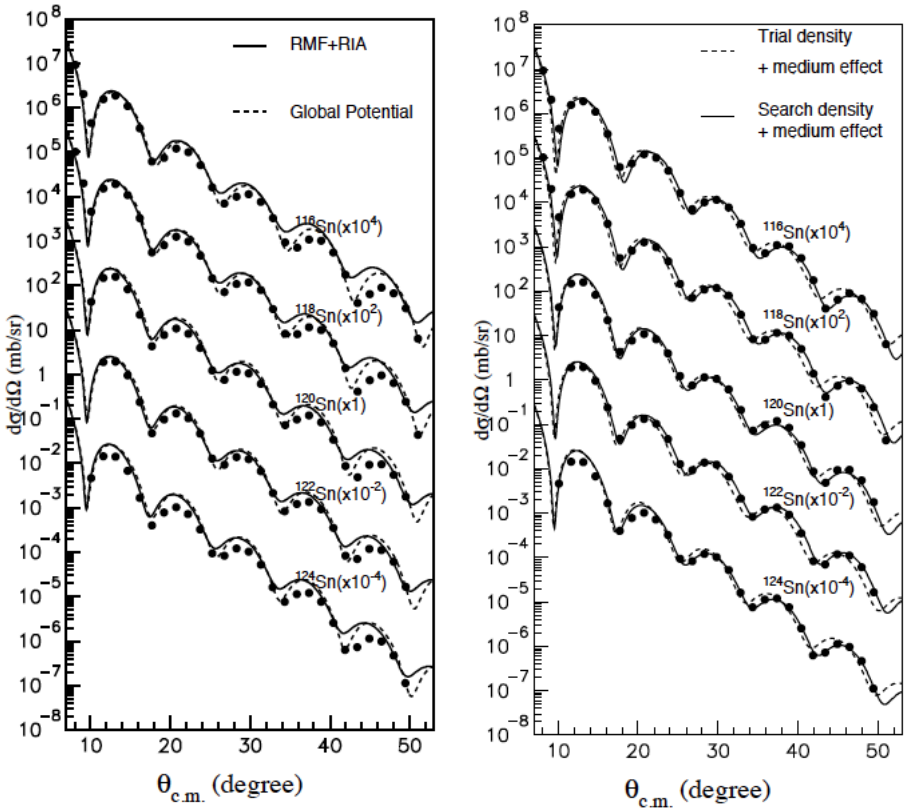

Figure 2.12: The plot on the left shows the differential cross sections for proton elastic scattering on tin isotopes. The sold lines correspond to the RIA calculations and the dashed lines show the calculations using global potential [75, 76]. The plot on the right shows the differential cross sections of tin isotopes with the solid lines corresponding to theoretical predictions from nuclear models. These are based on both Skyrme-Hartree-Foch approaches and relativistic mean field models. The figure is taken from the reference [70].

The values extracted for the neutron skin indicate an increase in the skin thickness with mass number across the isotopic chain.

Other approaches have looked at the giant dipole response of certain tin isotopes. The resonances were excited by elastic alpha particle scattering and by the (^{3}He,t) transfer reaction. Theoretically, it has been shown, that the cross section of the GDR excitation depends on the neutron skin thickness [77, 78, 79]. Krasznahorkay *et. al.* [64] confirmed it experimentally in the measurement of the GDR excitation cross section in inelastic α scattering. The data have been

Table 2.1: Neutron skin thickness of tin isotopes measured in the proton elastic scattering experiment.

Isotope	Neutron skin, Δr, (fm)
^{116}Sn	0.110±0.018
^{118}Sn	0.145±0.016
^{120}Sn	0.147±0.033
^{122}Sn	0.146±0.016
^{124}Sn	0.185±0.017

collected for two tin isotopes (^{116}Sn and ^{124}Sn) and ^{208}Pb and the relative neutron skin thickness have been extracted [66]. These results are also shown in the figure, but tend to have large errors not allowing for definitive conclusions to be drawn. The results do however support the existence of a skin of order 0.1 fm for the tin isotopes.

Figure 2.13 summarises the results from various experiments of neutron skin measurements on tin. These are compared with the theoretical predictions from various nuclear models.

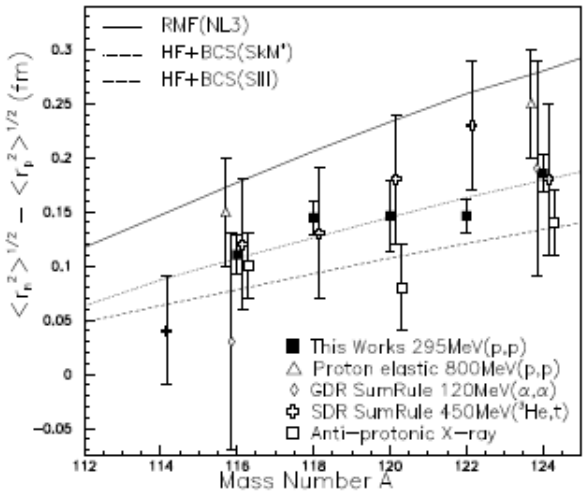

Figure 2.13: Values of the netron skin thickness for various tin isotopes predicted by different models. The solid squares show the results of the proton elastic scattering experiment at 295 MeV [70], the empty triangles correspond to the proton elastic scattering at 800 MeV [80] and the empty squares show the results of the antiprotonic X-ray experiment [81]. The results of the spin dipole resonance measurements [63] are indicated with the empty crosses and the data from the giant dipole resonance experiemnt [64] is marked with empty rhombes. The solid line shows the predictions of the RMF theory using the NL3 parameter set [82], dashed lines represent different Skyrme-Hartree-Fock calculations [83, 84].

To summarize, the proton and mass radii are among the most fundamental properties of atomic nuclei. However, currently a measurement of a matter radius has not been accurately determined neither from the experimental data nor the theoretical models. A number of various methods have been employed to determine matter radius of heavy nuclei, particularly ^{208}Pb. Such measurement has important consequences for a wide range of physics fields: theoretical studies of nuclear structure, atomic parity violation, heavy ion collisions and the physics of neutron stars. A measurement along an isotopic chain of tin allows the study of the evolution of neutron skin with increasing mass number in a setup that allows various systematic effects to cancel out. This should result in a much more accurate determination of the value of the neutron skin.

Chapter 3

Experimental Details

3.1 Overview

The experiment described in this dissertation was performed in the A2 hall of the MAMI facility at the Johannes Gutenberg Universitaet in Mainz, Germany in October 2012 over the course of 21 days.

The key element of the MAMI installation is the Mainzer Mikrotron which provides a 100% duty factor electron beam that can be directed at any of four experimental halls. The photon beam utilized in the experiment is produced by directing an electron beam onto a thin metallic radiator creating bremsstrahlung radiation. Then, one of the elements of the A2 hall detector setup, the Glasgow Photon tagging spectrometer [85, 86] analyses the recoiling electrons from the bremsstrahlung process and provides information about the energy of the photons. The tagger comprises of a large dipole magnet with a highly segmented detector apparatus near its focal plane. The tin target, located in the center of the Crystal Ball (CB), is exposed to these bremsstrahlung photons. The products of the resulting photoreactions is then detected by A2 segmented detectors. Since neutral pions have a very short lifetime, of the order of $\sim 10^{-18}$ s, it is not possible to detect them directly. Instead, the products of their dominant decay, two photons, are detected by the apparatus and the pion's 4 momentum is reconstructed from this information. A schematic picture of the MAMI facility is presented in Figure 3.1.

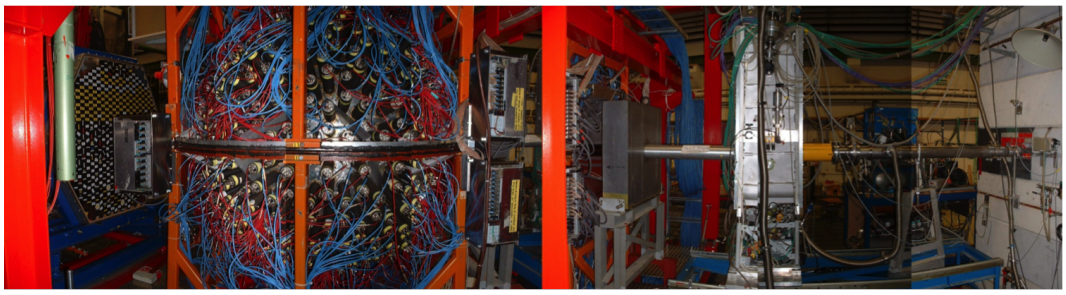

Figure 3.1: A picture of the experiential setup in the A2 hall at MAMI.

In addition to the CB and TAPS detectors, we also used information from the Edinburgh Particle Identification Detector (PID), which provides information about the charged particles detected by the CB and the Multi Wire Proportional Chambers (MWPC), which provides identification of charged particles and tracking information. The details of all the detectors as well as the MAMI facility itself are presented in the following sections.

3.2 Mainzer Mikrotron

The Mainz Microtron (MAMI) is a continuous wave electron accelerator. It is located at the Institut fuer Kernphysik at Johannes Gutenberg Universitaet in Mainz, Germany. MAMI has been in operation since 1979 and in that period has been upgraded three times, achieving successively higher electron beam energies and intensities. The most recent upgrade to MAMI-C, completed in 2006, provides an electron beam energy up to 1.6 GeV with an 80% helicity polarization and a beam current of over 20 μA (unpolarized electron beams can reach up to 100 μA).

The MAMI facility operates using a racetrack microtron design. In this design, a beam of electrons is accelerated by a series of radio frequency LINAC (linear accelerator) sections and recirculated through the LINACs using a magnetic field. Each time the beam passes through the LINAC, its orbit through the magnetic field changes, with higher energy electrons taking wider paths through the magnetic field. These paths are finely tuned so the electrons always pass through the LINAC in time with the correct radiofrequency (rf) electric field applied to the LINACs. The early stages of the MAMI racetrack microtron (RTM) employed

two homogeneous semicircular magnets and a small linear accelerator (LINAC) placed between them (see Fig. 3.2). Repeated passes through LINAC ensure that high beam energy can be achieved even if the acceleration with each pass is relatively small. The first microtron was constructed at the National Research Council of Canada in 1947 according to the design of V. I. Veksler where the electrons accelerated along circular paths, reached energies of up to 4.6 MeV [87]. Ever since this initial design the idea of a microtron has been worked on to reach higher electron energies. The concept of a RTM had already been proposed in 1945 but the first RTM was not constructed until 1961 and provided electron beams of energies up to $\sim$ 12 MeV.

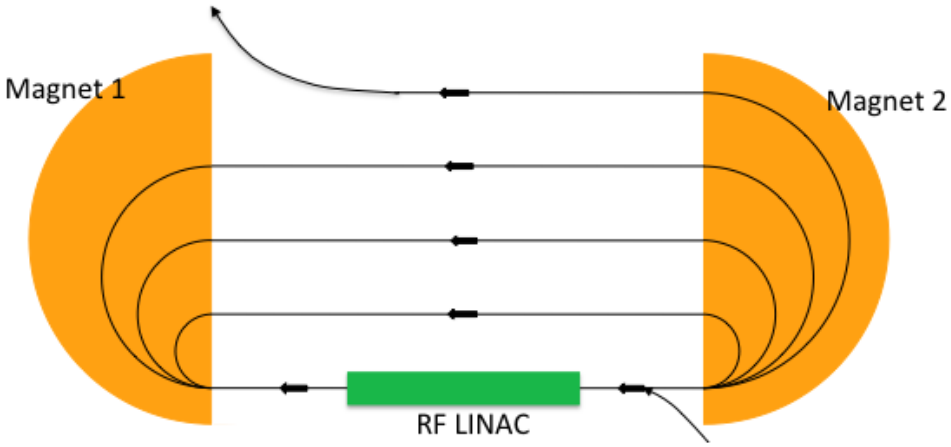

Figure 3.2: Schematics of a simple microtron.

In 1979 a RTM was first successfully used at the MAMI facility, producing an electron beam of 14 MeV (MAMI-A1). A subsequent upgrade (MAMI-A2) introduced another RTM to the design and allowed beam energies to go up to 180 MeV in 1983. The need for even higher beam energies inspired yet another upgrade (MAMI B), and in 1990 with the addition of another RTM it was possible to achieve energies of up to 855 MeV. However, quickly advancing research in the fields of nuclear and particle physics required even higher energies. A design allowing beam energies to go up to 1.5 GeV however, could not employ another RTM based on the dipole magnet design because the magnets required for achieving such energies would have weighted 2500 tons each which was neither financially nor spatially feasible. For comparison, magnets in the MAMI B design

weigh "only" 450 tons. The issue has been bypassed by adding a harmonic double-sided microtron (HDSM). In this design, rather than using two magnets to bend the beam by 180°, four 90° magnets and two accelerating sections have been used instead (Fig. 3.3).

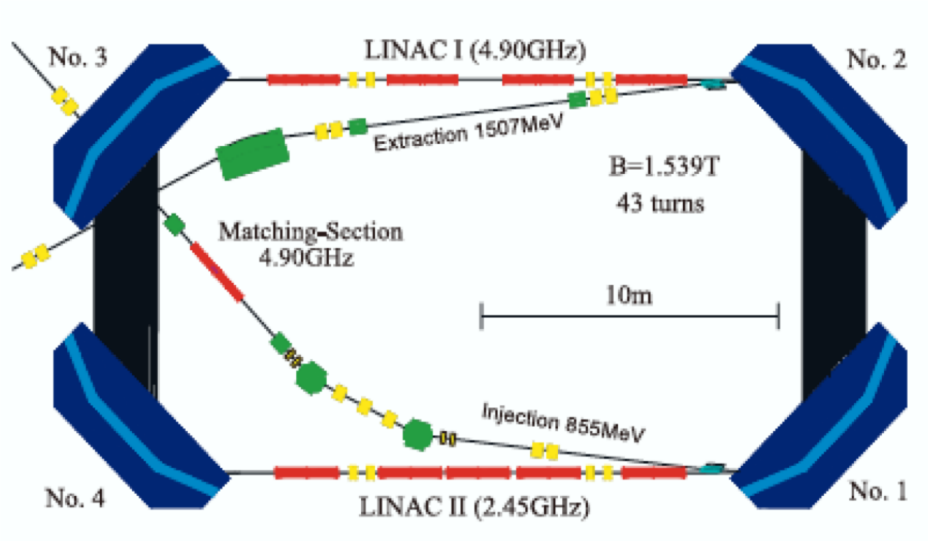

Figure 3.3: Schematic picture of a harmonic double-sided microtron for MAMI-C.

This design allowed a 1.508 GeV electron beam to be produced in December 2006, and energy as high as 1.604 GeV has been reached in 2009 [88].

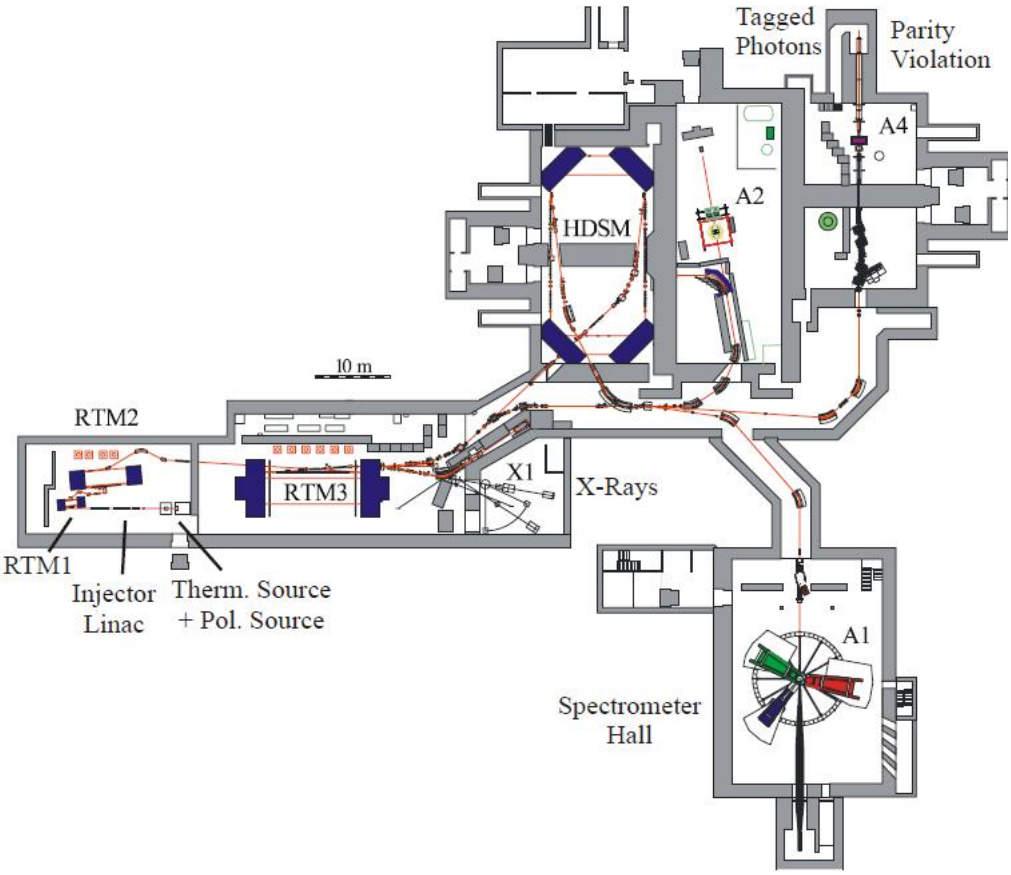

Figure 3.4: Floor plan of the MAMI facility.

3.3 The Glasgow Photon Tagger

The experiment was performed in the A2 hall of MAMI (Figure 3.4), which houses the installation dedicated to the studies of reactions between high-energy photons with different atomic nuclei. The photon beam used in this experiment was produced by electrons ejected from RTM3 which were then directed into a thin, 10 μm thick, copper radiator. The 855 MeV electrons interact with the electrostatic field of the copper nuclei and radiate photons. The energy, E_γ, of these bremsstrahlung photons can be calculated from:

$$E_\gamma = E_0 - E_e \tag{3.1}$$

where E_0 is the initial beam energy and E_e is the energy of the scattered electrons. This equation neglects the energy loss due to the recoil of the copper nuclei, however, the mass of the copper nucleus is high enough to assume that only negligible amount of kinetic energy are transferred.

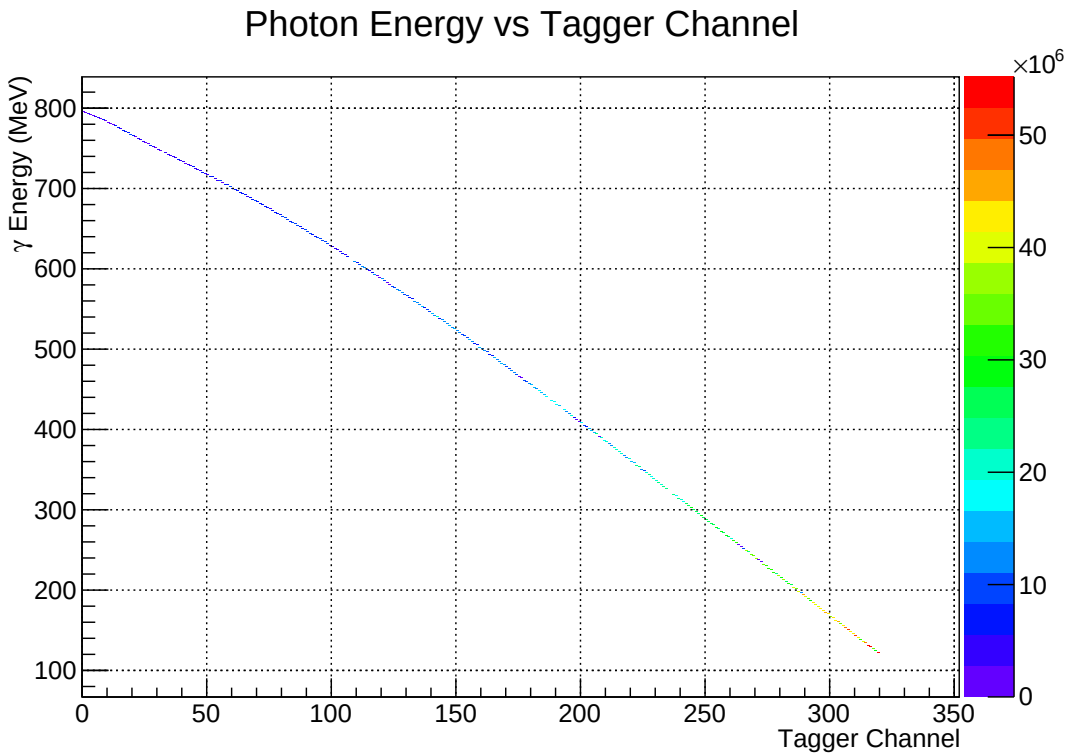

Figure 3.5: Plot of the photon beam energy against the tagger channel number. Lower energy electrons, which give higher energy photons, are bent more in the magnetic field and hit the lower channels in the tagger, the opposite applies to the higher energy electrons.

The Glasgow Photon Tagger (GPT) is a large momentum acceptance spectrometer. Electrons, after passing through the radiator, first enter the magnetic field of a quadrupole magnet, which focuses them vertically. After this, the resulting electrons pass through a dipole magnet which disperses them horizontally according to their energies. For example, the lower energy electrons associated with the production of higher energy photons are bent more significantly by the field compared to the higher energy electrons (Figure 3.5). The momentum of the bremsstrahlung electrons is analyzed in the Glasgow

Photon Tagger (Figure 3.6). By identifying the path of the electron in the field and correlating the timing of the electron with the subsequent photonuclear reaction in the target, the photons can be characterized on an event-by-event basis. This is referred to as a tagged photon beam. Electrons that have radiated bremsstrahlung photons are directed on to a segmented focal plane detector. The electrons that have not radiated any photons follow a curved path into a beam dump.

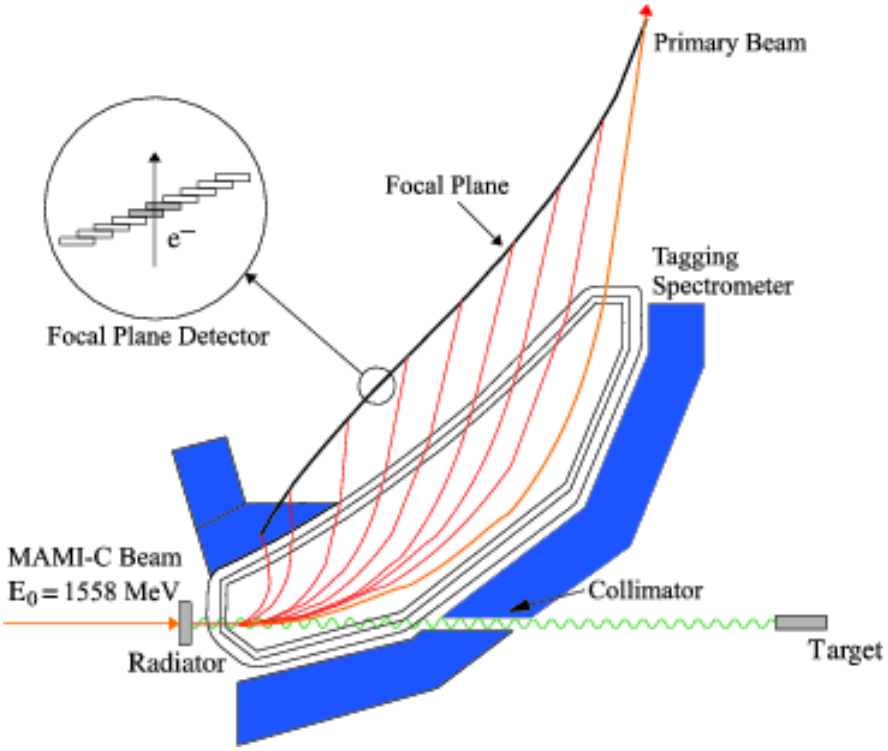

Figure 3.6: Schematic picture of the Glasgow Photon Tagger [89].

The Focal Plane (FP) detector consists of 353 plastic scintillator detectors wrapped in double-sided, aluminized Mylar [86]. Each of these scintillators is 80 mm long and 2 mm thick with a varying width of 9-32 mm. The detector width decreases along the focal plane in order to keep the energy resolution constant. The scintillators overlap by more than a half-width (Figure 3.6) which allows for electron detection by coincident signals in two adjacent detectors. The size of this overlap fixes the achievable energy resolution, which ranges from 2-8 MeV with an average of 4 MeV, depending on the beam energy [90]. The coincidence

condition also allows for significant reduction of the low energy background in the detector.

Each scintillator is connected to an R1635 Hamamatsu photomultiplier tube (PMT), which are shielded from the magnetic field by 0.7 mm thick steel plates and an individual sheath of μ-metal. The high segmentation of the array allows for the tagging of high-flux photon beams. When used with the 1.508 GeV electron beam, the tagger can operate at a rate of up to 10^8 s^{-1} flux photons in the energy range of 0.08-1.401 GeV. The maximum rate is determined by the operating limit of the individual PMTs which is 1 MHz per channel, a limit used in order to avoid an unnecessary reduction of their operating lifetime. The bremsstrahlung photons pass through the magnetic field of the GPT unaffected and exit into the experimental hall through a channel bored into the dipole magnet.

In order to ensure a small size for the beam spot on the target a 3 mm collimator is employed near to the exit of this bored channel. Employing a collimator not only produces a better defined beam spot on the target, but also reduces the photon flux. Without collimation, the photon flux incident on the target would be related more directly to the number of hits in the FP detector. To determine the exact luminosity of the photon beam, tagging efficiency measurements have to be made where a 100% efficient lead glass detector is placed in the beamline. This efficiency correction is applied individually to each detector channel in the focal-plane detector, as the efficiency depends on the opening angle of the gamma beam, which depends on the gamma (or electron) energy. The tagging efficiency is defined as:

$$\epsilon_{tagg} = \frac{N_\gamma}{N_e} \tag{3.2}$$

where N_γ is the number of photons passing through the collimator and is registered by the lead glass detector, and N_e is the number of hits in the FP detector. During the tagging efficiency measurement, carried out as separate runs in the experiment, a lead glass detector is placed in the path of the collimated beam. The beam intensity employed in this measurement is lower than that used in the actual experiment in order to protect the lead glass detector from the potential radiation damage and to reduce the number of multiple hits in the FP detector.

3.4 The Crystal Ball

The Crystal Ball (CB) detector was constructed and used in various experiments long before being installed at MAMI. First used in the 1970s for colliding beam experiments at the SLAC facility to obtain the first accurate measurements of J/ψ meson [91]. Later it was used at DESY and in the Brookhaven National Laboratory and arrived in its current home, the A2 hall at MAMI only in 2002. The CB is a highly segmented calorimeter, it consists of 672 sodium iodide (NaI) crystals, each in the shape of a truncated triangular pyramid, and arranged into the shape of a 20 sided polyhedron (Fig. 3.7).

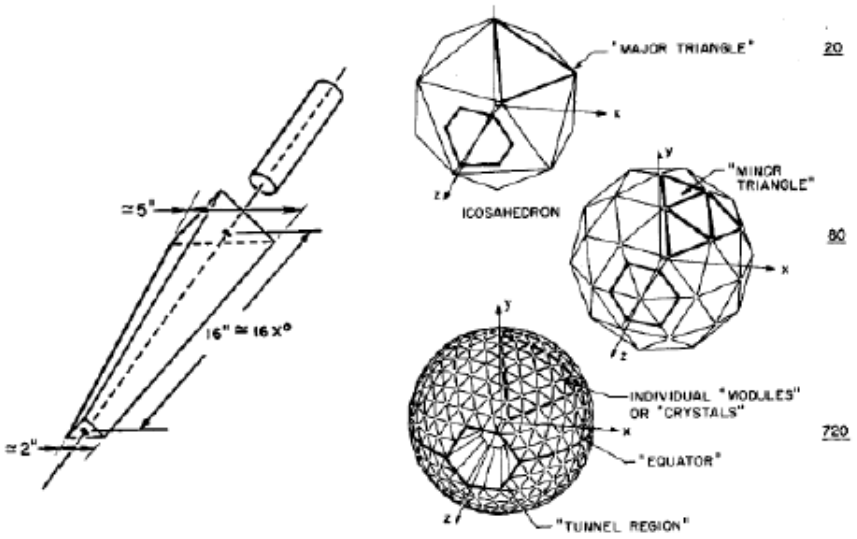

Figure 3.7: NaI crystal and CB geometry [88].

Having been originally designed for colliding beam experiments, the design of the detector had to accommodate the beamline running across and through the center of the CB. Because of that the section corresponding to 24 crystals on opposite poles of the sphere had to be cleared, making room for the beamline components. The remaining crystals were grouped into two, hermetically sealed hemispheres; the isolation of the crystals from the outside environment was essential because NaI is a highly hygroscopic and it degenerates when exposed to the moisture in the air.

The outer and inner radii of the CB are 66 cm and 25.3 cm respectively. The two hemispheres are enclosed within a 1.5 mm thick steel casing and the width of the gap between them, in the equator region, is 8 mm thick, consisting of two 1.6 mm thick steel plates with an adjustable air gap, usually set to 5 mm. Such a design allows for the coverage close to complete angular range, $\sim 94\%$ of 4π.

The crystal are arranged into groups of major and minor triangles. Each major triangle consists of 36 crystals. These can be divided into 4 smaller triangles (minor triangle) which in turn are divided into 9 segments corresponding to the individual NaI crystals (Fig. 3.7). Each crystal is 40.6 cm long with the sides of the inner and outer faces being 5.1 cm and 12.7 cm respectively, and is optically shielded with a reflector paper and aluminized Mylar. This in turn is connected to the 5.1 cm diameter SRC L50 B01 PMT, chosen for its good linear response over a wide range of energies. These photomultipliers are mounted outside the CB and any scintillation light produced, is fed into them through a 5 cm air gap and a thick glass window, separating the NaI crystals from the photomultipliers (PMTs). This set up constitutes part of the hermetic design helping to maintain an isolated environment for the sodium iodide crystals. During the experiment, photons produced by the reactions inside the CB trigger an electromagnetic shower which deposits energy in the NaI crystals. This system allows for a good resolution across a wide range of energies. The amount of deposited energy and the number of crystals hit depend on the reaction studied. The information about the nature of the particles detected in the CB are recovered from the analysis of the hits in the NaI clusters. The basic detection properties of the CB are summarized in the table 3.1 [92].

3.5 Multi Wire Proportional Chambers

Inside the tunnel region of the Crystal Ball two Multi Wire Proportional Chambers (MWPCs) can be found. The task of this apparatus is to provide track information of the charged particles produced in the reaction. It follows the same design as that originally used in the DAPHNE detector [93].

Each of the two MWPCs is built up of three layers; internal and external stripes acting as cathodes and a middle layer of wires as the anode (Fig. 3.8). The cylindrical cathodes are made of 1 mm thick rohacell laminated with aluminum

Table 3.1: Crystal Ball Detection Parameters

Energy Photon Resolution		
	$\frac{\sigma}{E}$	$\sim \frac{1.7\%}{E}(GeV)^{0.4}$
Angular Resolution		
	azimuthal:	$\sim \frac{2^\circ}{sin\theta}$
	polar:	$\sim 2-3^\circ$
Angular Coverage		
	azimuthal:	0 - 360°
	polar:	20 - 160°
Time resolution		
		$\sigma \sim 2$ ns

stripes, 4mm wide and 0.1 μm thick, spaced 0.5 mm apart. The stripes are wound helically at 45° with respect to the anode wires, in opposite directions. The anode is made up of 20μm Tungsten wires 2 mm apart placed parallel to the beam direction. The chambers are filled with a gas mixture of argon (74.5%), ethane (25%) and freon (0.5%).

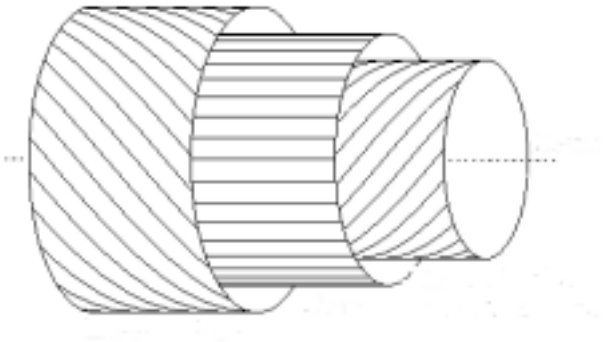

Figure 3.8: Diagram of the MWPC showing the positions of the oblique anode wires and the horizontal cathode wires [94].

Correlating the hits in both the cathode stripes and the anode wires will determine the tracks for charged particles. For the current experiment, the

MWPCs were only used to accurately locate the position of the target with respect to the CB detector. This information is extracted from the measurement of reactions which produce two charged particles in their final state. A linear fit to the polar angle and z-position of the hits registered in both chambers is used to obtain the azimuthal and theta angles for each track. The trajectories of multiple tracks are then analyzed to find their intersection, and thus we obtain the position of the target. The design of the chambers provides a full 360° coverage of the azimuthal angle with a polar coverage that ranges between 21° and 159°; the characteristics of the MWPC chambers are summarized in table 3.2.

Table 3.2: MWPC parameters

Angular Resolution		
	azimuthal:	$\sim 1.8°$
	polar:	2°
Angular Coverage		
	azimuthal:	0 - 360°
	polar:	21 - 159°

3.6 Particle Identification Detector

The Edinburgh Particle Identification Detector (PID) is located inside the Crystal Ball and is surrounded by the MWPCs. It is a $\frac{dE}{dx}$ detector and, together with the CB apparatus, provides information about the charged particles. The PID consists of 24 EJ204 plastic scintillators arranged in a cylindrical shape. Each scintillator strip is 500 mm long and 4 mm thick, and, in order to minimize the gaps between adjacent scintillators, the design demanded that they should have a right-angle trapezium cross-section. Each strip is wrapped in an aluminized Mylar foil in order to optically isolate the scintillation light. The scintillators are connected to different PhotoMultipliers (PMT), Hamamatsu R1635 and E1761-04 via perspex light guides. An aluminum ring with 24 holes supports the construction where the PMTs are positioned in order to match the arrangement of the scintillator strips (Fig. 3.9). The entire detector is wrapped in a black

Tedlar (polyvinyl fluoride) foil to ensure the lightproof of the detector.

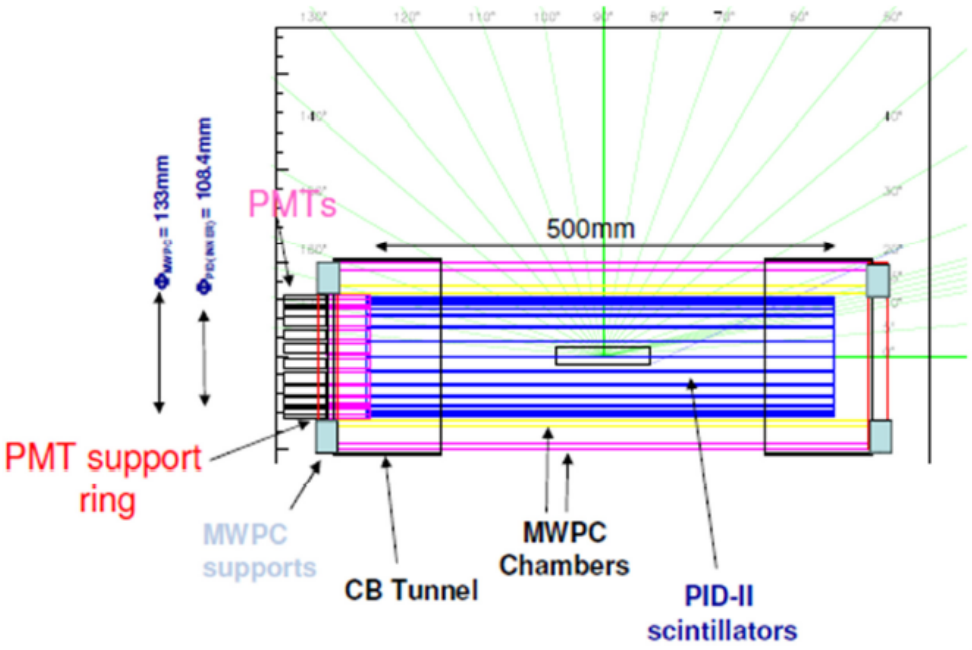

Figure 3.9: The Edinburgh Particle Identification Detector (PID) schematics.

The design of the PID allows for full coverage of the azimuthal angle and for a coverage from 20° to 160° of the polar angle. This coverage matches the angular acceptance of the CB exactly. When a charged particle passes through the scintillator it deposits a fraction of its energy while the rest of its energy will be detected in the Crystal Ball. The identity of such particle is determined by correlating the events from both detectors while enforcing the hit in the CB to be within 15° from the center of the PID scintillator (azimuthal angle). When plotting the energy deposited in the PID against the energy registered in the CB on a two-dimensional plot a characteristic shape is obtained (Fig. 3.10). The proton and pion distribution are easily identifiable in such a plot, and can be used to separate the particle species. For the current method separation of charged particles is not necessary as the final state of interest consists only of neutral photons. However, the PID can be used to identify the uncharged events of interest from the data.

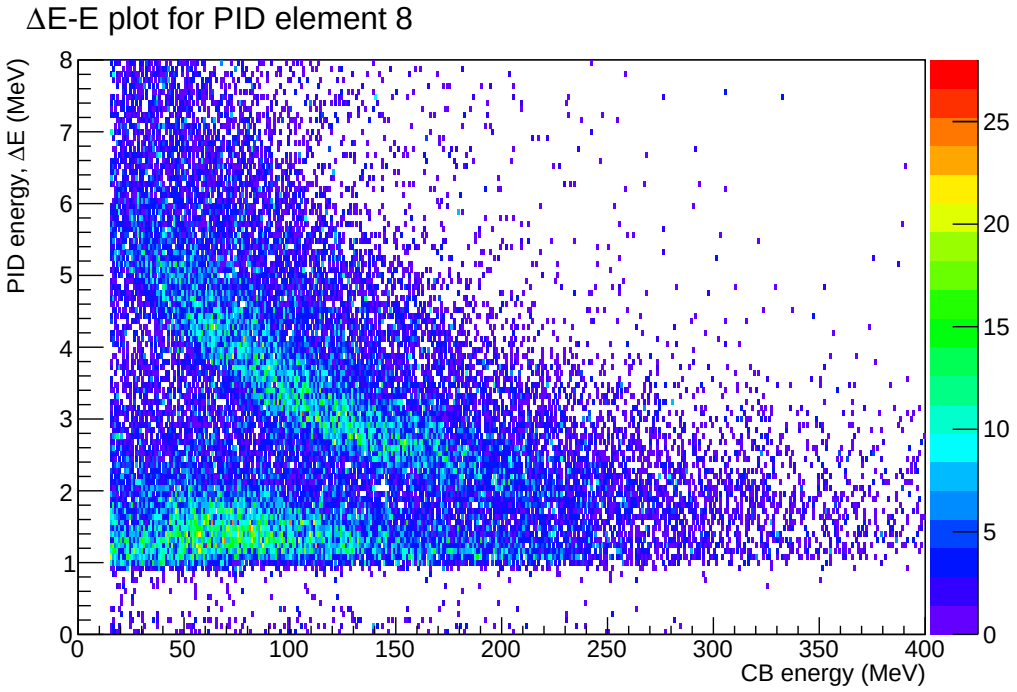

Figure 3.10: ΔE-E plots of PID and CB energy deposits.

3.7 TAPS

The Crystal Ball detector has been designed for colliding beam experiments. For this reason, the detector does not cover $\sim 20°$ in the polar angle range for both the backward and the forward direction. In order to fill this gap, another detector had to be added to the system: the TAPS detector. In MAMI, the CB is used for fixed target experiments. These experiments have reaction products that are Lorentz boosted forward, due to the forward motion of the photon-target centre-of-mass frame of reference. For this reason it is crucial for many experiments to have the additional TAPS detector, covering those missing forward 20 degrees, mounted [95].

TAPS is located 1.5 m downstream from the reaction vertex. It is a segmented calorimeter detector made from 385 hexagonal BaF_2 crystals (Fig. 3.11). Each crystal is 25 cm long, wrapped in 8 layers of 38 μ thick UV-reflecting PTFE (Teflon) foil and a single layer of 15 μm thick aluminum foil in order to assure light proofing. The cylindrical end part of each crystal is connected to an Hamamatsu

R2059 PMT using silicone glue.

The barium fluoride crystals, even though they have a much lower scintillation output than the NaI crystals used in CB, have a higher density (4.89 g/cm^3 for BaF_2 against 3.67 g/cm^3 for NaI) and larger atomic number. These characteristics provide just as good detection efficiency as the sodium iodide crystals used in the CB. Another key property of the BaF2 crystals over other inorganic materials is their fast timing resolution ($\sim$ 0.6 ns), which makes the detector ideal for identifying particles through time of flight (TOF) methods [95].

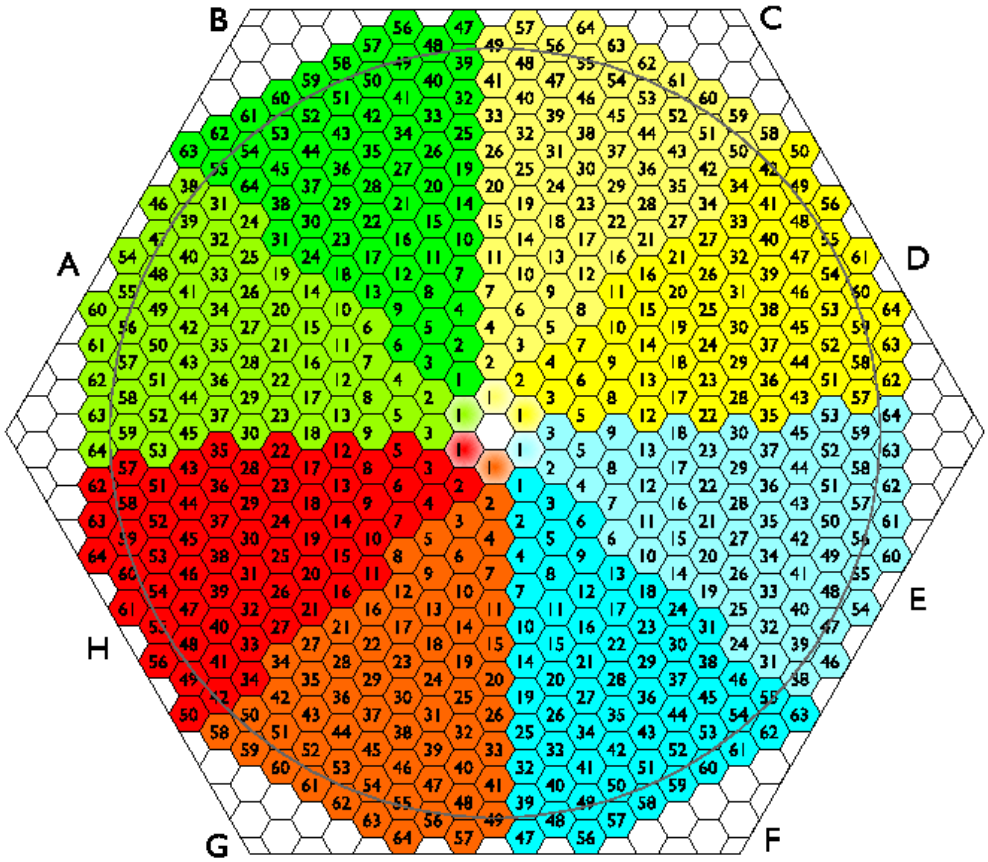

Figure 3.11: Diagram of the BaF_2 crystals arrangement in TAPS. Different colours represent sectors that can be used in the trigger if required.

Directly in front of the TAPS detector, there is an array of 5 mm thick NE102A plastic scintillators which constitute the TAPS Veto detector. The output from this detector is collected by optic fibers in Valvo XP2972 phototubes. This addition to TAPS allows the discrimination between neutral and charged particles by correlating events from TAPS Veto and TAPS. This allows charged particles to be identified as a function of their energy and energy deposition.

As mentioned before, a parallel method used by TAPS to identify particles is

through the time of flight of the particles. By measuring the time for a particle to travel from the target to the TAPS detector one can discriminate between higher mass particles (like protons and neutrons) and particles traveling at, or almost at, the speed of light like photons and electrons.

A different method for particle identification is the pulse shape analysis. This exploits the fact that BaF_2 crystals have fast ($\sim$ 0.6 ns) and slow ($\sim$ 620 ns) decaying components. Each particle type leaves its own particular imprint on slow and fast components and by comparing the ratios of energy deposited in both, it is possible to improve the particle identification process.

For the current work the data from TAPS was not included. This was due to the complications in the yield extraction due to the variation in the energy resolution for the reconstructed π^0 mesons when the TAPS information was included (the TAPS detectors have a better angular resolution than the CB as they are somewhat smaller and located further from the target). The analysis of the TAPS data would be a worthwhile additional analysis in the future, but was not possible in the timescale of the current analysis. However, its omission does not significantly affect the yield of events or the results presented in this thesis.

3.8 Targets

The targets used in this experiment were three isotopes of tin (^{116}Sn, ^{120}Sn and ^{124}Sn); chosen because of their stability, and because these elements are easily availabile in an enriched form. Theoretical calculations predict a change of $\sim$ 0.05 to 0.15 fm in the neutron skin thickness when going across the isotopic chain of tin from ^{116}Sn to ^{124}Sn (Fig. 2.1) [96].

The targets were secured in a foam target holder and placed inside a carbon fibre tube at the center of the detectors using a calibrated mounting rod. The details of the targets are given in table 3.3.

Targets used in this experiment had different thickness because they were obtained from two different sources. The ^{116}Sn and ^{124}Sn targets were manufactured at GSI specifically for this experiment and the ^{120}Sn target was a previously used Primex target.

Table 3.3: Tin targets. ^{116}Sn and ^{124}Sn targets' parameters were measured in Mainz and ^{120}Sn data comes from [97]

Isotope	mass (MeV)	thickness (mm)	density (g/cm^2)	surface density ($nuclei/cm^2$)	enrichment (%)
^{116}Sn	107961.738	2.332 ± 0.021	7.084 ± 0.140	8.584×10^{21}	99.53
^{120}Sn	111688.180	0.586 ± 0.001	7.294 ± 0.347	2.201×10^{21}	98.29
^{124}Sn	115417.416	2.176 ± 0.030	7.431 ± 0.155	7.860×10^{21}	99.90

3.9 Data Acquisition

The analogue output signal of the detectors' PMTs were read out and translated into a digital signal by the data acquisition system (DAQ) with the use of charge to digital converters (QDCs), amplitude to digital converters (ADCs) and time to digital converters (TDCs). The latter measures the time difference between the start signal of the experimental trigger and the stop signal from a given detector element. Providing information about the time of the event. The ADCs give digital information proportional to the pulse height of the signal, while QDCs return digital signal proportional to charge. Both these values, pulse height and charge are proportional to the energy deposited in the detector element.

The signals from the QDCs, ADCs and TDCs were read out by the AcquDAQ software package [98]. Then, in the AcquRoot analysis the signals from the converters were translated into physical quantities (energy and time measurements). The calibration procedure that allowed for this conversion is presented in chapter 4.

The detailed description of the detectors' electronic systems is explained in the sections that follow.

3.9.1 Tagger Electronics

The energy of the bremsstrahlung photons was obtained from the hit position of the recoiling electron on the tagger focal plane. The timing of this was used to match the events in the detectors with the hits on the focal plane. Providing that a signal from the focal plane passed the threshold of the discriminator, a logic pulse was fed to a Compass Accumulation, Transfer and Control Hardware

(CATCH) TDC (section 3.9.2) to record the time of the hit. Simultaneously, a signal from the discriminator was sent to FASTBUS scalers, which provided the count rate for each FP detector element. The count rate in the tagger focal plane was also recorded by ungated, free running scalars, that were subsequently used to determine the photon flux independently of the experimrental trigger.

3.9.2 Crystal Ball Electronics

As depicted in Fig. 3.12, signals from each PMT were sent to fan-out units splitting the analogue output into three signals. One passes to a Flash ADC (F-ADC) via a delay, the second goes through the discriminator and branches to a scalar and CATCH TDS, and the third signal is fed to the triggering electronics.

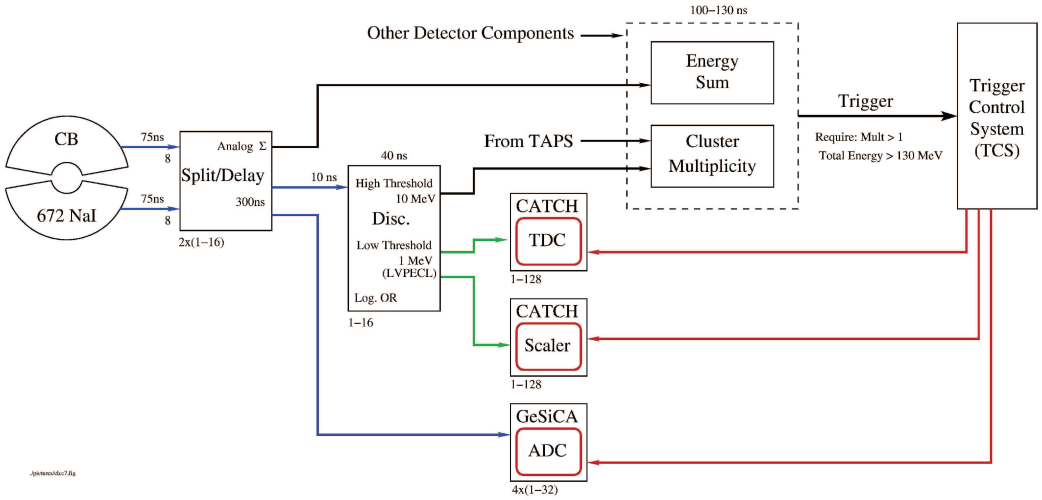

Figure 3.12: Crystal Ball electronics [99].

The integral of the pulse from each PMT was obtained from the F-ADCs, which sampled the shape of the signal with a frequency of 40 MHz. Since the

DAQ was not prepared to handle such large volumes of data, only the integrals of pulses over three regions were taken. The integration was done over a time window of 750 ns (30 signals). The first window was set to sample the pedestal whose signal is a convolution of remnant light and residual charge in the PMTs. The second window was set over the signal, and the third was set to evaluate the tail of the pulse. This set up allowed for the simultaneous measurement of the signal and the pedestal for every event, and with the dynamic subtraction of the pedestal from the signal, the energy resolution of the crystals was significantly improved.

Contrary to the typical TDCs, which are started by a hit in a relevant detector and stopped by a logic pulse from the trigger, CATCH TDCs, developed for the Compass experiment at CERN, allow for multiple hits in TDCs [100]. Using a $\sim$ 10 GHz oscillator each TDC is running independently while the CERN-standard trigger control system synchronizes the signals in those TDCs. One of the TDCs is designated as a reference element and attached to the trigger. When an event passes the trigger threshold a logic pulse is sent to this reference TDC and the oscillator value is stored. When other TDCs record a hit, the corresponding oscillator value is stored in a buffer. In order to extract the information about the timing of an event the oscillator value stored in the reference TDC has to be subtracted from the oscillator values recorded by other TDCs, the conversion rate of 117 ps/channel is then used [101].

3.9.3 TAPS Electronics

The signals from the TAPS PMTs received a similar treatment to those from the Crystal Ball and were also split into three separate signals. One signal was directed to a TDC via a constant fraction discriminator (CFD), which analyzed the shape of the pulse and provided accurate timing information for the QDCs. The other two signals were fed to separate QDCs, one with integration time of 40 ps, the other with 200 ps, this double integration allows for a pulse shape analysis.

3.9.4 Triggering Electronics

While an event is being registered by the DAQ, no other event is recorded; this is defined as dead time. In order to reduce the effects of this dead time, a series of triggers were set up to limit the events read by a DAQ only to those relevant to the experiment. Two LeCroy LRS 4805 logic units were used to define the conditions an event must satisfy in order to be recorded.

The first level trigger for this experiment required the sum of energy deposited in all 672 NaI crystals of the CB to be greater than 40 MeV. For the second level trigger, the DAQ analyses grouped NaI crystal in clusters of 16, and it was required that two hit clusters were detected in the Crystal Ball. When those two conditions were satisfied the DAQ read the event, recorded it in the data stream and reset the electronics ready for the next event. The applied triggers did not cause any significant rate reduction for the used photon energies (only a couple of precent [2]), it was the deadtime of the detection systems that affects the yield of the studied reactions. In MAMI the typical livetimes are of the order of $\sim 75\%$.

3.10 Analysis Code

Online analysis and monitoring of the data was done using the AcquRoot framework [98]. AcquRoot was written in C++ specifically for the data analysis at MAMI, it uses libraries and tools of R00T [102, 103]. AcquRoot consists of three components: the AcquDAQ Data Acquisition, the AcquRoot Analysis and the AcquMC Event Generator.

Offline analysis was done using the a2GoAT framework (A2 Generation of Analysis Trees) [98]. In this framework AcquRoot is used to produce the analysis trees containing only the basic track information for the particles such as 4-vectors and the particle ID. This removes the need to analyse all the data from the basic ADC, TDC values every time the analysis is run and speeds up the computation time significantly. The GoAT software package [98] is then used in a subsequent step to process these event trees; here particle reconstruction, all the data checks, and calculation of relevant physics observables is performed.

3.11 Summary

To summarize, the experiment detailed in this thesis was performed in the October of 2012 in the A2 experimental hall of the MAMI facility at the Johannes Gutenberg Universitaet in Mainz, Germany. The 855 MeV electron beam provided by the Mainzer Microtron have been used to produce bremsstralung photons whose energies have been determined by the Focal Plane detector in the Glasgow Photon tagging spectrometer. Such tagged photon beam is then directed on a target, which is located in the centre of the Crystal Ball detector. The products of the reactions of the target with photons are detected by the CB and TAPS detectors. PID and MWPCs provide information about charged particles.The signals from these detectors are read out by the AcquDAQ software package. Online analysis and monitoring is done with the use of the AcquRoot and offline analysis is performed using the a2GoAT frameworks. The following chapter describes the techniques used in the calibrations of various detectors used in the experiment presented in this dissertation.

Chapter 4

Calibrations

This chapter addresses the calibrations of all the detectors used in this experiment. The process involved converting the raw signals from the detectors into real physical quantities allowing for the energy, position and timing corrections to be determined and applied to the subsequent analysis.

4.1 Tagger Calibrations

4.1.1 Energy Calibration

The tagger energy calibration determines the relationship between tagger channel number and the electron energy. The calibrations were carried out by colleagues at the University of Glasgow [90].

In order to make a tagger energy calibration, an incident MAMI electron beam of an energy of interest is bent in the magnetic field; for a 855 MeV beam, a field of ~ 1.025 T is used. Then the magnetic field was varied in small steps to guide the beam through the focal plane (FP) and an energy measurement was taken at each step. Six different electron beam energies were used for the calibration, which ranged from 195.22 MeV to 705.26 MeV, with an uncertainty of 0.16 MeV. The uncertainty in the magnetic field was 0.01 mT [104].

The varying magnetic field required the beam to sweep across a given channel allowing for the determination of the position of a hit in the FP detector with an accuracy of 0.05 of the channel width. Finally, in order to relate the FP channel number to the electron energy a linear interpolation between the different

energies was used. In the analysis software a hit in each tagger channel was assigned the electron energy from this calibration. As the incident MAMI electron beam energy is well determined, the energy of the any associated bremsstrahlung photons can be determined.

4.1.2 Tagger Random Subtraction

Some of the hits in the FP of the tagger do not correspond to bremsstrahlung photons subsequently produced in the reaction identified in the CB or TAPS detector apparatus. These uncorrelated FP hits contribute to the background radiation. They arise from a number of processes, for example: bremsstralung electrons that produced photons which pass the target without any interactions, Moeller scattering in the radiator (non-radiative reactions) and bremsstrahlung photons which were subsequently removed from the flux by the collimator. They are known as *random* hits, in contrast to the *prompt* hits, which correspond to the photons that triggered the photoreaction identified in the detector apparatus. In order to discern which tagger hits should be classified as prompt and which as random a timing analysis of the FP events is carried out.

The time recorded by the tagger TDCs for each element in the focal plane is a measure of the time difference (time taken by the photon to reach the target plus the time taken by the photon-induced reaction products to satisfy the experimental trigger) between the hit in the tagger FP detector element and the trigger (Fig. 4.1). The hits in the tagger that correspond to the photons triggering reactions in the target form a prompt peak in the tagger time spectra. The peak is a reflection of the fact that prompt hits will have a roughly constant time difference relation between the FP and the trigger. On the other hand, the electron hits which did not correspond to photons triggering the reactions within the target result in a flat background of random hits in the time spectra.

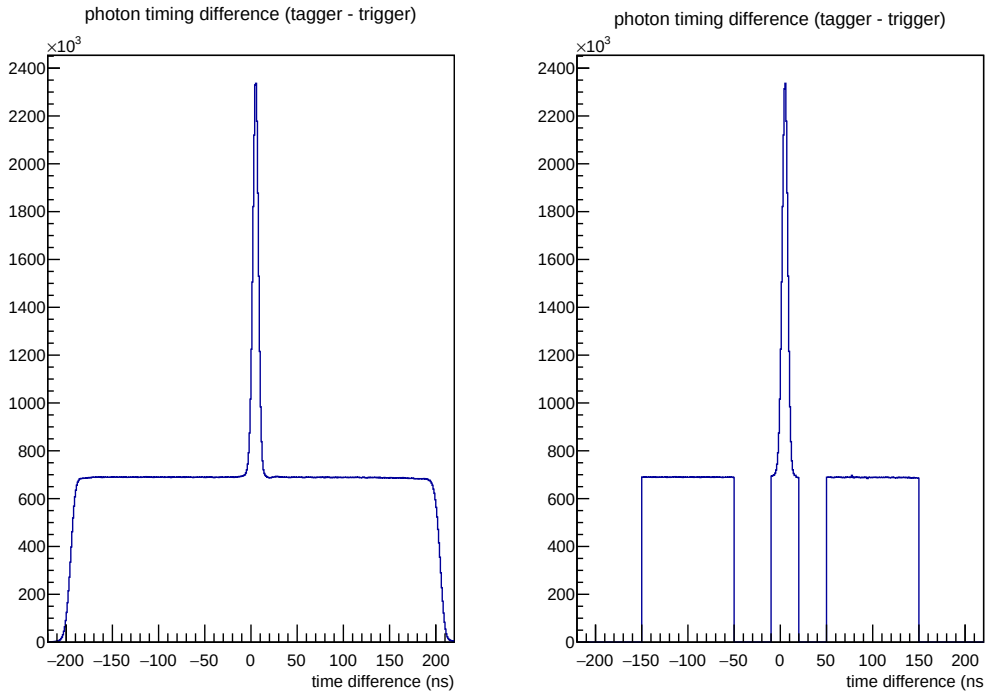

Figure 4.1: Time spectrum of the hits in the tagger. The plot on the left shows the full time spectrum and the plot on the right shows the cuts defined for the prompt and random regions.

Nevertheless, it is not possible to categorise hits as prompt or random for an individual event because there is still some random contribution even in the selected region of the prompt peak. In order to resolve this, a large number of random events are analysed in exactly the same way as the prompt events and then given an appropriate negative weight (to account for the different size of the prompt and random regions) when filling the physics histograms. This effectively removes the effect of random events in the prompt region.

Before the single uniform selection of prompt and random regions can be carried out the timing of the individual tagger FP elements must be aligned to account for any small variations. This was done by fitting a Gaussian function to the prompt peak of each individual FP element and introducing an offset in the timing such that the prompt peaks from all the elements were synchronized to the same time.

4.2 Crystal Ball Calibrations

4.2.1 Clustering Algorithm

Photons entering the Crystal Ball deposit their energy in the NaI crystals via electromagnetic showers which hit multiple crystals in each event. These groups of impacted crystals are called clusters. The accurate analysis of the CB events required an algorithm which identifies the clusters and recovers information about the incident photon's energy and position from the energy deposited on the crystals within a cluster.

The first step in the analysis is to identify the crystal with the highest energy deposit, the central crystal of the cluster, and its 12 closest neighbours (Fig.4.2). An impact on this central crystal provides the timing information for the event. The energies of the neighbouring crystals are scanned and if their energies are greater than the threshold energy of around 2 MeV they are added to the cluster. It has been confirmed that in 98% of cases the energy deposit of the shower triggers 13 crystals or less [2] and this is why only the 12 closest neighbors of the central crystal are considered in the algorithm. The total energy of the cluster is then obtained as:

$$E_{sum} = \sum_{k} E_i \tag{4.1}$$

where E_i is the energy of the i^{th} crystal in the cluster of k detector elements. The condition of the the total energy of the cluster being greater than 20 MeV is then applied to suppress any background effects.

The position of the hit is calculated as the weighed mean position given by the equation:

$$r_{mean} = \frac{\sum_k \sqrt{E_i} r_i}{\sum_k \sqrt{E_i}} \tag{4.2}$$

where E_i is the energy deposited in the i^{th} crystal and r_i is the position of the i^{th} crystal in the cluster.

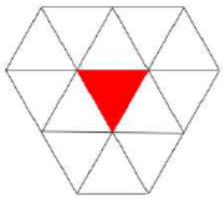

Figure 4.2: Schematic representation of a NaI cluster. The central triangle, shaded in red, depicts a triangular face of the NaI crystal and is the logical center of the cluster. The other 12 triangles are its closest neighbours.

4.2.2 Crystal Ball Energy Calibration

Crystal Ball energy calibrations have been carried out by the colleagues from UCLA and Johanes Gutenberg Universitaet in Mainz [105]. The energy calibration of the Crystal Ball was performed in three steps. first, a low energy calibration - mainly important for the acquisition system was obtained, then a high energy calibration has been performed, and in the end, an energy scale factor has been applied to account for crystal thresholds and clustering algorithms.

4.2.2.1 Low Energy Calibration

In this first step of the CB energy calibration, an ^{241}Am/^{9}Be source was placed at the center of the Crystal Ball [105]. The α decay of Americium, and a subsequent capture of these particles by Beryllium, triggers a series of reactions resulting in the excited state of ^{12}C which decays to a ground state and emits a 4.438 MeV photon in this process. This photon energy deposit in the NaI crystals has been used to adjust the gains of all PMTs, so that the detected peak was in the same position in the ADC spectra for all the detector elements.

4.2.2.2 High Energy Calibration

The photons produced in neutral meson decay, $\pi^0 \rightarrow 2\gamma$, have energies much higher than the photons used in the low energy calibration. Therefore, a calibration in the data analysis more appropriate for higher energy photons is also required. This is because the higher energy photons will create deeper showers in the CB and would be expected to have different sensitivities to any scintillation

light attenuation effects which depend on depth. The $\pi^0 \rightarrow \gamma\gamma$ reaction is used as a source of such photons for the calibration. The invariant mass, $M_{\gamma\gamma}$, of two photon events detected in the CB was reconstructed from the information about the measured energy and momentum of the photons (Fig.4.3). Events with $M_{\gamma\gamma}$ around the mass of the π^0 were selected for the analysis. The following selection cuts are also applied:

- no less than 70% of the detected photon energy had to be deposited in a single NaI crystal. This criterium was decided upon to ensure the deposit in a single crystal dominated the cluster;
- in order to ensure that the photons used for the calibration were of similar energy, the condition of having an energy difference between two photon clusters of less than 35% of the total energy was set up;
- the tagged photon energy had to be less than 180 MeV. This restriction constrained the energy range of the decay photons to be between 40 MeV and 125 MeV. Such an energy cut favored large opening angles between the photons, resulting in an even angular distributions in the lab frame.

The invariant mass of π^0 reconstructed from the two photon decay, was fitted with a Gaussian function to determine its centroid. The mean of the fit, corresponding to $M_{\gamma\gamma}$, has been compared to the mass of π^0. With this information a new gain factor, G_{new}, was obtained according to the equation below:

$$G_{new} = \frac{M_{\gamma\gamma}}{M_{\pi^0}} G_{old} \Big[\frac{MeV}{channel} \Big] \tag{4.3}$$

where G_{old} is the gain factor used previously. Because the energy of the photon cluster detected depended on both the central crystal and all the other crystals in the cluster, a single set of calculation to obtain the new gain was not enough. Several iterations were required to iterate the gain of each crystal such that the $M_{\gamma\gamma}$ calculated from all the crystal combinations were aligned.

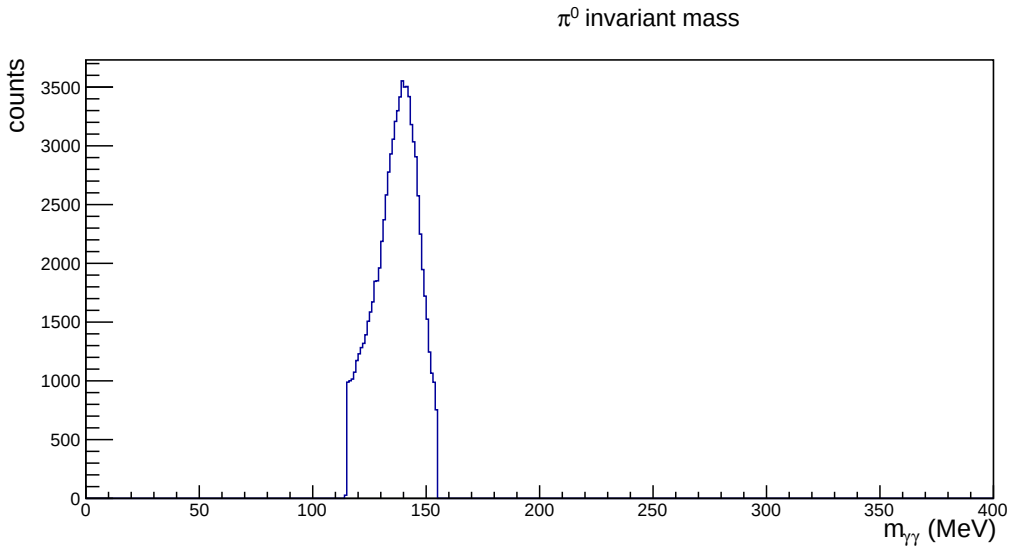

Figure 4.3: Reconstructed mass of the π^0.

4.2.2.3 The Energy Scaling Factor

The recorded energy of the incident photons is not necessarily the same as the total energy of the cluster and there is some energy dependence on this factor because of the energy losses due to the individual energy thresholds of the CB crystals in the showers. To account for this in the analysis, another energy correction had to be applied. In order to ensure that the mass reconstructed from the decay of two photons was indeed the mass of π^0 meson, an additional scaling factor of 1.05 was applied to the data. This is consistent with the values employed in previous analyses [2, 106].

4.2.2.4 Time Walk Correction

There arises a time difference between the small and large signals registering at the discriminator threshold because of the slow time response, 250 ns, of the NaI crystals [107]. Therefore, in order to account for this time difference, the times reported by the TDCs required a correction which improved the CB time resolution (Figure 4.4). The corrected time, T_{corr}, is defined as:

$$T_{corr} = T - r\sqrt{\frac{a_0}{a}} \tag{4.4}$$

where T is the measured time, a_0 is the discriminator's voltage, r is the rise in the time and a is the signal's amplitude.

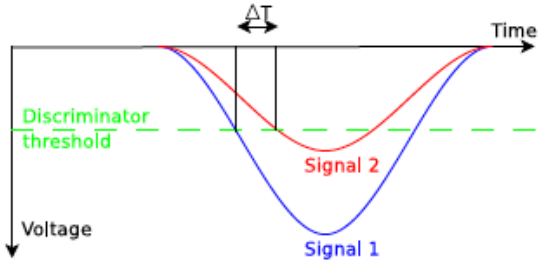

Figure 4.4: CB time walk.

4.3 The PID Calibration

4.3.1 PID Azimuthal Corrections

In order to accurately determine the correlation between hits in the PID and Crystal Ball, the PID azimuthal angle (ϕ) with respect to the Crystal Ball had to be measured. The steps taken to calculate the value of ϕ are as follows.

First, only the events that triggered a signal in one of the crystals in a CB cluster were selected. The reason for doing this was to keep events with a well defined angle and to enhance the contribution of charged particles to the yield (elecromagnetic showers from photon events only rarely fire a single crystal). Another cut made to the event sample was to only retain events in which a single PID element fired. In this way combinatoric backgrounds from multi-body final states were not allowed to complicate the subsequent analysis.

The angular distribution of those events has been plotted for each PID element, which gave a single peak over the azimuthal range of each one (Figure 4.5). A 1D projection has been plotted for each PID element and a Gaussian function was fitted to the peak. Having 24 PID elements means that each of them occupies $\sim 15^\circ$ of the total azimuthal coverage. A linear fit was used, and the gradient measured allowed accurate calibration of the azimuthal angle corresponding to the centre of each element (Figure 4.6).

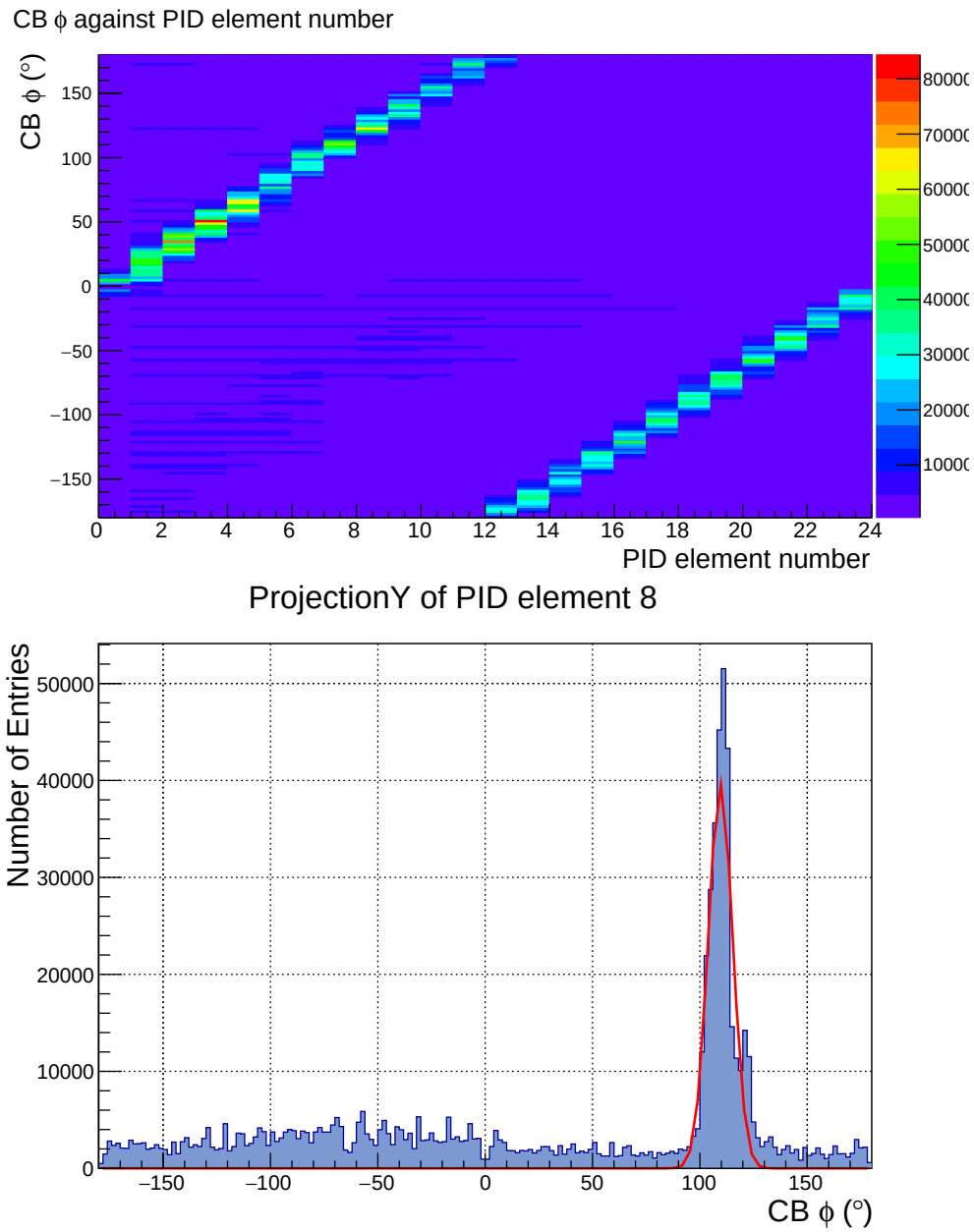

Figure 4.5: Plot of ϕ position in CB cluster vs hit in PID (top) and Gaussian fit to the projection of PID element 8 over the azimuthal range (bottom).

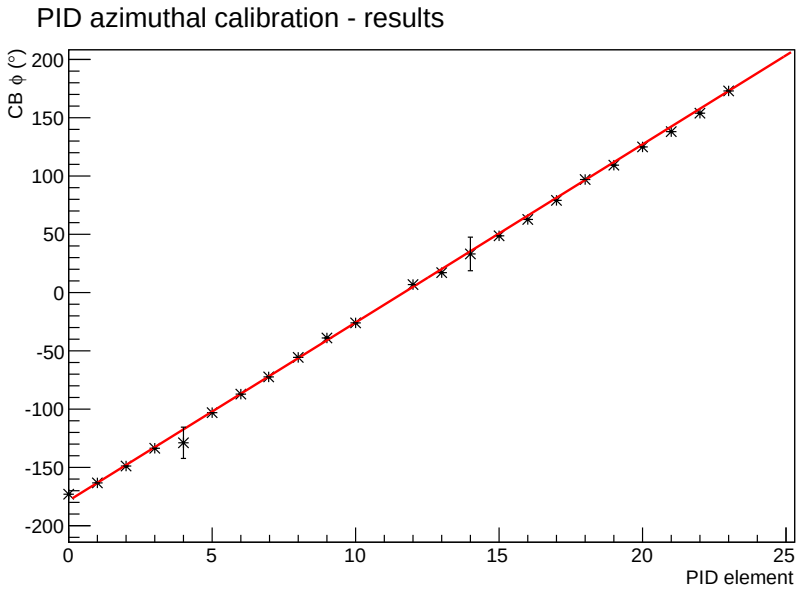

Figure 4.6: PID azimuthal correction - linear fit to the means of the Gaussian fits to the ϕ distribution of each PID element against the element number.

4.3.2 PID Energy Correction

The energy calibration for each PID element used the (ΔE-E) relation described earlier (Section 3.6). Different charged particle species such as protons, pions and electrons formed separate loci on these plots. By comparing these loci in experimental data and simulated data, using the GEANT4 package, an absolute calibration of the PID ADC signal to PID energy can be obtained on an element by element basis. This procedure is described below.

The ΔE-E plots were divided into bins according to the energy deposited in the CB. A binning of the CB energy of width 10 MeV was used in the analysis. The PID energy corresponding to each bin was extracted (Figure 4.7). Those projections featured two domininant peaks, the first one corresponding to the pion and the second one representing proton ridges. Although other charged particles can be produced in photoreactions, such as deuterons, their yield is much smaller and does not complicate the analysis. The proton peak was fitted with a Gaussian function and the value of the mean extracted (Figure 4.8). This step has been performed for all the energy bins in the range of 20-300 MeV. Similarly,

the GEANT4 simulated data had the same procedure applied. Subsequently, the means of the Gaussian functions for the experimental data have been plotted against corresponding means for the simulated data. A linear fit has been used to determine the gain for each PID element (Figure 4.8).

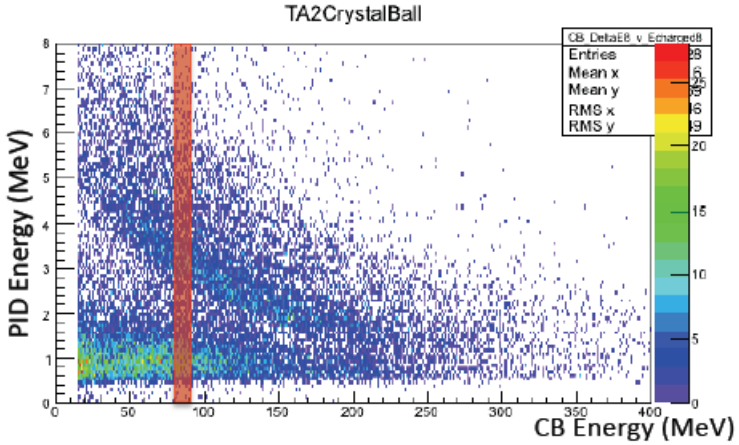

Figure 4.7: ΔE-E plots of PID vs CB energy deposits. As an example, a 10 MeV energy bin is shaded in red.

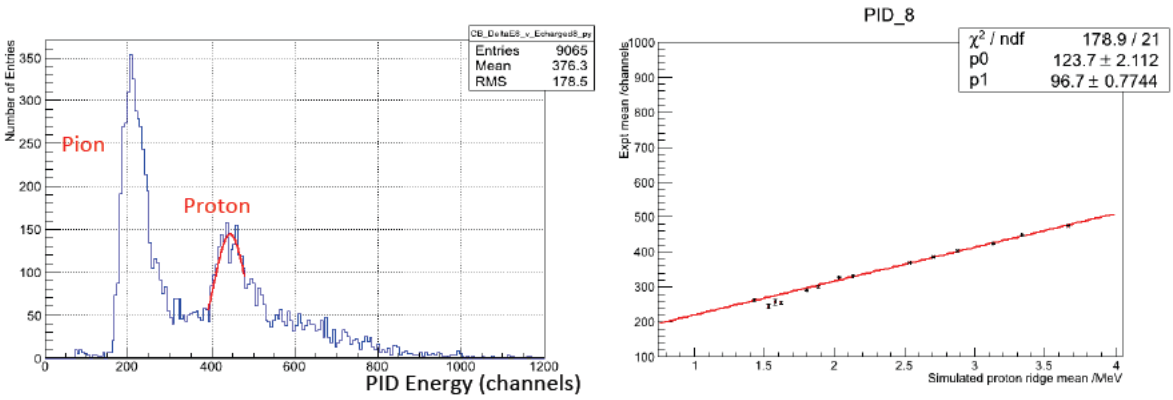

Figure 4.8: Gaussian function fitted to the proton peak (left) and linear fit to the Gaussian means (right).

The PID ADC measures the charge of the input signal. However, the device always has a residual offset or pedestal, due to the current required to run the module. This pedestal offset for the calibration was obtained from the analysis of

the raw ADC signal for each PID element. The first peak in the ADC spectrum represents the pedestal position. A Gaussian function has been fitted to this peak and the value of the mean was determined. This offest is applied to the data used in the calibration described above.

4.3.3 PID Time Calibration

Accurate information about the timing of the events, obtained with the TDCs, is an essential part of the data analysis. Timing the coincidence allows for a correlation of the coincidence charged particles between different detectors to be made. It is then used in the clustering algorithm of the Crystal Ball, and enables particle identification in TAPS to be performed, therefore allowing for the association of a hit in the FPD with an event in the CB/TAPS detectors. The principles followed for the time calibration of the various detectors are the same, therefore, only the PID time calibrations are described in more detail below.

The TDC spectrum of each PID element was fitted with a Gaussian and a value of the means for all the elements have been extracted (Figure 4.9). These values have been used to determine the offset in the calibration and align the peaks of all the detector elements in the timing spectrum (Figure 4.10). The misalignment for the PID element 16 is caused by the malfunctioning PID element (Figure 4.11).

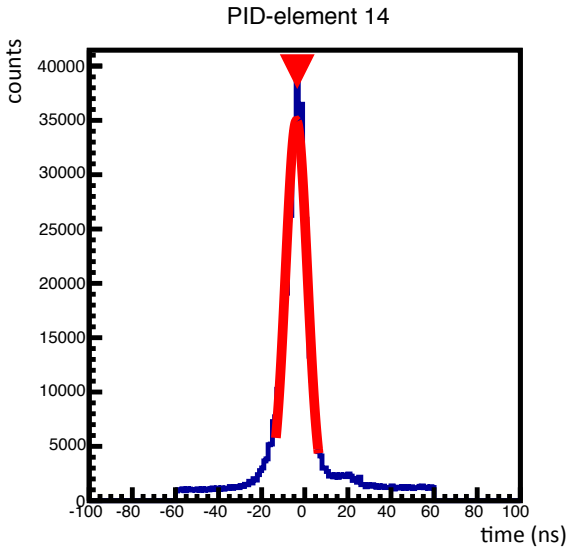

Figure 4.9: Gaussian fit to PID-element 14. The red arrow marks the mean of the peak.

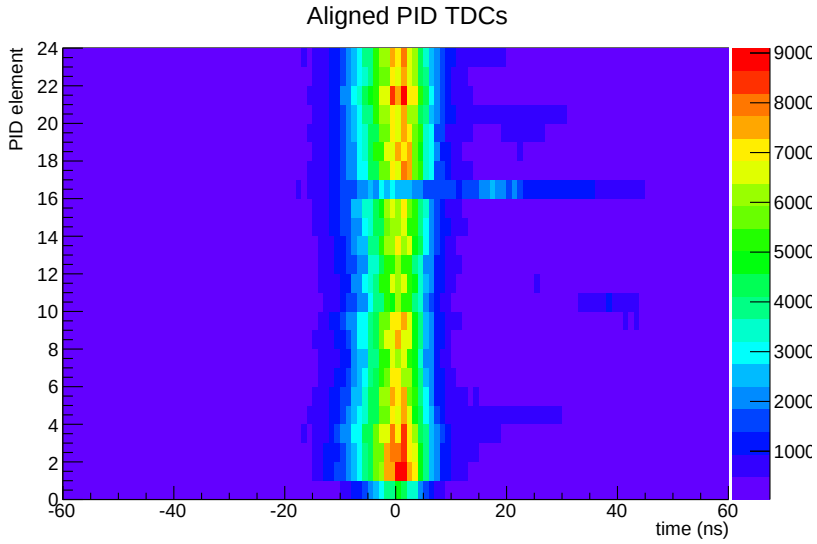

Figure 4.10: Time alignment of all PID elements.

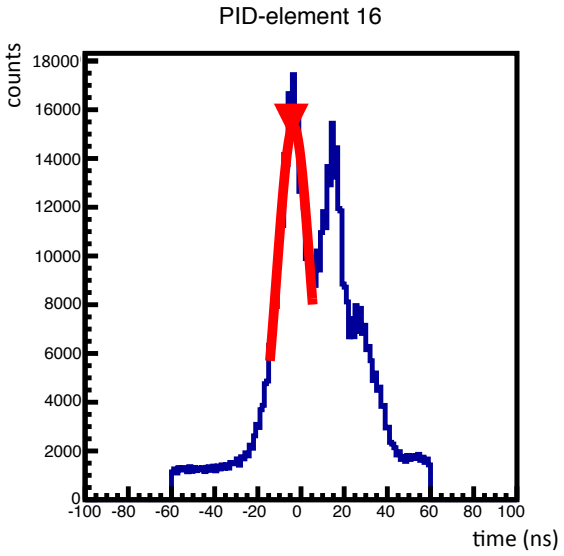

Figure 4.11: Gaussian fit to PID-element 16. The TDC spectrum of the malfunctioning PID element where the red arrow marks the mean of the peak.

As the reaction of interest for this thesis does not require charged particle separation, the PID is only used to identify clusters in the CB which are not associated with a PID hit. This was done using only the TDC information.

4.4 TAPS Calibration

The calibration of the TAPS BaF_2 crystals employed cosmic rays using the mean deposited energy of the minimum ionizing muons equal to 37.7 MeV [108]. For each of the BaF_2 crystals' PMTs the position of the energy peak was adjusted so it was in the same ADC position for all the detector elements, and then the channel number corresponding to the mean peak position was determined.

Using a similar technique to that employed in the CB calibrations, the correction for the gain was obtained. However, because the detection of two photons from the π^0 in the TAPS is very rare, the events having only one photon detected in the TAPS and one in the CB were chosen. A detailed procedure for

this calibration can be found in [109].

The procedure to calibrate the plastic Veto detectors in front of each TAPS crystal was similar to the one used to calibrate PID. The pedestal positions were obtained from the raw ADC spectra and the gain was determined by comparing the experimental mean position of the proton peak in the Veto to the simulated data. Details of this method can be found in the reference [110].

4.5 Summary

To summarize, this chapter outlined the procedures followed for the calibrations of the different detectors used in the MAMI A2 experimental hall. The calibration of this detector system consisting of the Tagger and FPD, the CB and the TAPS detectors have been shared between several members of the A2 collaboration. The details of the methods used at each stage of the calibrations have been described and those calibrations performed by the colleagues were explicitly referenced. The next chapter describes the data analysis, i.e. the process of converting the digital information from the calibrated detectors and translating it into physical quantities of interest.

Chapter 5

Data Analysis

This chapter describes the analyis carried out to take the calibrated detector data and produce the physics observables of interest.

5.1 Target Position Correction

The information from the charged track events in the MWPCs was used to accurately determine the positions of the targets. The reconstructed z-vertex position from multiple charged track events are presented in the figures below:

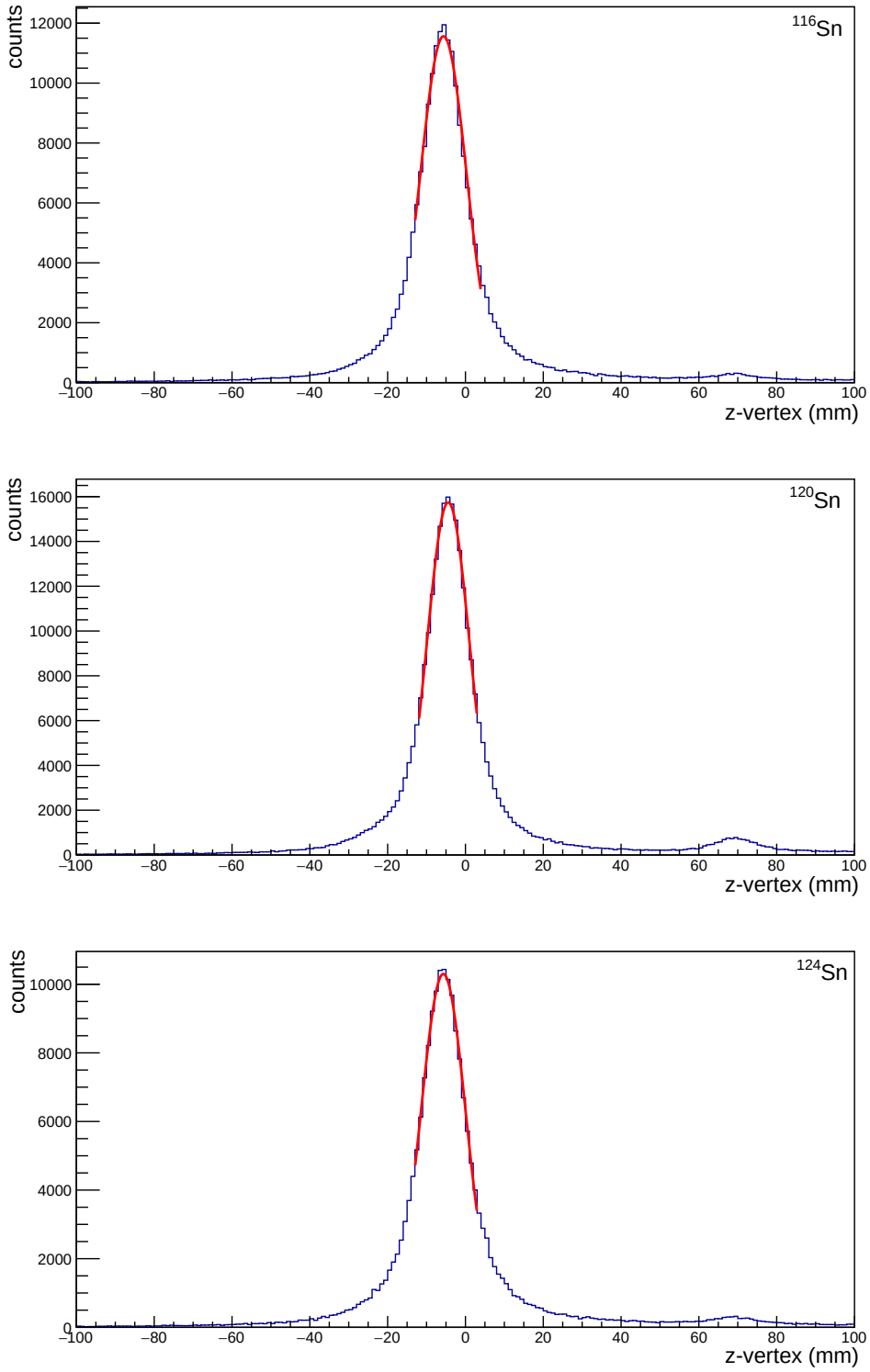

Figure 5.1: Target positioning. Top graph shows the fit results for ^{116}Sn, the middle graph shows data for ^{120}Sn, and the bottom graph shows ^{124}Sn.

The position of the target was determined by the use of a Gaussian fit to the charged particle reaction vertices (Fig.5.1). The mean of the Gaussian fit was extracted and its value employed in the analysis as the target position correction. The offset values were found to be -0.5631 ± 0.0023 cm for ^{116}Sn, -0.4435 ± 0.0015 cm for ^{120}Sn and -0.5686 ± 0.0021 cm for ^{124}Sn.

The value obtained for the position offset with respect to the Crystal Ball was used in the analysis code to correct the momenta of the particles detected. The formulas below show how the momentum is calculated for the target located at the centre of the Crystal Ball (Equation 5.1) and how the calculation is corrected when the effect of the position offset is included (Equation 5.2):

$$p = \frac{E_{meas}}{\sqrt{x^2 + y^2 + z^2}}(x, y, z) \tag{5.1}$$

$$p = \frac{E_{meas}}{\sqrt{x^2 + y^2 + (z - z_{corr})^2}}(x, y, z - z_{corr}) \tag{5.2}$$

where E_{meas} is the measured energy of the deposit in the cluster; x, y, and z are the coordinates of the centre of mass of the cluster and z_{corr} is the correction due to the target position offset determined with the MWPCs.

The correction of the target z-vertex position has a direct effect on the calculations of the reconstructed π^0 angle θ. Including the target position correction shifts the reaction vertex upstream and gives a more accurate calculation of the reconstructed pion angle. It should be noted that there is only a slow variation of the angle with target position. For a 1 cm offset (much larger than found here) the largest deviation in θ (which occurs at 90°) is 1.26°.The deviation at the edge of the Crystal Ball is only 0.44°. The value of the θ deviation at the edge of TAPS depends on whether a Cherenkov's detector is used or not. It varies between 0.10° and 0.14° depending on the actual TAPS detector position[111].

5.2 Coherent Events

As described in chapter 2, the π^0 photoproduction from nuclei can occur in several different ways, and alongside the coherent process, incoherent and quasi-free reactions take place. In order to extract the coherent events from the

background, a missing energy analysis has been performed. This technique uses information on the incident photon's energy from the tagger and the π^0 4-momentum reconstructed from the information recorded in the Crystal Ball.

The pion's missing energy is calculated using the following formula:

$$\Delta E_\pi = E_\pi^{CoM}(E_\gamma) - E_\pi^{CoM}(E_{\gamma_1\gamma_2}) \tag{5.3}$$

where $E_\pi^{CoM}(E_\gamma)$, defined in equation 5.4, is the pion energy in the pion-nucleus' centre of mass frame of reference. E_γ in the incident photon energy, s is the invariant mass of the photon-nucleus system and m_π and M^2 are the masses of pion and the nucleus, respectively. $E_\pi^{CoM}(E_{\gamma_1\gamma_2})$ is the pion's energy reconstructed from the detected energies of the two decay photos, Lorentz-transformed to the CoM reference frame.

$$E_\pi^{CoM}(E_\gamma) = \frac{s + m_\pi^2 - M^2}{2\sqrt{s}} \tag{5.4}$$

Although the pion energy can be approximated as the sum of the energies of the two decay photons, considering the angular information of the reaction allows for much better energy resolution, and therefore, more accurate calculations [112]:

$$E_\pi = \sqrt{\frac{2m_\pi^2}{(1 - \frac{E_1 - E_2}{E_1 + E_2}^2)(1 - cos\phi)}} \tag{5.5}$$

where E_1 and E_2 are the detected energies of the two decay photons and ϕ is the opening angle between them. The Lorentz transformation of the pion energy detected to the CoM frame of reference is calculated from:

$$E_\pi^{CoM} = \gamma\Big(E_\pi - \frac{E_\gamma}{E_\gamma + M}\big(E_1 cos\theta_1 + E_2 cos\theta_2\big)\Big) \tag{5.6}$$

where θ_1 and θ_2 are the polar angles of the two decay photons, E_π is the detected pion energy. The figure 5.2 illustrates this relationship.

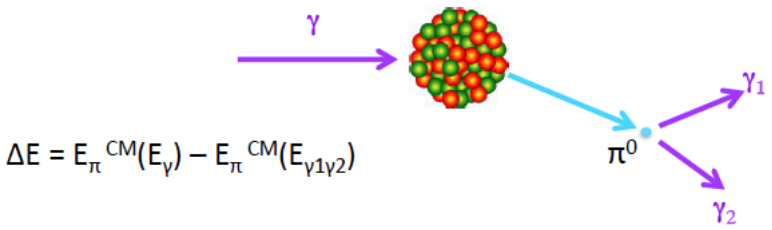

Figure 5.2: A diagram illustrating the coherent pion photoproduction. Note that the π^0 decay occurs at very short distances from the reaction vertex and is displaced in the above figure for clarity.

The condition for the coherent π^0 photoproduction process is satisfied when $E_\pi^{CoM}(E_\gamma)$ and $E_\pi^{CoM}(E_{\gamma_1\gamma_2})$ are the same. Background processes however, return negative values of ΔE_{pi} since the initial energy is split between other particles, in addition to the detected π^0. Energy can also be taken by the daughter nucleus, when it is left in an excited state.

In order to extract the coherent π^0 yield the missing energy spectrum has been split into several energy bins in the photon energy range from 135 to 580 MeV, and initially into 180 angular bins in the θ_π range between $0-180°$. The resulting spectra were then fitted with one or two functions describing the coherent and background signals.

The fitting procedure is tuned by considering the relative contributions of the different processes as a function of the pion angle. As shown in the figure 5.3 the coherent process shows a very strong variation, exhibiting a maximum cross section for the forward π^0 angles of around 20 degrees. For the incoherent processes, however, the cross section variation is much slower with angle [113]. This behaviour implies that, for the forward angle regions around the coherent π^0 maxima, the ΔE_π spectrum will be entirely dominated by the coherent peak [3]. This allows the coherent peak to be fitted in isolation and the parameters of the fitted gaussian to be fixed. This fit information can be subsequently used for the fits in the regions where incoherent contributions dominate and the coherent peak is less prominent due to a large background. GEANT4 simulations and studies of the CB experimental data confirmed that the missing energy resolution does not vary significantly with θ. This is due to the symmetric acceptance of the CB and the negligible variation in pion energy as a function of θ (for a given photon

energy) due to the heavy masses of the recoiling system.

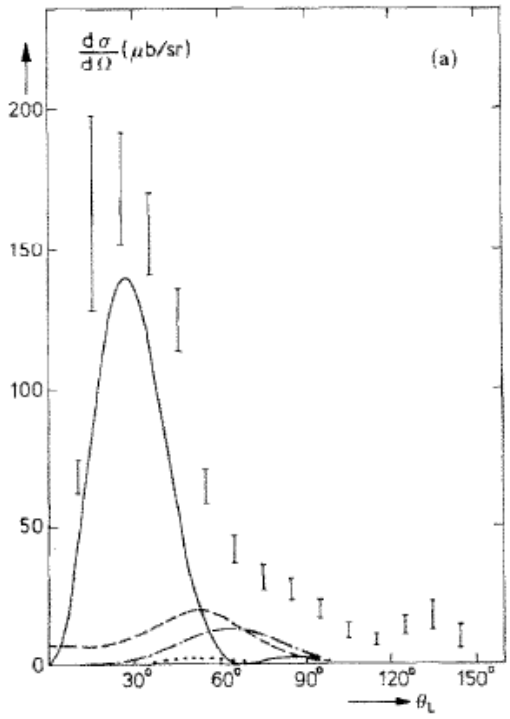

Figure 5.3: Coherent (solid line) and incoherent (dashed, dash-dot and dotted lines) π^0 photoproduction on ^{12}C. Data taken from [114].

The first step in the fitting procedure was to plot the 2D spectra of pion scattering angle, θ_π against the pion missing energy, ΔE_π for photon energies in the range of $E_\gamma = 135 - 580$ MeV, an example plot is shown in Figure 5.4.

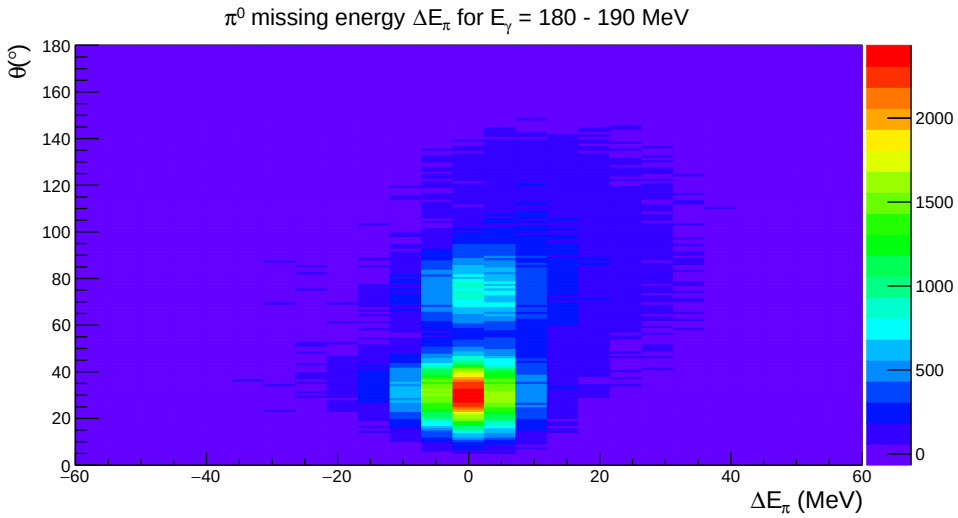

Figure 5.4: An example plot of the pion scattering angle θ_π against pion missing energy ΔE_π for the ^{116}Sn data.

These 2D spectra are then projected along the x-axis in $1-10^\circ$ angular bins. Each projection is fitted with a gaussian and the parameters of the fit are extracted. Next, these widths are ploted against the size of the angular bin and fitted with a linear function for each photon energy bin (Fig. 5.5-5.7). The value of the fit is then extracted and used to fix the value of the width of the coherent peak.

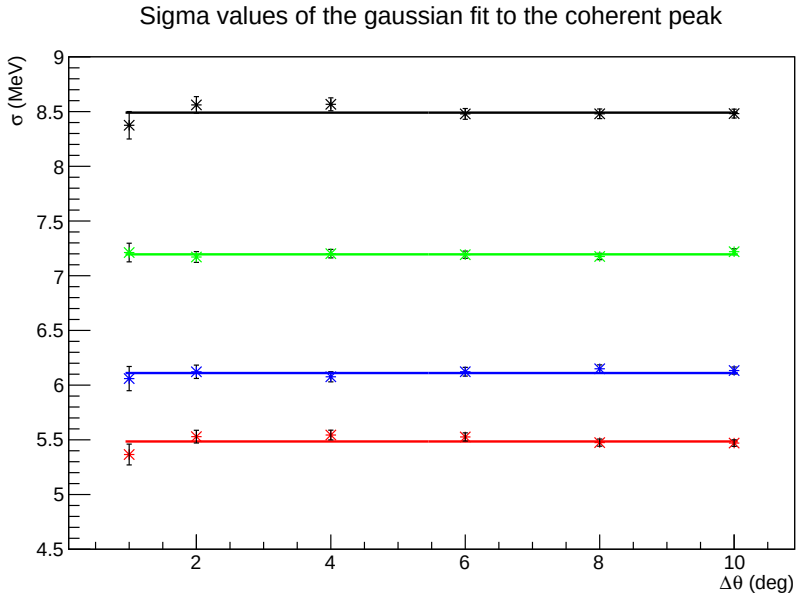

Figure 5.5: Linear fit to the width of the gaussian fit against the size of θ bin for ^{116}Sn. In red is the fit for E_γ bin 180 - 190 MeV, in blue for E_γ bin 190 - 200 MeV, in green for E_γ bin 200 - 220 MeV and in black for for E_γ bin 220 - 240 MeV.

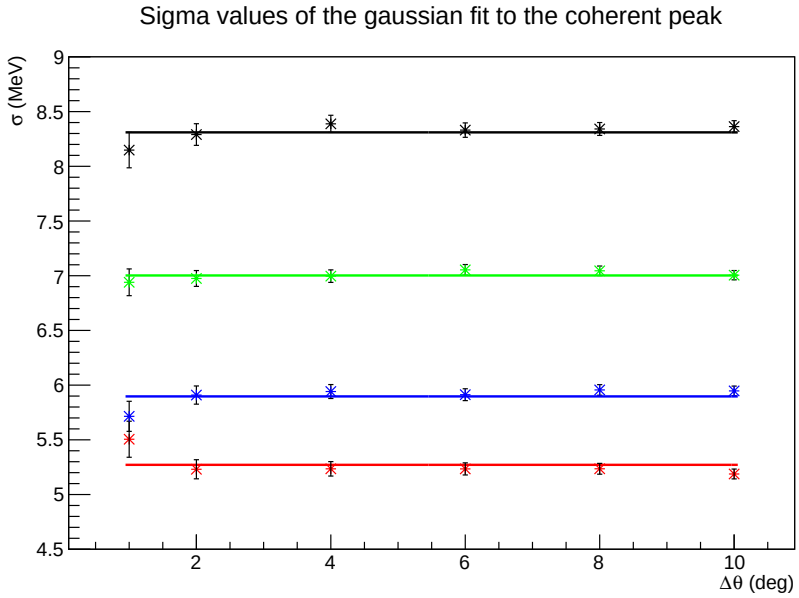

Figure 5.6: Linear fit to the width of the gaussian fit against the size of θ bin for ^{120}Sn. In red is the fit for E_γ bin 180 - 190 MeV, in blue for E_γ bin 190 - 200 MeV, in green for E_γ bin 200 - 220 MeV and in black for for E_γ bin 220 - 240 MeV.

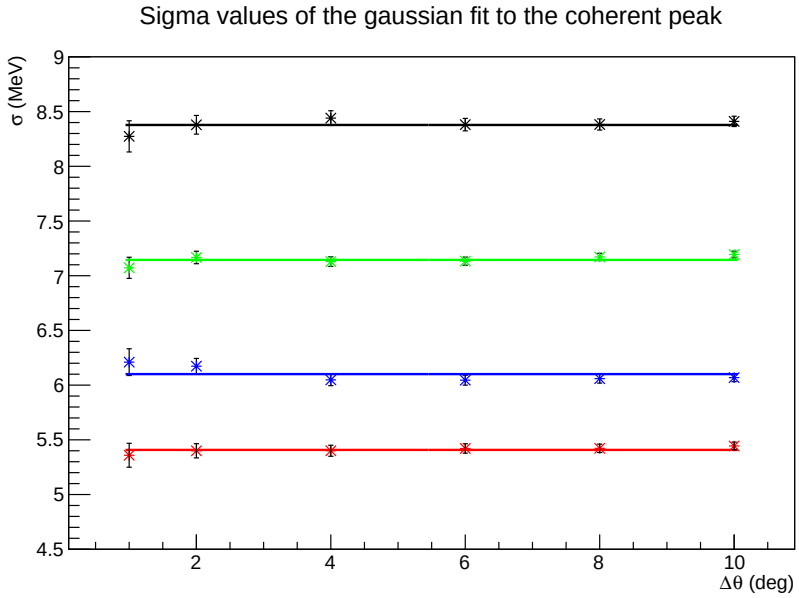

Figure 5.7: Linear fit to the width of the gaussian fit against the size of θ bin for ^{124}Sn. In red is the fit for E_γ bin 180 - 190 MeV, in blue for E_γ bin 190 - 200 MeV, in green for E_γ bin 200 - 220 MeV and in black for for E_γ bin 220 - 240 MeV.

Similarly, the value of the mean is obtained. The results of the fits are shown in figures 5.8-5.10. In this case, however, the linear fit was only applied to the results of the Gaussian fit for $2-6°$ angular bins because for larger angular bins the contribution from the background signal increased and caused the mean to shift towards larger values what was especially visible for higher photon enrgy bins.

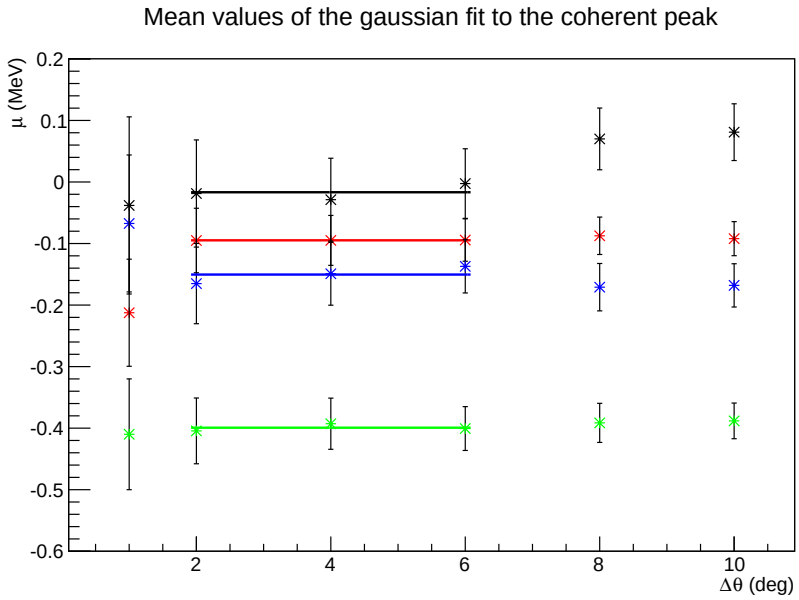

Figure 5.8: Linear fit to the mean of the gaussian fit against the size of θ bin for ^{116}Sn. In red is the fit for E_γ bin 180 - 190 MeV, in blue for E_γ bin 190 - 200 MeV, in green for E_γ bin 200 - 220 MeV and in black for for E_γ bin 220 - 240 MeV.

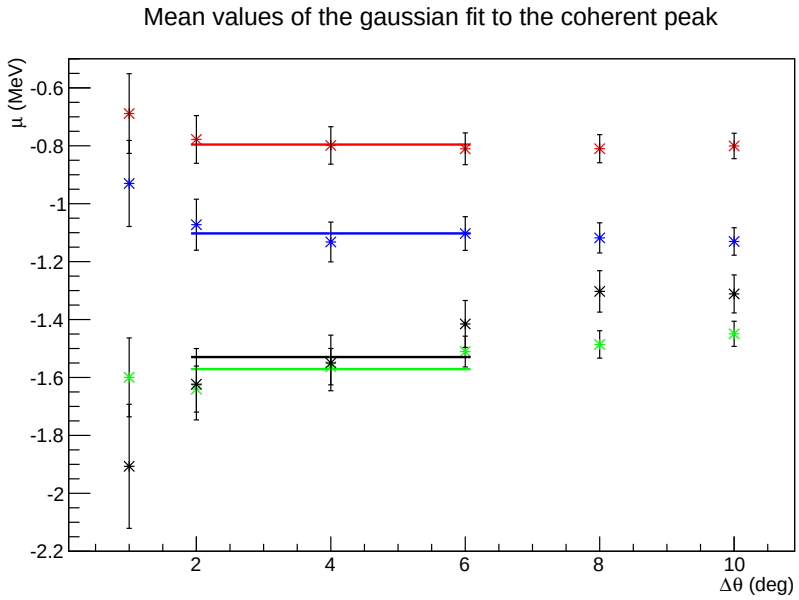

Figure 5.9: Linear fit to the mean of the gaussian fit against the size of θ bin for ^{120}Sn. Red is the fit for E_γ bin 180 - 190 MeV, in blue for E_γ bin 190 - 200 MeV, in green for E_γ bin 200 - 220 MeV and in black for for E_γ bin 220 - 240MeV.

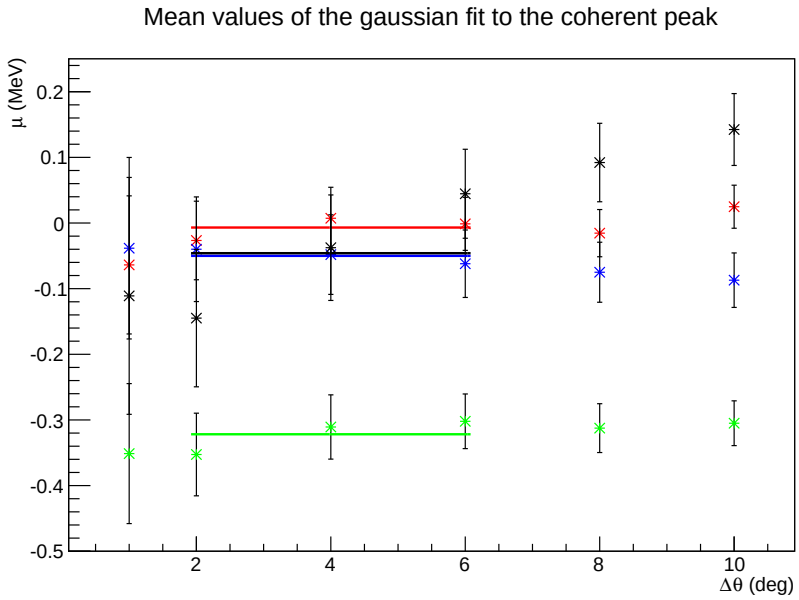

Figure 5.10: Linear fit to the mean of the gaussian fit against the size of θ bin for ^{124}Sn. In red is the fit for E_γ bin 180 - 190 MeV, in blue for E_γ bin 190 - 200 MeV, in green for E_γ bin 200 - 220 MeV and in black for for E_γ bin 220 - 240 MeV.

The second iteration, used to fit the background signal, is done with the parameters of the coherent peak fixed to the values obtained from the linear fits. In this step, the functional form consists of one gaussian describing the coherent peak and a second gaussian with free parameters that fits the incoherent signal of the background. Such form of the fitting function has been shown to adequately describe the background processes. The position and width of the second gaussian are consistent with those expected from quasi-free pion photoproduction [3]. The figure 5.11 shows the fits around the diffraction maximum and minimum.

The area of the Gaussian function fitted to the coherent peak is taken as as the coherent yield for the reaction.

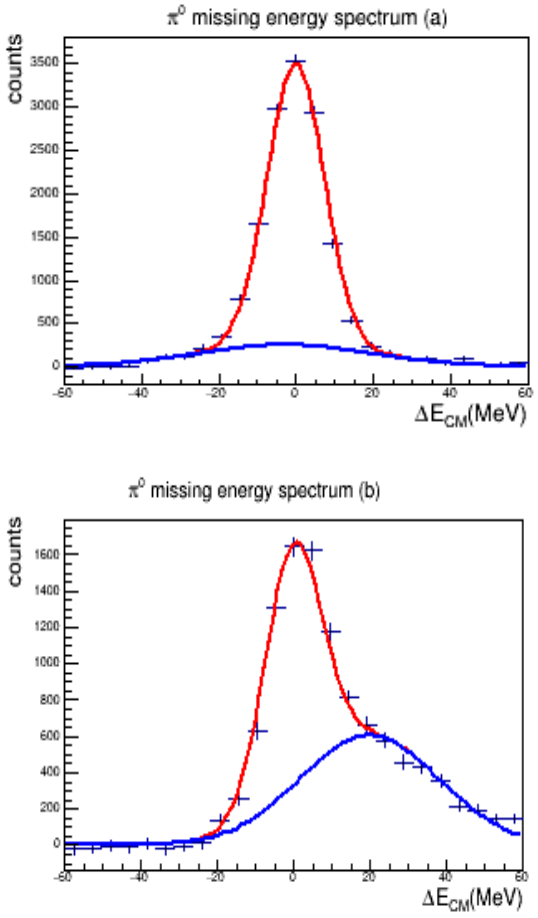

Figure 5.11: The fits to the pion missing energy spectrum for an energy bin of $E_\gamma = 220$ MeV for the ^{116}Sn target. Panel (a) shows the fit around the first diffraction maximum, and panel (b) shows the fit around the first diffraction minimum.

The yield extraction method removes the main background from quasi-free processes, but may not accurately fit any residual strength from inelastic production, in which the resiudal nucleus is left in a low lying excited state. Some of these states will be smaller than the resolution of the experiment and may result in an asymmetric gaussian peak. If their contribution was large, the fixed coherent width may not well reproduce the data or if the state is sufficiently well separated from the ground state, it may show up as an additional strength for the missing energies corresponding to the energy of the excited state. This

contribution would only be expected to be significant near the diffraction minima. From an inspection of the fits, there is no clear indication of a significant strength in the signal from inelastic processes which are resolvable with the detector resolution. A similar conclusion was found for the studies on ^{208}Pb [3], where as well as missing energy studies it was also possible to look for the produced nuclear decay photons from the inelastic processes. There was no evidene of any significant contribution from the decay photons in coincidence with a detected π^0. Such studies were not possible for the current tin data as the lowest excited states are below the detection thresholds of the CB ($\sim$ 2 MeV). Attempts to lower this threshold before the experiment resulted in unacceptably large noise signals being recorded in the data stream.

5.3 Tagging Efficiency

A determination of the tagging efficiency has been performed in order to accurately determine the beam luminosity, which is necessary to obtain absolute cross sections. As described in chapter 3, the information about the photon flux is obtained from the number of hits in the FP detector. However, when the beam passes through the collimator further photons are removed and in order to account for this reduction in the flux incident on the target a dedicated measurement is performed.

This tagging efficiency measurement utilised a close to 100% efficient photon detector, made from lead glass, which is inserted into the beamline. The run uses a much lower beam current than when in experiment mode of operation. This eliminates the contribution of random coincidences in the FP of the tagger so that only prompt photons are recorded. The ratio of the number of hits in the lead-glass detector to the number of hits in each FP detector allows the tagging efficiency to be calculated. This is done separately for each FP element. A number of tagging efficiency measurements were obtained during the run period and because of the fine tuning of the beam, its parameters were changing during the beamtime what resulted in different values of DAQ deadtime and tagging efficiency during the run.

The first step in extracting the values for tagging efficiency was to correct the measurements for the DAQ deadtime. This was done by reading the DAQ time

count that was inhibited, coresponding to the time when the system is free, and the total time count. Then the tagger scalers were scaled to take account of the obtained value of the livetime (defined as the ratio of 'inhibited' time count to the total time count) [111]. Tagging efficiency spectra are shown in figures 5.12-5.14.

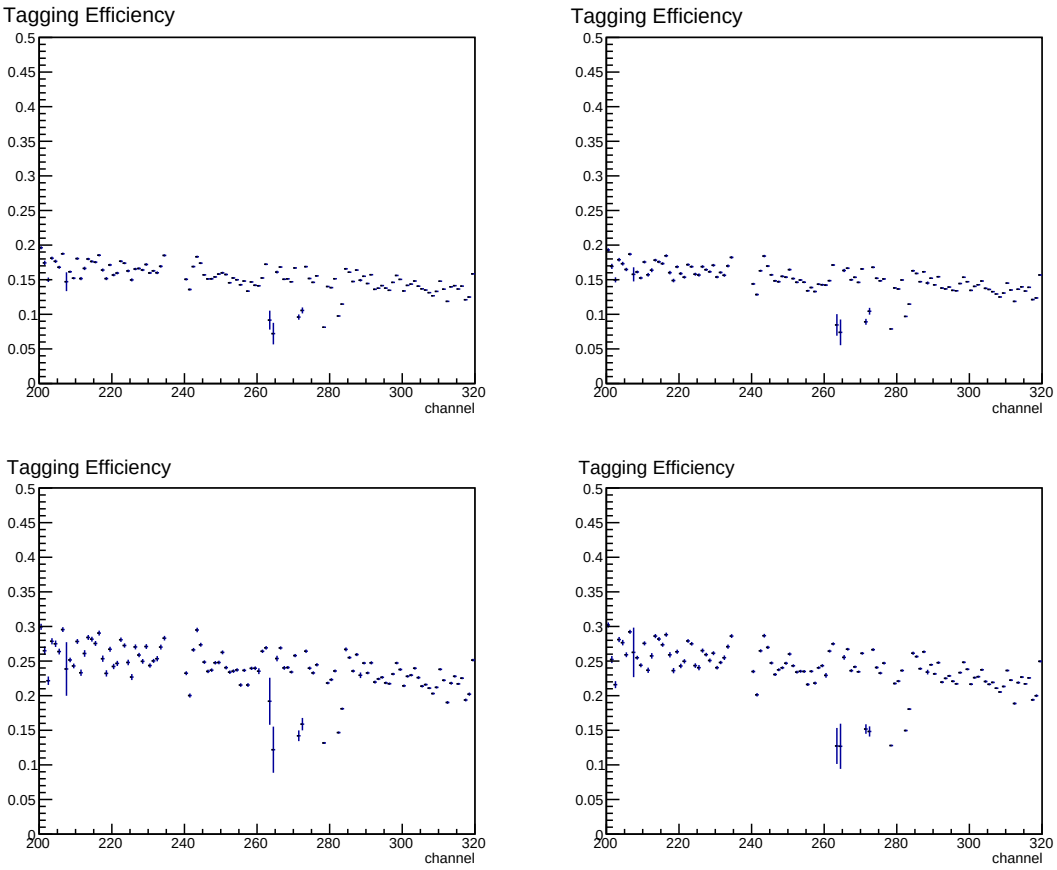

Figure 5.12: Tagging efficiency as a function of channel number for the ^{116}Sn target in the photon energy range of 135-400 MeV. The top plots shows the measurement done during the first part on the run, and the bottom plots show the tagging efficiency used for the second part of the run.

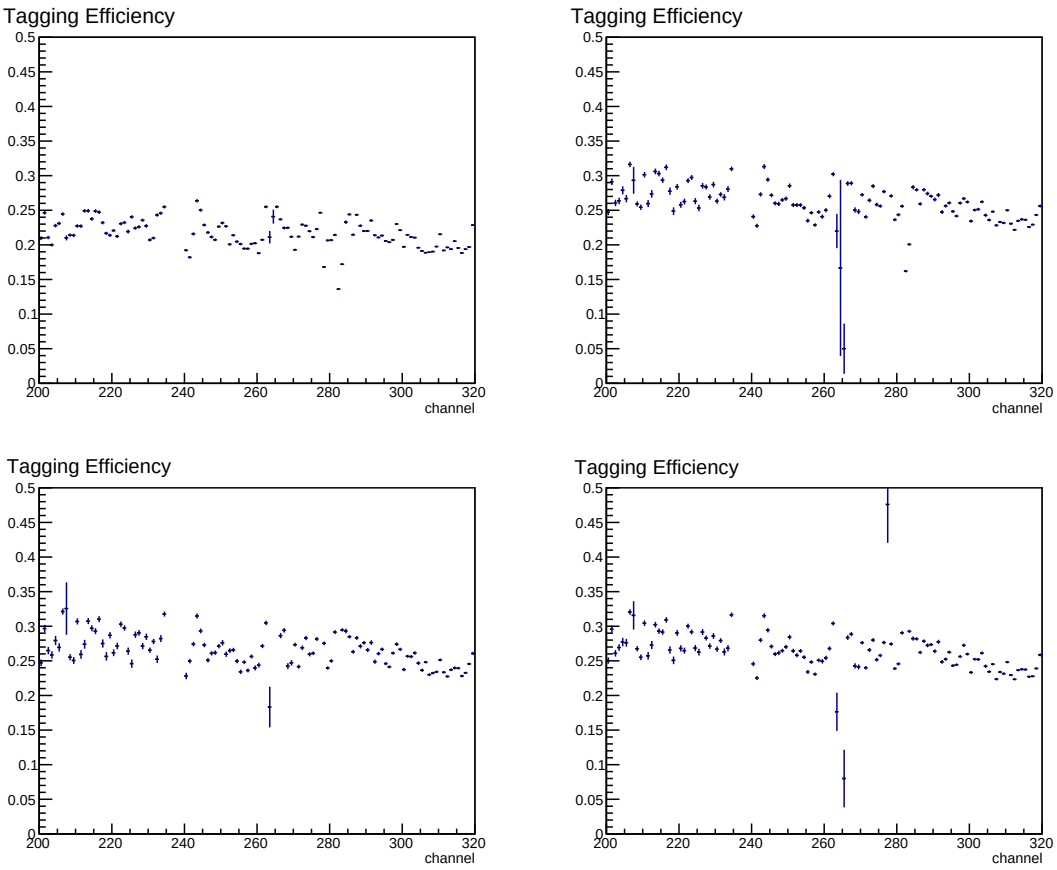

Figure 5.13: Tagging efficiency as a function of channel number for the ^{120}Sn target in the photon energy range of 135-400 MeV. The top left plot shows the measurement done during the first part on the run, the top right plot shows the measurement used for the second part of the run, and the bottom plots show the tagging efficiency used for the third part of the run.

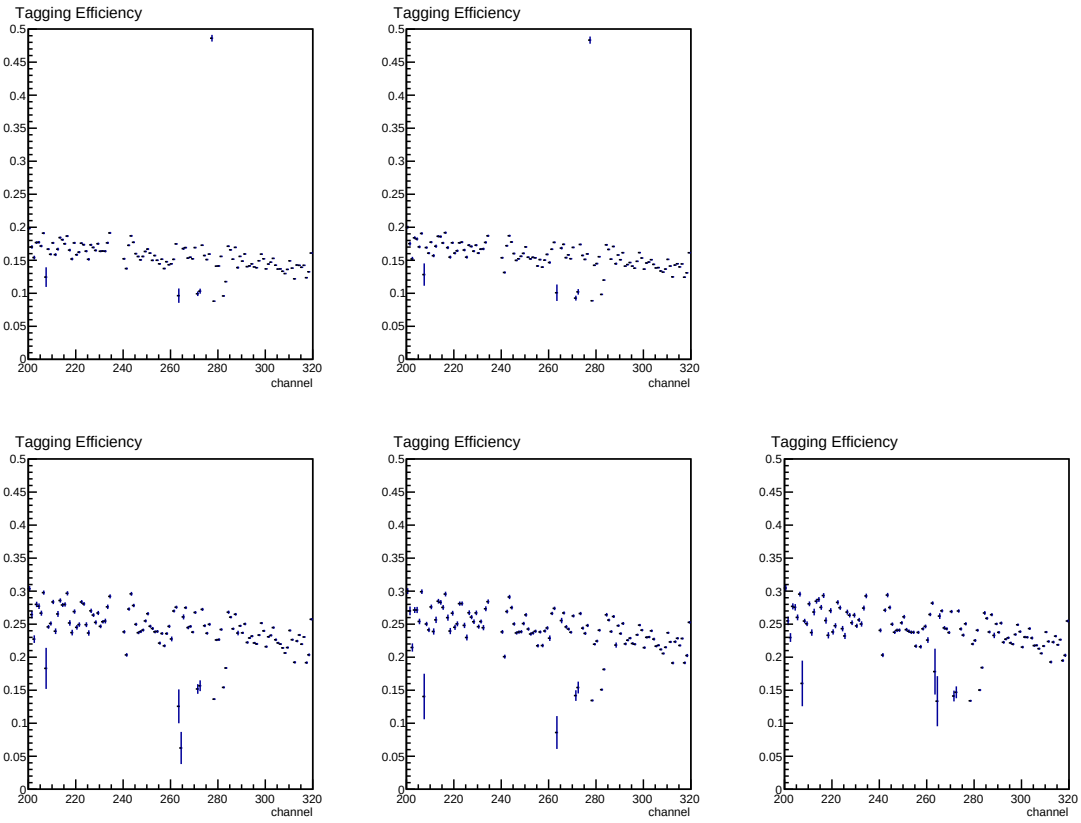

Figure 5.14: Tagging efficiency as a function of channel number for the ^{124}Sn target in the photon energy range of 135-400 MeV. The top plots shows the measurement done during the first part on the run, and the bottom plots show the tagging efficiency used for the second part of the run.

The values of the tagging efficiency were applied as a correction to the targets' scalers information for the corresponding periods of the runs in the cross sections calculations.

5.4 π^0 Detection Efficiency

A GEANT4 Monte Carlo simulation has been used to calculate the efficiency of the detector setup for the detection of π^0 mesons. This efficiency needs to be determined as a function of both the pion angle and the incident photon energy. The efficiency is used to correct the measured yield of pions to the actual yield

produced in the reaction on a bin by bin basis.

The efficiency is calculated by passing generated pseudo-events through the GEANT4 simulation of the detector apparatus. The $A(\gamma, \pi^0)A$ events have been generated for the energy range of 135-540 MeV, for each target. The simulated events include the measured target offsets and the thicknesses of the different targets. The pions are generated with an isotropic angular distribution so that all bins are populated. The GEANT4 simulation tracks the events through the detector apparatus and models the timing and magnitude of the energy deposits in each of the detector elements of the CB. The resulting data is then output in a form which can be analysed with the same analysis software as the experimental data. The energy resolution of the CB crystals are adjusted globally so that the reconstructed missing mass of the π^0 has a similar width to the experimental data.

In order to optimise the time required for the simulation, the minimum number of generated events was estimated. This minimised number was based on an analysis of the resulting impact on the error in the cross sections due to the statistical accuracy with which the detection efficiency (ϵ_{det}) is determined. The typical error in the yield of reconstructed pion events in the coherent peak was $\sim 1\%$. Achieving this accuracy in the simulation required an event sample of around 10 million events.

The detection efficiency has been calculated for each energy and θ bin as the the ratio of the total number of detected π^0's to the total number of π^0's generated in that energy and θ bins. The results are shown in figures 5.15, 5.16 and 5.17. The ^{120}Sn target shows a slightly higher pion detection efficiency as it was thinner than the other 2 targets. Because of this, fewer pion decay photons are absorbed in the target before they reach the CB or TAPS detectors. The detection efficiency data were fitted with a three part polynomial. In the $0^\circ - 40^\circ$ and $140^\circ - 180^\circ$ ranges, a second degree plynomial functions were used and the $40^\circ - 140^\circ$ region was fitted with a polynomial of the fourth degree (see equations 5.7-5.9).

$$for \theta = 0^\circ - 40^\circ : y = a\theta^2 + b\theta + c \tag{5.7}$$

$$for \theta = 40^\circ - 140^\circ : y = d\theta^4 + e\theta^3 + f\theta^2 + g\theta + h \tag{5.8}$$

$$for \theta = 140^\circ - 180^\circ : y = i\left(\theta - 180^\circ\right)^2 + j\left(\theta - 180^\circ\right) + k \tag{5.9}$$

where a, b, d, e, f, g, h. i and j are free parameters and c and k are defined in equations 5.10 and 5.11 respectively.

$$c = (40°)^4\, d + (40°)^3\, e + (40°)^2\, f + 40°g + h - \left(a\theta^2 + b\theta\right) \tag{5.10}$$

$$k = (140°)^4\, d + (140°)^3\, e + (140°)^2\, f + 140°g + h - i\,(140° - 180°)^2 + j\,(140° - 180°) \tag{5.11}$$

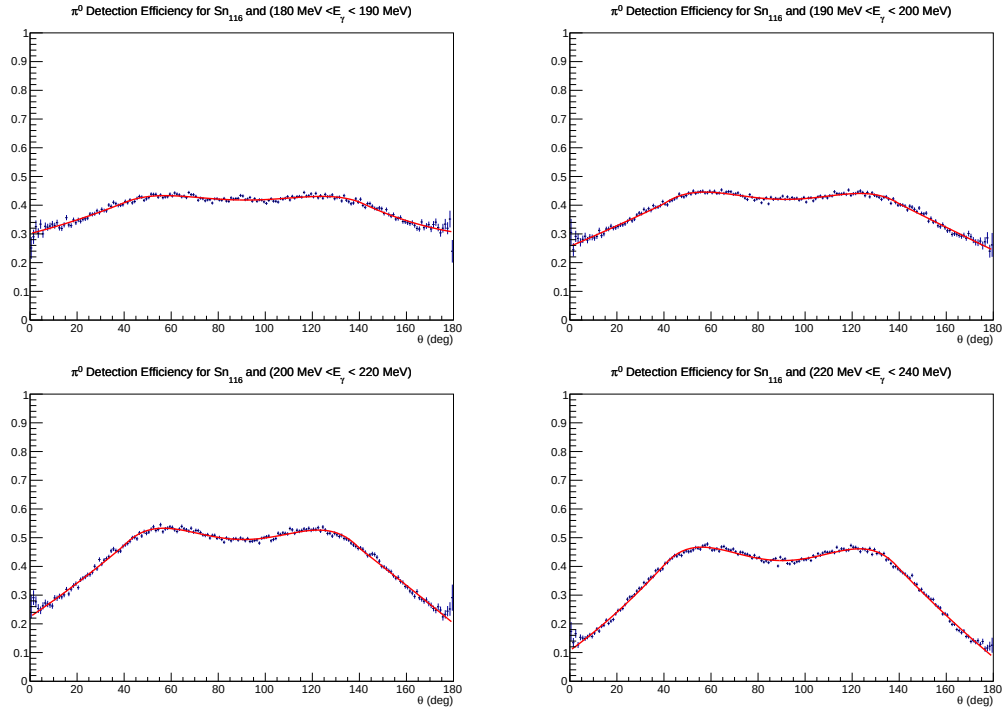

Figure 5.15: Dependence of the detection efficiency on energy and θ_{π^0} for the ^{116}Sn target. Red line is a three part polynomial fit.

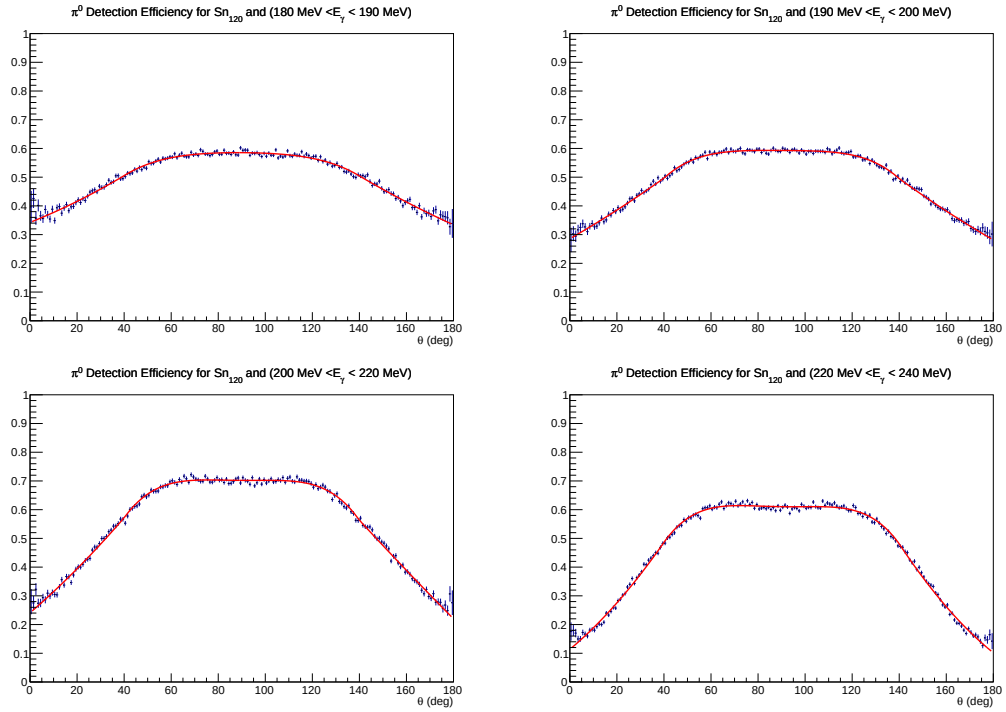

Figure 5.16: Dependence of the detection efficiency on energy and θ_{π^0} for the ^{120}Sn target. Red line is a three part polynomial fit.

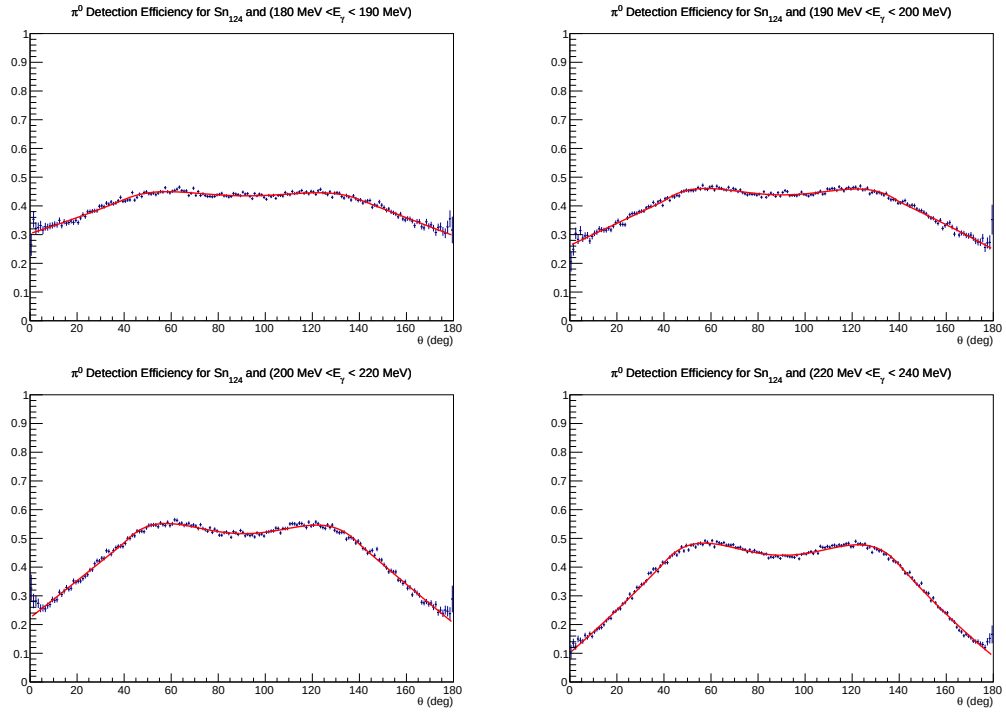

Figure 5.17: Dependence of the detection efficiency on energy and θ_{π^0} for the ^{124}Sn target. Red line is a three part polynomial fit.

5.5 Cross Sections Measurements

This section outlines how the coherent pion photoproduction cross sections are calculated from the measured yield of pion events. From the definition, cross section is a measure of probability that a certain reaction will take place under specified conditions. The probability for a reaction $A(a,b)B$ to take place is defined as:

$$\sigma = \frac{N_b}{N_a N_A} \tag{5.12}$$

where N_a is the number of incident particles per unit area, N_A is the number of target particles per unit area visible to the beam and N_b is the number of emitted particles.

In this experiment, N_a is the incident photon flux calculated from the number of hits in the tagger scalers corrected with the tagging efficiency, N_A is the surface

density of the target as seen by the beam, and N_b is the π^0 yield corrected with the detection efficiency.

The differential cross section is a derivative of the total cross section with respect to the solid angle. For a given photon energy bin, E_γ, and pion scattering angle, θ_{π^0}, it can be expressed as:

$$\frac{d\sigma}{d\Omega} = \frac{N_{\pi^0}}{N_s \epsilon_{tagg} \epsilon_{det} \rho_a \Omega \Gamma_{\gamma\gamma}} \tag{5.13}$$

where N_{π^0} is the number of π^0's detected in the given E_γ and θ_{π^0} bins. N_s is the count of the tagger scalers in the given E_γ bin. ϵ_{tagg} is the tagging efficiency in the given E_γ bin and ϵ_{det} is the detection efficiency in the given E_γ and θ_{π^0} bins. ρ_a is the target surface density in $nuclei/cm^2$. $\Gamma_{\gamma\gamma}$ is the branching ratio of the decay, and Ω is the solid angle of detection, defined as:

$$\Omega = \int_{\phi_1}^{\phi_2} d\phi \int_{\theta_1}^{\theta_2} sin\theta d\theta \tag{5.14}$$

5.6 Error Analysis

In evaluating the cross section as well as the statistical uncertainties, which simply derive from the measured yield of pions in a given bin, systematic uncertainties must be assesed. Estimates of the systematic errors affecting the measurement are outlined below.

One of the sources of the systematic error is the uncertainty due to the surface density calculations. It arises from the target thickness measurements, and for the ^{116}Sn and ^{124}Sn targets, it is of order $\sim 1\%$ and for the ^{120}Sn target it is $\sim 2\%$.

Another source of systematic error comes from the fitting procedure for the π^0 yield from the missing energy analysis. Inaccuracies in the chosen fitting functions or the shape of the background could introduce systematic errors in the extracted yield. From inspection of the fits in the coherent region and near the minima, where the background is more clearly seen, it is estimated that the coherent yield is obtained with a systematic error below 5%. This was estimated by variation of the fitted functions while still getting acceptable agreement with the data.

There are also sources of the statistical error in the evaluating quantities used

to extract the cross section. There is a statistical error on the tagging efficiency evaluated for each FP detector. As the data is binned with each photon energy bin using around 4 channels then the effect of this on each bin is reduced. The error on tagging efficiency comes from the fact that the experiment measures a probability and as such follows Poisson's statistics. The statistical error on ϵ_{tagg} was estimated to be around 1% for all channels. The pion detection efficiency was established to a statistical accuracy of 1%.

Combining the errors in quadrature gives an overall systematic error for the measured cross sections of around 6%. However, it should be noted that when taking the ratio the systematics will largely cancel as they will be common to the data from both targets used in the ratio.

5.7 Incorporating the Experimental Resolution into the Model Predictions

To compare with the experimental data the predictions of the DKT model need to be folded with the experimental resolution and binning.

Averaging of the calculations over the photon energy is straightforward. The model is calculated for every 2 MeV photon energy and then the model calculations are averaged over the photon energy bins in the analysis.

Incorporating the angular resolution of the pion requires input from the simulation. To extract this a full analysis of simulated pseudo-data was underatken, using the same software routines used to extract the pion angle in the data analysis. The initial "true" angle of the pion was recorded with each event and this allowed the difference between the true and the reconstructed pion angle to be determined. The resulting distribution was fitted with a gaussian function whose width was taken as the angular resolution of the detector apparatus.

The dependence of the θ resolution for different targets and photon energies is shown in the figures 5.18 - 5.20. The non-uniformity in the distribution is caused by the segmented crystal structure of the CB. The data have been fitted with a third degree polynomial function which was then used to extract the pion angular resolution as a function of pion (photon) energy. This was used in the DKT calculations to smear the theoretical cross sections to allow a direct comparison of theory and data.

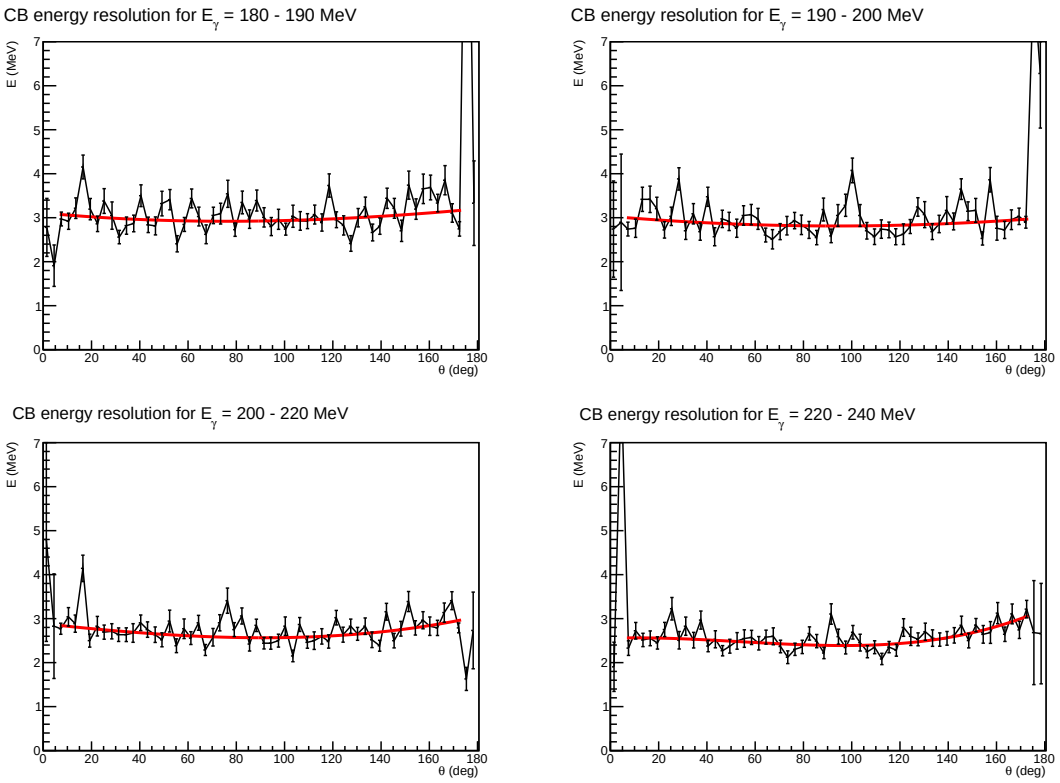

Figure 5.18: The example plots of the energy resolution dependence on the angular bin, θ_π, and the photon energy bin, E_γ. Data for the ^{116}Sn target.

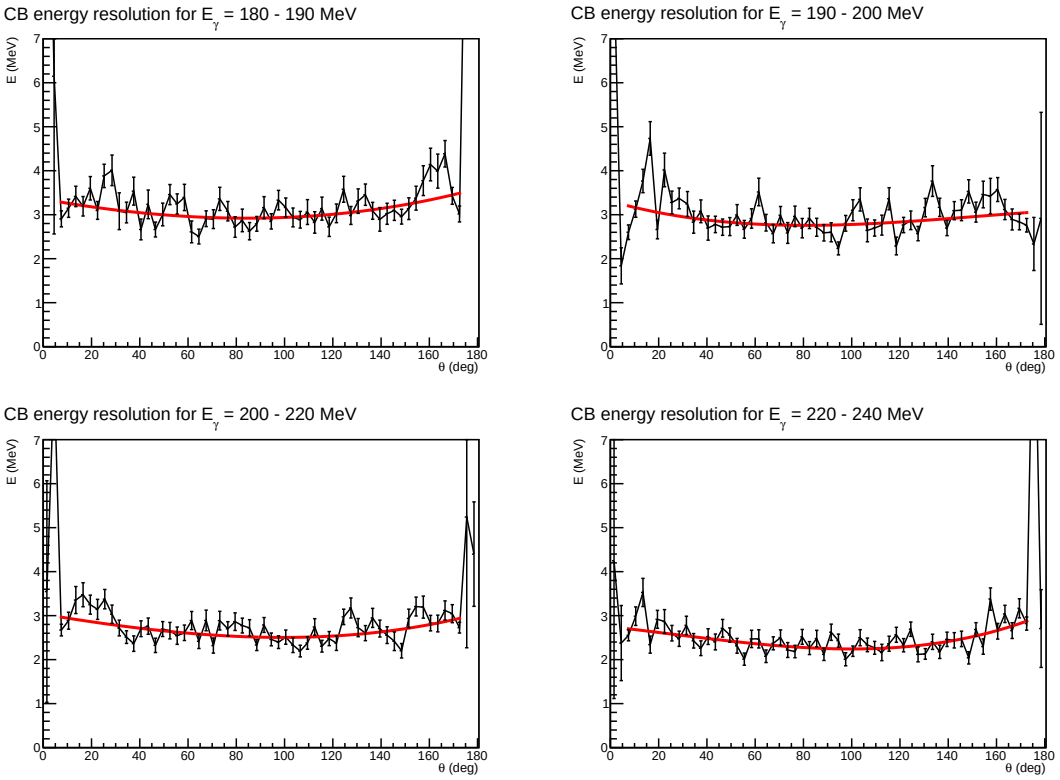

Figure 5.19: The example plots of the energy resolution dependence on the angular bin, θ_π, and the photon energy bin, E_γ. Data for the ^{120}Sn target.

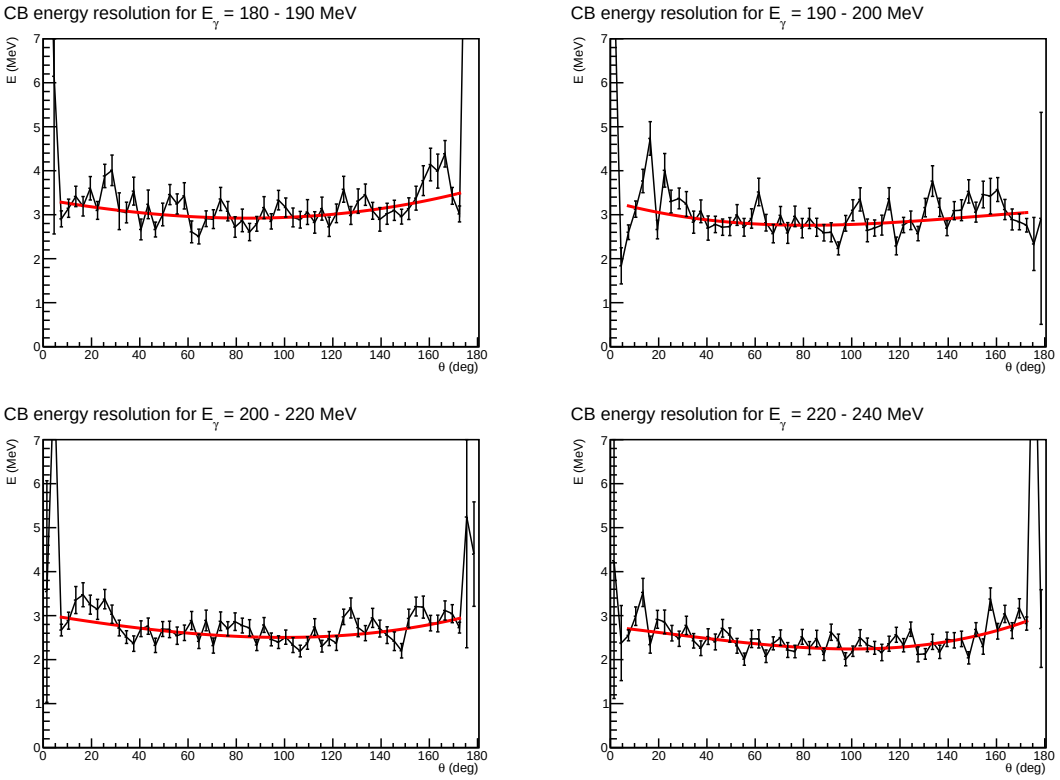

Figure 5.20: The example plots of the energy resolution dependence on the angular bin, θ_π, and the photon energy bin, E_γ. Data for the ^{124}Sn target.

To summarize, this chapter details all the steps taken to analyse the experimental data and extract the cross sections of the coherent π^0 photoproduction on tin targets, allowing to compare the experimental data with various predictions of the nuclear models. Next chapter presents the results of this anlaysis.

Chapter 6

Results

This chapter presents the results of the measurements of the cross sections for the coherent π^0 photoproduction on ^{116}Sn, ^{120}Sn and ^{124}Sn. The experimental data are compared with the theoretical calculations from the DKT model for coherent pion photoproduction.

6.1 Cross Sections

The differential cross sections for all the targets are presented in figures 6.1 - 6.3. The cross sections are presented in a linear scale and also in a log scale so that the detailed shape in the minima can be better observed. The expected diffraction pattern due to the matter form factor is clearly present in the cross sections and up to three diffraction maxima can be seen in the data. Indications of structures around the 4th maxima are also evident although the structure is not well resolved.

Also presented on the plots are the DKT model predictions. As described in the previous chapter the DKT model predictions have been smeared with the experimental pion angle resolution and averaged over the photon energy bin so the data and theory can be compared directly. The smearing does not affect the height of the maxima significantly but tends to fill in the minima. The model calculations are done for a range of values of the 2PF parameters for the charge and matter distribution. However, it should be noted that 2PF parameters are predicted from an energy density functional and all give very similar values for the matter radius. Nevertheless, they suffice for this first comparision with the

data. The model gives a reasonable description of the data for all tin targets. The maxima and minima positions are are in generally good agreement with those observed in the experimental data. The agreement for the higher photon energy bin for ^{124}Sn looks poorer than the other targets, in terms of both the position of the maxima/minima. The height of the maxima are also in reasonable agreement, although the model tends to underestimate the predicted height of the first maxima by around 20% at E_γ = 200 - 220 MeV.

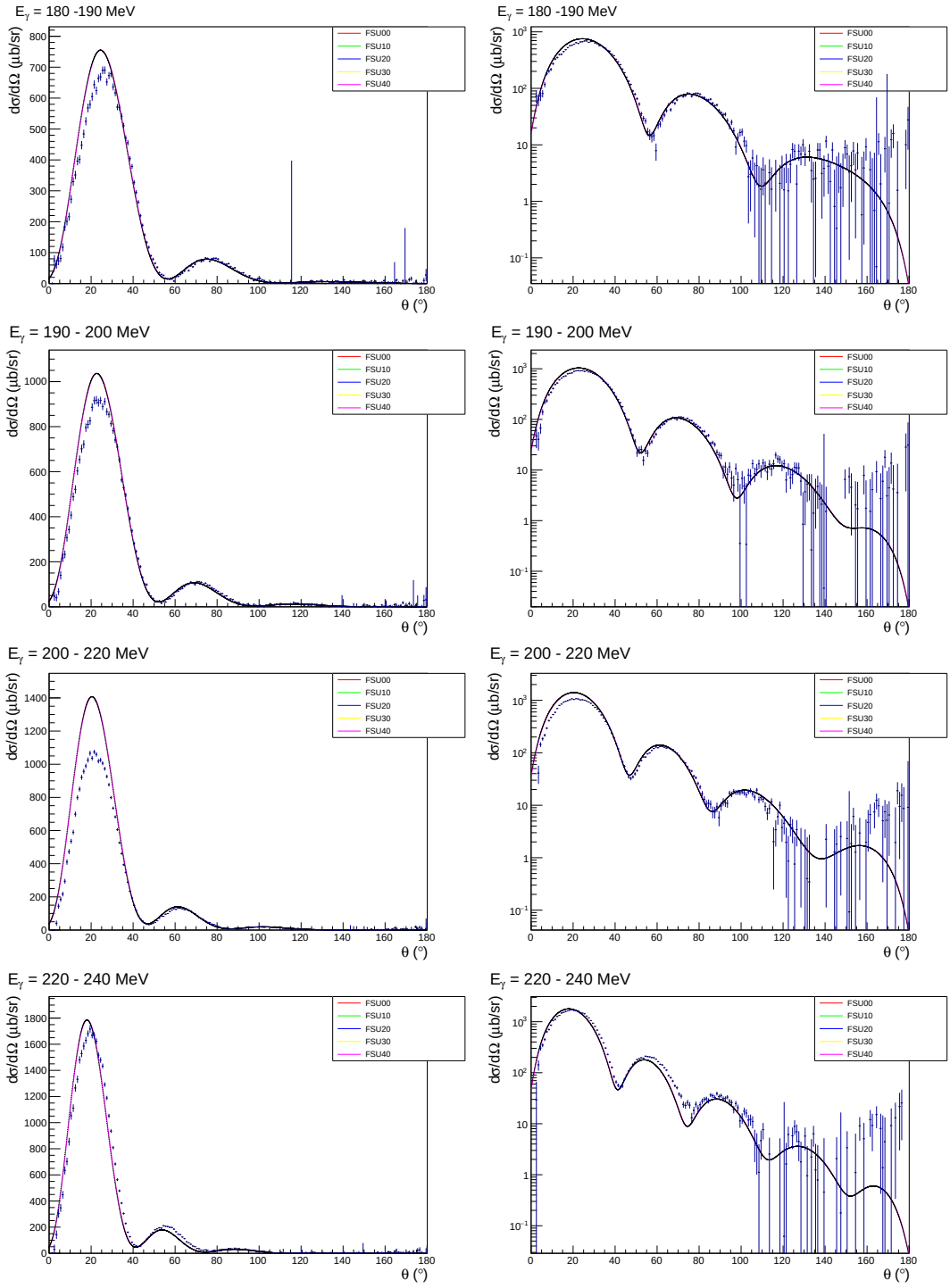

Figure 6.1: Differential cross sections for the ^{116}Sn target for the photon energy bins in the E_γ range of 180 - 240 MeV.

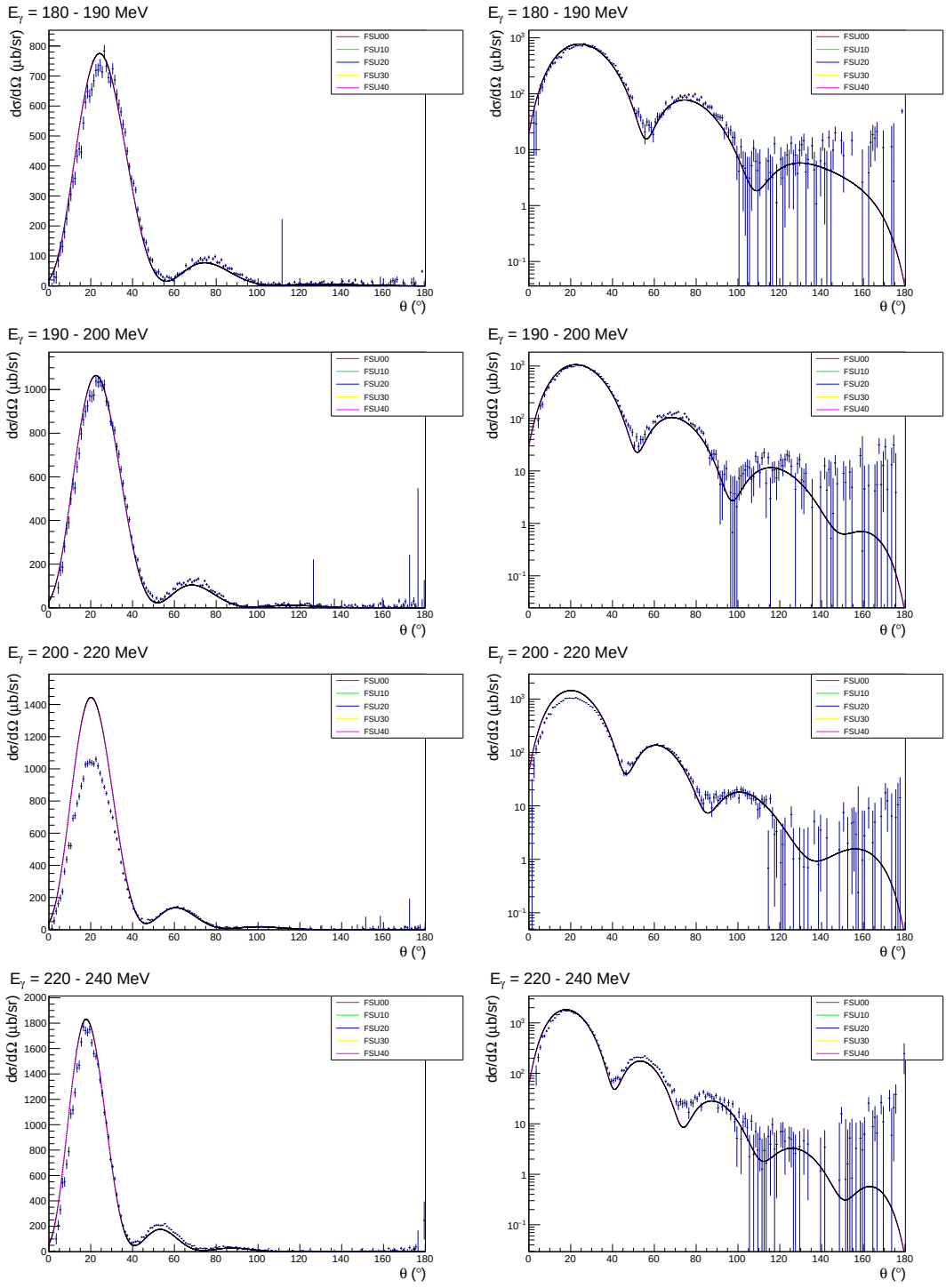

Figure 6.2: Differential cross sections for the ^{120}Sn target for the photon energy bins in the E_γ range of 180 - 240 MeV.

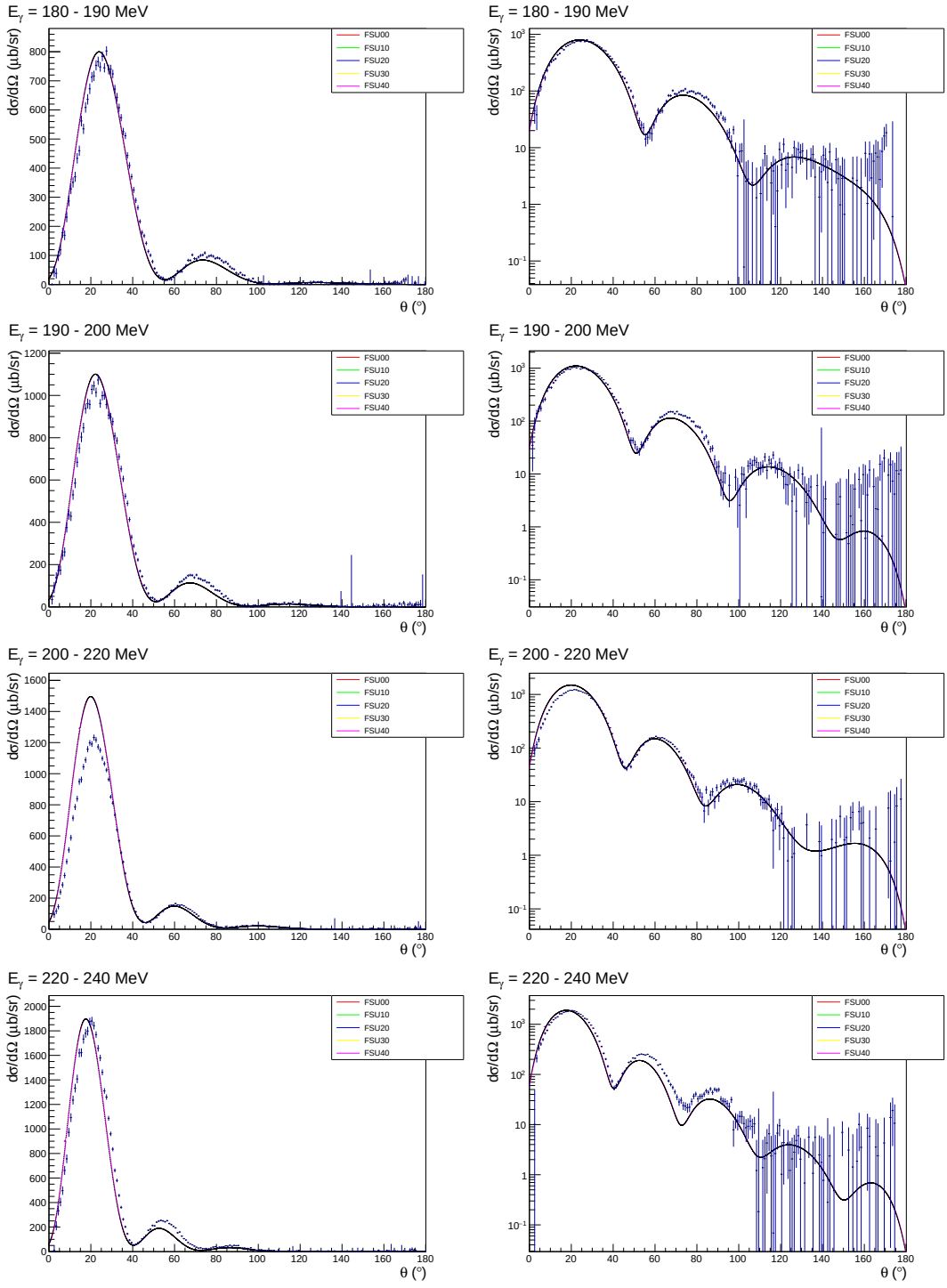

Figure 6.3: Differential cross sections for the ^{124}Sn target for the photon energy bins in the E_γ range of 180 - 240 MeV.

Calculations of the ratio of the cross sections between the isotopes were done in order to investigate the changes in the nuclear structure of the isotopes with reduced bias from experimental systematic errors. These ratios are presented for the different targets and different photon energy bins in figures 6.4 to 6.6. It is clear from the data that the experiment is indeed sensitive to the difference in the matter form factor between the nuclei. For the case of identical matter form factors or matter form factors with differences not resolvable within the detector resolution, the ratio would be expected to be a flat line at unity. However, clear structures are evident in the data in the approach to the diffraction minima. Due to the differences in the matter form factors for the different targets, the minima position occur at different pion angles. For larger matter radii the minima positions would move to progressively smaller pion θ angles. For the case where the denominator in the ratio has the smaller matter radius, the result is a structure which initially rises with the increasing θ due to the fall off in the yield from the larger nucleus. Following this the shape of the structure is determined by the detailed shape of the minima in the 2 nuclei. Such structures are clearly evident in the data.

The experimental ratios are compared to the theoretical predictions from the DKT calculations, using the FSUGold parameter sets [41]. The details of different FSUGold models are summarized in the Table 6.1. The general features of the data are reproduced by the models which gives confidence that the structures are related to the change in matter radii (Fig. 6.4 - 6.6).

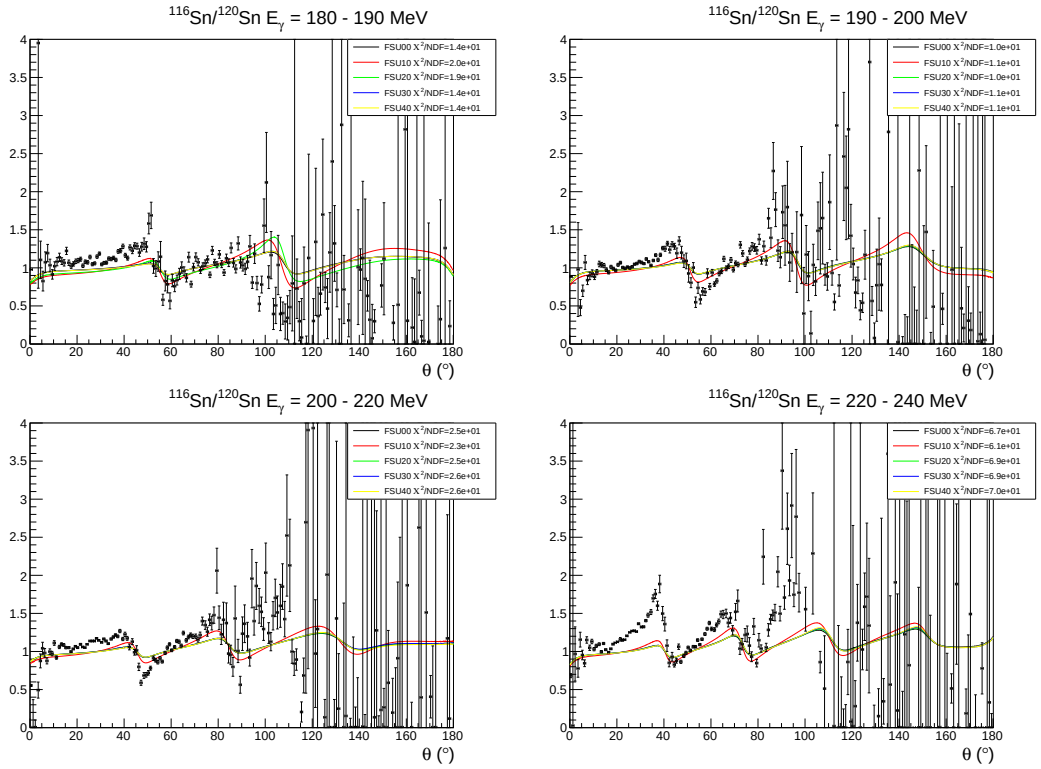

Figure 6.4: The ratio of the cross sections of ^{116}Sn to ^{120}Sn for the E_γ bins in the photon energy range of 180 - 240 MeV compared with the DKT calculations using different FSUGold parameter sets. Top left plot shows E_γ = 180 - 190 MeV, top right shows E_γ = 190 - 200 MeV, bottom left shows E_γ = 200 - 220 MeV and bottom right shows E_γ = 220 - 240MeV.

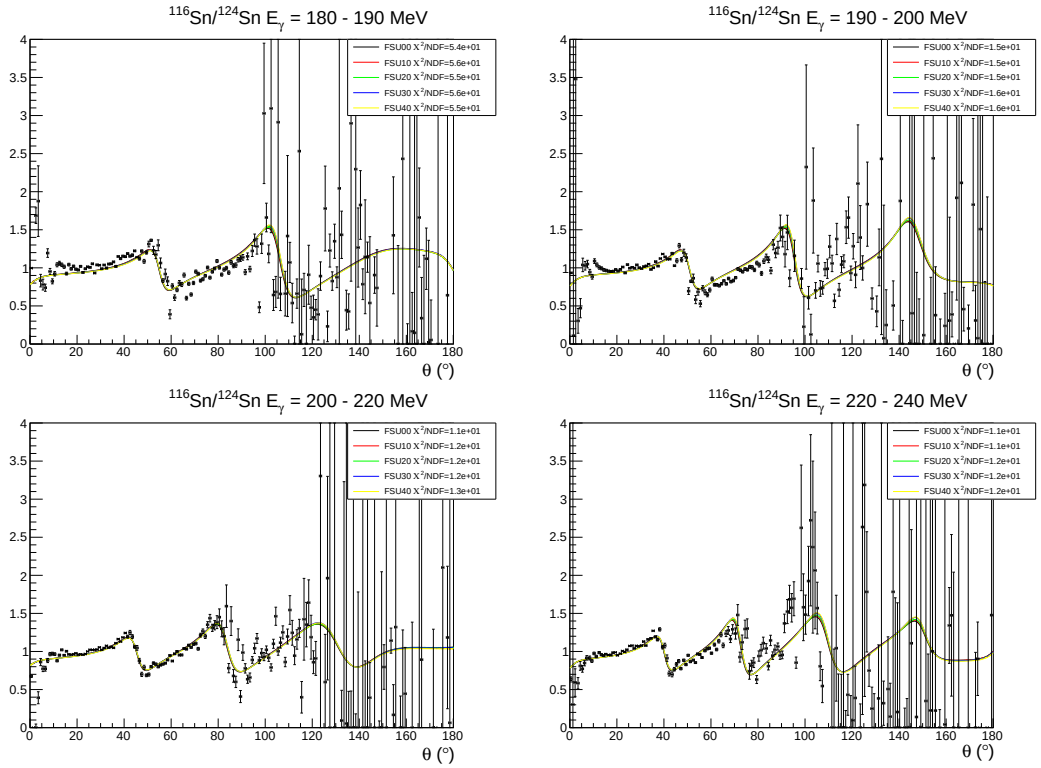

Figure 6.5: The ratio of the cross sections of ^{116}Sn to ^{124}Sn for the E_γ bins in the photon energy range of 180 - 240 MeV compared with the DKT calculations using different FSUGold parameter sets. Top left plot shows E_γ = 180 - 190 MeV, top right shows E_γ = 190 - 200 MeV, bottom left shows E_γ = 200- 220 MeV and bottom right shows E_γ = 220 - 240 MeV.

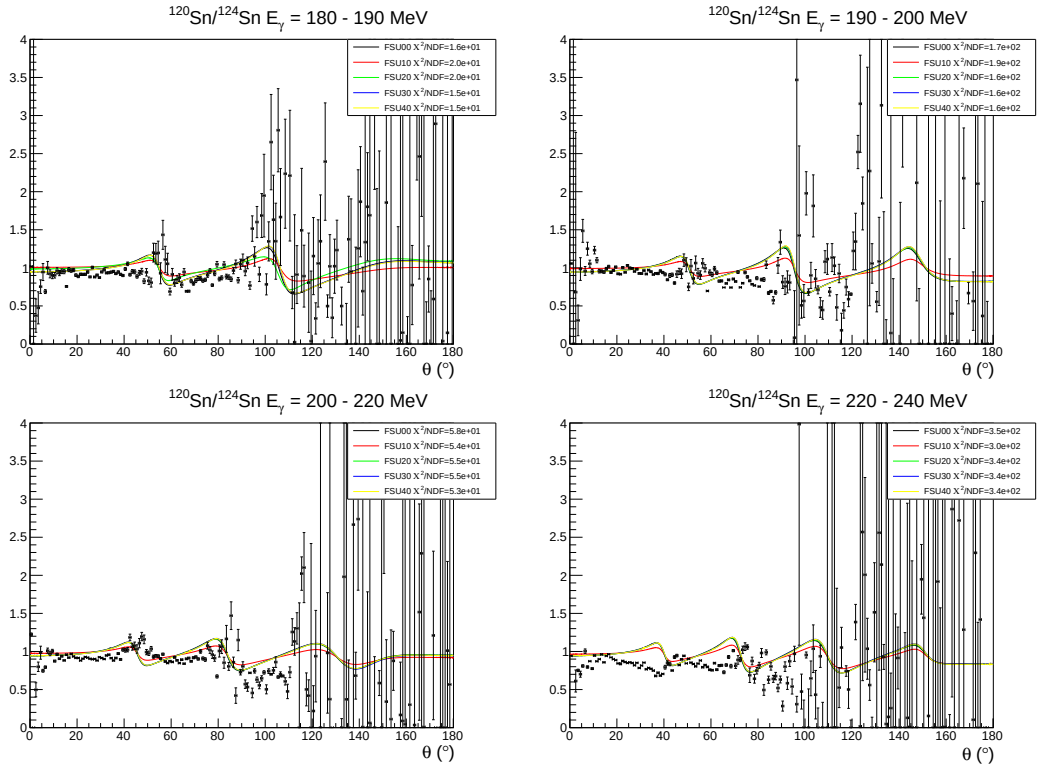

Figure 6.6: The ratio of the cross sections of ^{120}Sn to ^{124}Sn for the E_γ bins in the photon energy range of 180 - 240 MeV compared with the DKT calculations using different FSUGold parameter sets. Top left plot shows E_γ = 180 - 190 MeV, top right shows E_γ = 190 - 200 MeV, bottom left shows E_γ = 200- 220 MeV and bottom right shows E_γ = 220 - 240 MeV.

The DKT calculations reproduce the general features of the structures visible in the ratio plots. The predicted shapes of the cross section ratios near the diffraction minima give a reasonable general description of the features in the experimental data, providing support that this measurement gives sensitivity to the evolution of a neutron skin. Detailed agreement is not observed for some target ratios and energy bins. However as the detailed shape depends on the the employed charge and neutron distributions in the DKT model these disagreements may reflect the need for iteration of these parameters. There is no clear difference between the DKT calculations for different FSUGold parameter sets, however, those parameters have been calculated from a fit to the global set of the experimental data and not specifically for the tin isotopes.

As discussed previously these currently available predictions all give very similar matter radii and therefore would not be expected to show strong differences. Further work will take a wider range of functionals and also include constraints from the measured charge distributions and other observables for the tin isotopes.

6.2 Discussion and Further Work

Only comparison with five density fuctionals derived from the FSUGold have been completed to date. The next stage is to compare the data with a broad range of density functionals and to establish which of these contain nuclear structure information that most closely matches the data. This will be done using a Chi square minimisation analysis.

The FSUGold density functionals employed in this thesis show variations in the rms proton radius of up to 0.02 fm. This is likely due to the functionals being tuned to a global set of experimental data and not specifically to the tin isotopes. For more detailed analysis new functionals need to be developed which are tuned to the experimental data on the charge distribution. This was measured by I. Angeli from a combination of electron scattering and X-ray analysis and found to be 4.6266 ± 0.0015 fm, 4.6543 ± 0.0009 fm and 4.6759 ± 0.0012 fm for ^{116}Sn, ^{120}Sn and ^{124}Sn, respectively [115].

Tuned functionals were not available at the time of writing of this thesis but should be developed by the theorists now that the data is available. This will enable more definite conclusions to be made. However, the current results are a succesful first step, showing that the coherent pion photoproduction holds real promise for providing new and valuable constraints on the neutron skin evolution across an isotopic chain.

	FSUGold						
Isotope	c_p (fm)	b_p (fm)	c_n (fm)	b_n (fm)	r_p (fm)	r_n (fm)	Δr (fm)
^{116}Sn	5.479	0.434	5.458	0.529	4.541	4.663	0.122
^{120}Sn	5.503	0.443	5.461	0.583	4.570	4.752	0.182
^{124}Sn	5.563	0.432	5.581	0.570	4.598	4.814	0.216
	FSU000						
Isotope	c_p (fm)	b_p (fm)	c_n (fm)	b_n (fm)	r_p (fm)	r_n (fm)	Δr (fm)
^{116}Sn	5.457	0.435	5.498	0.532	4.526	4.696	0.170
^{120}Sn	5.473	0.445	5.515	0.586	4.551	4.795	0.244
^{124}Sn	5.533	0.433	5.644	0.573	4.579	4.863	0.284
	FSU010						
Isotope	c_p (fm)	b_p (fm)	c_n (fm)	b_n (fm)	r_p (fm)	r_n (fm)	Δr (fm)
^{116}Sn	5.464	0.435	5.484	0.531	4.530	4.685	0.155
^{120}Sn	5.482	0.444	5.496	0.585	4.556	4.780	0.224
^{124}Sn	5.541	0.433	5.622	0.572	4.584	4.846	0.262
	FSU020						
Isotope	c_p (fm)	b_p (fm)	c_n (fm)	b_n (fm)	r_p (fm)	r_n (fm)	Δr (fm)
^{116}Sn	5.471	0.435	5.471	0.530	4.535	4.674	0.139
^{120}Sn	5.492	0.444	5.478	0.584	4.562	4.766	0.246
^{124}Sn	5.551	0.432	5.601	0.571	4.590	4.830	0.240
	FSU040						
Isotope	c_p (fm)	b_p (fm)	c_n (fm)	b_n (fm)	r_p (fm)	r_n (fm)	Δr (fm)
^{116}Sn	5.489	0.435	5.445	0.528	4.548	4.652	0.104
^{120}Sn	5.516	0.444	5.442	0.582	4.580	4.738	0.158
^{124}Sn	5.577	0.432	5.561	0.568	4.608	4.797	0.189

Table 6.1: The FSUGold parameters set used for the Kamalov's DKT calculations. Five different values for the paramenters are used and compared with the data: FSUGold the original parameter set by [56] and four other functionals derived from this set, which correspond to larger and smaller values of the neutron skin.

Chapter 7

Conclusion

This thesis presents a pioneering study to obtain accurate information on the evolution of the neutron radial distributions across an isotopic chain of nuclei using an electromagnetic probe. The thesis presents the first measurement of coherent pion photoproduction with multiple isotopic targets, obtained at the MAMI facility using the Crystal Ball detector apparatus. Differential cross sections for coherent π^0 photoproduction have been determined for three tin isotopes, ^{116}Sn, ^{1120}Sn and ^{124}Sn in the photon energy range 180-240 MeV. The results have been compared to the theoretical calculations of the DTK model for coherent pion photoproduction. The input nuclear structure information for the model was taken from those predicted by the FSUGold relativistic mean field nuclear sructure calculation.

The experimental data was used to produce a ratio of the cross sections between different isotopes as a function of pion azimuthal angle. The use of a ratio allowed for the study of the changes in the nuclear structures with a reduced bias from experimental systematic errors, which would be similar for the different measurements as they use a common apparatus and analysis method. Clear structures relating to the difference in the nuclear sizes between the isotopes are observed in the ratio. This work presents the first measurement indicating that sensitivity to neutron skin evolution across an isotopic chain can be obtained using an electromagnetic probe.

The theoretical calculations reproduce the general features of the structures visible in the ratio plots, nevertheless, some discrepancies between the experimental data and the model remain. The FSUGold input nuclear structure parameters

in the model, however, have been tuned to the global set of the experimental data and not specifically for the tin isotopes. The functional calculated specifically for the tin isotopes were simply not available at the time of writing the thesis. However, now that the tin data is present, it is anticipated a new set of functionals will be made available and compared to the experimental data. This will not be solely for the FSUGold functional, there are many other functionals also based on relativistic mean field calculations as well as others based on Skyrme Hartree Foch approaches. When this information is available, it will be possible to draw more definite conclusions from the current data. The current results, however, are already very promising in confirming that the experimental method of coherent π^0 photoproduction can indeed provide new constraints on the evolution of the neutron skin along the isotopic chain.

The method described in the thesis can be applied to a future measurement programme. Accesssing the nuclear structure information with a well understood electromagnetic probe offers distinct advantages over other methods, such as the scattering of hadron beams. Coherent pion data of sufficent statistical quality can be obtained in beam times of the order of a few days with modern photon beam and detector facilities. This makes the current method a promising way to constrain nuclear structure over a wide region of the nuclear chart, an important next step to better constrain nuclear structure and the equation of state for nuclear matter.

Bibliography

[1] H. de Vires and et al. *At. Nuc. Dat. Nuc. Dat. Tab. 36*, page 495, 1987.

[2] C. M. Tarbet. *PhD Thesis*. University of Edinburgh, 2007.

[3] C. Tarbert et. al. *Phys. Rev. Lett. 112*, page 242502, 2014.

[4] X. Roca-Maza, M. Centelles, X. Vinas, and M. Warda. *Phys. Rev. Lett. 106*, page 252501, 2011.

[5] P. Haensel. *Space Science Reviews 74*, pages 427–436, 1995.

[6] J. Piekarewicz and S. Pieper. *Nucl. Phys. A 778*, page 10, 2006.

[7] M. B. Tsang et al. *Phys. Rev. C 86*, page 015803, 2012.

[8] W. Heisenberg. *Z. Phys. 77*, pages 1–11, 1932.

[9] J. Dudek. *Meson and baryon spectroscopy from Lattice QCD*. http://irfu.cea.fr/Documentation/Conferences/webCALS12/Talks/March9/dudek.pdf, 2011.

[10] B. Martin and G. Shaw. *Particle Physics*. Wiley and sons, 2008.

[11] C. Amsler and et al. *Phys. Lett. B 667*, page 1, 2008.

[12] D. Dreschel et. al. *Nuc. Phys. A645*, pages 145–174, 1999.

[13] D. Dreschel et. al. *Nuc. Phys. A660*, pages 423–438, 1999.

[14] T. Ericsson and W. Weise. *Pions and Nuclei*. 1988.

[15] F. J. Fattoyev et al. Pure neytron matter constraints on the relativistic mean-field and skyrme-hartree-fock models. *arXiv:1205.0857v1*, 2012.

[16] J. McAndrew. *PhD thesis*. University of Edinburgh, 2011.

[17] R. Walker. *Phys. Rev. 182, 1729*, 1969.

[18] C. Bertulani. *Nuclear Physics in a Nutshell*. Princeton University Press, 2007.

[19] J. Bjorken and S. Drell. *Relativistic Quantum Mechanics*. McGraw Hill, New York, 1964.

[20] F. E. Low G. F. Chew, M. L. Goldberger and Y. Nambu. *Phys. Rev. 106*, pages 1345–1355, 1957.

[21] S. Schamand B. Krusche. *Prog. Part. Nucl. Phys. 51*, page 399, 2003.

[22] V. D. A. Nagl and H. Uberall. *Nuclear Pion Photoproduction*. Springer-Verlag, 1991.

[23] R. Davidson. *Czech J. Phys. 44*, page 365, 1994.

[24] Close, Donnachie, and Shaw. *Electromagnetic Interactions and Hadronic Structure*. Cambridge University Press, Cambridge UK, first edition, 2007.

[25] *The MAID Hompage, http://portal.kph.uni-mainz.de/MAID//maid2007/observ.html*. 2016.

[26] *The MAID Homepage, http://www.kph.uni-mainz.de/MAID*.

[27] *CNS Data Analysis Center, http://gwdac.phys.gwu.edu*.

[28] D. Dreschel. *Eur. Phys. J. A 34*, page 69, 2007.

[29] R. Arndt et al. *Phys. Rev. C 42*, page 1853, 1990.

[30] *The BnGa Homepage, http://pwa.hiskp.uni-bonn.de/*.

[31] B. S. Zou and D. V. Bugg. *Eur. Phys. J. A 16*, page 534, 2003.

[32] A.V. Anisovich et.al. The impact of new polarization data from bonn, mainz and jefferson laboratory on $\gamma p \to \pi n$ multipoles. *https://arxiv.org/abs/1604.05704*, 2016.

[33] J. Beringer et al. *The Review of Particle Physics, Phys. Rev. D86*, 2012.

[34] D. Rönchen at. al. *Eur. Phys. J. A 49*, page 44, 2013.

[35] D. Rönchen at. al. *Eur. Phys. J. A 50*, page 101, 2014.

[36] B. Krusche et. al. *Phys. Lett. B 526*, page 287, 2002.

[37] R. A. Eisenstein and F Tabakin. *Comput. Phys. Commun. 8*, page 130, 1974.

[38] S. Kamalov et. al. M. Gmitro. *Phys. Rev. C 36*, page 3, 1987.

[39] L.C. Liu and C.M. Shakin. *Prog. Part. Nucl. Phys. 5*, page 207, 1981.

[40] M. Warda, X. Vinas, X. Roca-Maza, and M. Centelles. *Phys. Rev. C81*, page 054309, 2010.

[41] J. Piekarewicz. Private communication, 2015.

[42] Zongqiang Sheng and Zhongzhou Ren. *Eur. Phys. J. A46*, pages 241–247, 2010.

[43] J. Piekarewicz. *Phys. Rev. C73*, page 044325, 2006.

[44] J. Piekarewicz. *Phys. Rev. C76*, page 031301, 2007.

[45] J. Piekarewicz. *Phys. Rev. C76*, page 064310, 2007.

[46] R. J. Furnstahl. *Nuc. Phys. A 706*, pages 85–110, 2002.

[47] A. W. Steiner. *Phys. Rept. 411*, pages 325–375, 2005.

[48] C. J. Horovitz et. al. *Phys. Rev. C63*, page 025501, 2001.

[49] P. Ring and P. Schuck. *The Nuclear Many-Body Problem.* Springer Verlag, Heidelberg, 1980.

[50] J. Carlson and R. Schiavilla. Quantum monte carlo calculations of a = 9, 10 nuclei. *Rev. Mod. Phys. 70-3*, page 743, 1998.

[51] S. Pieper et. al. Quantum monte carlo calculations of a = 9, 10 nuclei. *Phys. Rev. C66*, page 044310, 2002.

[52] D. Vautherin et. al. *Phys. Rev. C5*, page 626, 1972.

[53] J. Decharge et. al. *Phys. Rev. C21*, page 1568, 1980.

[54] A. Meucci. *Relativistic Mean Field Theory of Nuclear Structure, Pavia.* 2000.

[55] K. Pomorski et. al. *Nuc. Phys. A624*, pages 349–369, 1997.

[56] B. G. Todd-Rutel and J. Piekarewicz. *Phys. Rev. Lett. 95*, page 122501, 2005.

[57] G. A. Lalazissis, J. Konig, and P. Ring. *Phys. Rev. C55*, page 540, 1997.

[58] J. Piekarewicz. *Phys. Rev. C66*, page 034305, 2002.

[59] J. Piekarewicz. *Phys. Rev. C69*, page 041302, 2004.

[60] J. Zenihiro, H. Sakaguchi, T. Murakami, M. Yosoi, Y. Yasuda, S. Terashima, Y. Iwao, H. Takeda, M. Itoh, H. P. Yoshida, and M. Uchida. *Phys. Rev. C 82*, page 044611, 2010.

[61] A. Trzcinska. *A. Phys. Pol. B. 41*, 2010.

[62] Lie-Wen Chen et al. *Phys. Rev. C72.* 2005.

[63] A. Krasznahorkay et. al. *Phys. Rev. Lett 82*, page 3216, 1999.

[64] A. Krasznahorkay et. al. *Nucl. Phys. A567*, page 521, 1994.

[65] A. Carbone, G. Col, A. Bracco, L. G. Cao, P. Francesco Bortignon, F. Camera, and O. Wieland. *Phys. Rev. C81*, page 041301(r), 2010.

[66] A. Krasznahorkay et. al. *Phys. Rev. Lett 66*, pages 1287–1290, 1991.

[67] A. Tamii et. al. *Phys. Rev. Lett. 107*, page 06502, 2011.

[68] P. G. Reinhard and W. Nazarewicz. *Phys. Rev. C 81*, page 051303 (r), 2010.

[69] S. Abrahamyan and et al. Measurement of the neutron radius of ^{208}pb through parity violation in electron scattering. *Phys. Rev. Lett. 108*, page 112502, 2012.

[70] S. Terashima and et al. *Phys. Rev. C77*, page 024317, 2008.

[71] C. J. Horowitz. *Phys. Rev. C31*, page 1340, 1985.

[72] D. P. Murdock and C. J. Horowitz. *Phys. Rev. C35*, page 1442, 1987.

[73] C. J. Horowitz and B. D. Serot. *Nucl. Phys. A368*, page 503, 1981.

[74] D. A. Hutcheon et. al. *Nucl. Phys. A483*, page 429, 1988.

[75] S. Hama et. al. *Phys. Rev. C41*, page 2737, 1990.

[76] E. D. Cooper et. al. *Phys. Rev. C47*, page 297, 1993.

[77] S. Shlomo et. al. *Phys. Rev. C36*, page 1317, 1987.

[78] K. Nakayama et. al. *Phys. Rev. Lett. 59*, page 1053, 1987.

[79] G. R. Satchler. *Nucl. Phys. A472*, page 215, 1987.

[80] L. Ray et. al. *Phys. Rev. C18*, page 2641, 1978.

[81] A. Trzcinska et. al. *Phys. Rev. Lett 87*, page 82501, 2001.

[82] G. A. Lalazissis et. al. *At. Dat. and Nucl. Dat. Tab. 71*, 1994.

[83] N. Tajima. *Nucl. Phys. A603*, page 23, 1996.

[84] J. Friedrich and P. G. Reinhard. *Phys. Rev. C33*, page 335, 1986.

[85] I. Anthony. Design of a tagged photon spectrometer for use with the mainz 840mev microtron. *Nuc. Inst. Meth A 301*, pages 230–240, 1991.

[86] S. J. Hall, G. J. Miller, R. Beck, and P. Jennewein. *Nucl. Inst. Meth. A 368*, page 698, 1996.

[87] M. Dehn and et al. *Eur. Phys. J. Special Topics 198*, page 1947, 2011.

[88] *A2 MAMI website, http://wwwa2.kph.uni-mainz.de.* 2015.

[89] M. Unverzagt. *Nucl. Phys. Proc. Suppl. 198*, pages 174–181, 2010.

[90] J C. McGeorge and J. D. Kellie et al. *Eur. Phys. J. A, 37*, pages 129–137, 2008.

[91] M. Oreglia et al. *Phys. Rev. D. 25*, page 9, 1982.

[92] A. Starostin et al. *Phys.Rev.C 64*, pages 55–205, 2001.

[93] Audit et al. *Nuc. Inst. Meth. A301*, pages 473–481, 1991.

[94] J. Albert. *PhD thesis.* 2003.

[95] R. Novotny. *IEEE Trans. Nucl. Sci. 38*, page 2, 1991.

[96] *Proceedings of the 13th National Conference on Nuclear Structure in China.* 2011.

[97] P. Martel and R. Miskimen. Analysis of primex targets, 2004.

[98] *A2 MAMI wiki page, https://wwwa2.kph.uni-mainz.de/intern/daqwiki/.* 2015.

[99] D. Krambrich. *University of Mainz, PhD thesis.* 2007.

[100] G. Bruan et al. Tdc chip and readout driver developments for compass and lhc experiments. *arXiv:hep-ex*, 1998.

[101] L. Schmitt. *IEEE Trans.Nucl.Sci.*, pages 51:438–444, 2004.

[102] J. R. M. Annand. *Data Analysis within an AcquRoot Framework. nuclear.gla.ac.uk/ acqusys/doc/AcquRoot.11.08.pd.* 2008.

[103] R. Brun. *Root manual, root.cern.ch.*

[104] D. Middleton. *Mainz a2 tagger calibrations a2 internal report.*, 2011.

[105] M. Unverzagt. *Diploma thesis.* University of Mainz, 2004.

[106] T. Jude. *PhD thesis.* University of Edinburgh, 2010.

[107] G.F. Knoll. *Radiation Detection and Measurement.* John Wiley and Sons, 2011.

[108] M. E. Roebig. *Diploma thesis.* Universitaet Giessen, 1991.

[109] B. Lemmer. *Diploma thesis.* Universitaet, Giessen, 2007.

[110] T. Gesslerr. *Bachelor thesis.* Universitaet, Giessen, 2008.

[111] P. Martel. Private communication, 2015.

[112] G.J. Miller and R. O. Owens. *Nuc. Ins. and Meth.*, pages 390 257–266, 1997.

[113] T. Takaki et. al. *Nucl. Phys. A443*, pages 570–588, 1985.

[114] J. Arends et. al. *Z. Phys. A311*, page 367, 1983.

[115] I. Angeli. *At. Data Nucl. Data Tab. 87*, page 185, 2004.